Exploiting Collective States in Superlattices

Dissertation

zur Erlangung des Grades eines Doktors
der Naturwissenschaften (Dr. rer. nat.)

am Fachbereich Physik der
Freien Universität Berlin

vorgelegt von

Sabrina Jürgensen

Berlin 2024

Erstgutachterin Prof. Dr. Stephanie Reich
Zweitgutachterin: Prof. Dr. Hélène Seiler

Tag der Disputation 30.08.2024

Selbstständigkeitserklärung

Ich erkläre gegenüber der Freien Universität Berlin, dass ich die vorliegende Dissertation selbstständig und ohne Benutzung anderer als der angegebenen Quellen und Hilfsmittel angefertigt habe. Die vorliegende Arbeit ist frei von Plagiaten. Alle Ausführungen, die wörtlich oder inhaltlich aus anderen Schriften entnommen sind, habe ich als solche kenntlich gemacht. Diese Dissertation wurde in gleicher oder ähnlicher Form noch in keinem früheren Promotionsverfahren eingereicht.

Mit einer Prüfung meiner Arbeit durch ein Plagiatsprüfungsprogramm erkläre ich mich einverstanden.

Berlin, 17. Juli 2024, Sabrina Jürgensen

Zusammenfassung

Kollektive Zustände mit ihren faszinierenden optischen Eigenschaften entstehen durch die Kopplung von Dipolmomenten. Die Kopplung der Dipole führt zu einem optischen Verhalten, das stark vom Monomer abweicht. Dipolgekoppelte Systeme besitzen optischen Eigenschaften, die für eine Vielzahl von optoelektronischen Anwendungen, Solarzellen und katalytische Reaktionen benutzt werden. Die entsprechenden Systeme reichen von atomaren und molekularen Gittern bis hin zu plasmonischen Strukturen und können in ihrer Dimensionalität variieren. Für verschiedene Anwendung lassen sich dipolgekoppelte Systeme leicht an die erforderlichen Anforderungen, wie zum Beispiel die Anregungsenergie, anpassen.
Der erste Teil dieser Arbeit untersucht kollektive Zustände in ein- und zweidimensionalen molekularen Gittern. Diese Zustände sind hoch emittierend, haben schmale Linienbreiten, sowie kurze Lebensdauern. Mit einem mikroskopischen Realraum-Dipolmodell zeige ich, dass die Anregung molekularer Einzelschichten robust gegenüber verschiedenen Formen von Unordnung ist. Ich realisiere das Wachstum von Monolagen mit einem Perylenderivat und zeige, dass die kollektiven Zustände auch auf Materialien existieren, die einen großen Zerfallskanal bieten. Anschließend untersuche ich kollektive Zustände in Molekülketten, die in Bornitrid-Nanoröhren eingeschlossen sind. Ich zeige, dass die kollektiven exitonischen Zustände von ein- und mehrgliedrigen Ketten eine enorme Verschiebung zu niedrigen Energien zeigen, die von einer Kette wechselwirkender Dipole nicht hinreichend beschrieben werden kann.
Der letzte Teil meiner Arbeit konzentriert sich auf eine andere Art von dipolgekoppelten Systemen, nämlich bimetallischen Nanopartikel-Superkristallen für photokatalytische Experimente. Kleine Platinpartikel, die in den Hotspots eines Gold-Superkristalls platziert werden, erhöhen nachweislich die H_2-Produktion während der Katalyse. Ich untersuche das schichtabhängige optische Verhalten des Kristalls und berechne die elektrischen Felder in den Hotspots, die ich mit der katalytischen Aktivität des Kristalls vergleiche.

Abstract

Collective states with their fascinating optical properties occur through the coupling of dipole moments. The coupling of the dipoles leads to an overall optical response that varies strongly from the monomer. Dipole coupled systems are manifold systems with optical properties that are interesting for a variety of optoelectronic applications, solar cells, and catalytic reactions. The lattices range from atomic and molecular lattices up to plasmonic structures and can vary in their dimensionality. Depending on the approach, dipole coupled systems can easily be adapted to the relevant requirements, such as excitation energy.

The first part of this work investigates collective states in one- and two-dimensional molecular lattices. These states are highly emissive, have narrow line widths as well as short radiative life times. With a microscopic real space dipole model, I show that excitations of two-dimensional molecular monolayers are robust against various forms of disorder. I realize the growth of two-dimensional monolayers with a perylene derivate and show that the collective states also exist on materials that provide a large radiative decay channel. Then I explore collective states in one-dimensional molecular aggregates, namely in molecule chains encapsulated in boron nitride nanotubes. I verify that the collective exitonic states of single- and multi-file chains show an enormous shift to lower energies that is not captured by the model of a chain of interacting dipoles.

The last part of my work focuses on a different kind of dipole coupled system, namely bimetallic nanoparticle supercrystals for photocatalytic experiments. Small platinum particles that are placed in the hotspots of a gold supercrystal show an increased production of H_2. I investigate the layer dependent optical response of the crystal and calculate the electric fields in the hotspots which I compare with wavelength dependent catalytic experiments. In photocatalytic experiments the binary crystal shows a higher H_2 generation rate than other top performers for formic acid dehydrogenation.

Contents

1 | Introduction

Since hundreds of years dyes and gold particles are used to color objects like textile fabrics or window panes. [1, 2] At first both materials were considered precious and were reserved for the rulers, nobility, and the clerics. Over the centuries dyes and gold particles found their way into everyday life and, subsequently, became a wide research area in the exact sciences. At first glance it appears that dyes and gold nanoparticles have nothing in common except that they can give objects color, but when bringing them into highly ordered systems the physics behind both systems is based on the same mechanism. When illuminated by light, dipole coupling between the single dye molecules or gold nanoparticles leads to a collective state with a unique optical response. This makes the one- and two-dimensional molecular lattices promising candidates for future soft-matter optoelectronic devices and the gold nanoparticle crystals for highly efficient photo-catalysts, solar cells, or sensors. [3–9]

Molecular monolayers exhibit lattice constants ($\sim$1 nm) that are much smaller than the ones of other two-dimensional nanolattices, like plasmonic supercrystal lattices (10-100 nm). [3, 10] This leads to the interesting situation that the translational periodicity of the molecule lattice is two orders of magnitude smaller than the wavelength of light. [11] In plasmonic lattices the effects of disorder are typically neglected, since the fabrication of the structures are either very precisely controlled or the lattices are large enough to be less sensitive to imperfections. [12, 13] In contrast to the fragile two-dimensional molecule layers where the effect of disorder becomes very important for their optical response. [14] Molecular transitions show strong inhomogeneous broadening in ambient environments resulting in lattices that are composed of energetically different transition dipoles. The adsorption and self-assembly of molecules on surfaces is mainly driven by the interaction

with the substrate and by weak intermolecular forces like hydrogen bonding. This makes two-dimensional molecular lattices more vulnerable to the different kinds of disorder than plasmonic structures. [11, 15, 16] Additionally, the dipole coupling of the molecules is screened by the presence of a substrate. Depending on the type of substrate a total quenching of the excited molecular states may appear. [17, 18] Ordered two-dimensional molecular systems are exemplary systems to study the transition from localized single molecules to delocalized Frenkel excitons. Further, the systems provide the opportunity to study how robust collective states are against spatial and energetic disorder, and how quenching affects the formation, energetic position, and line width of the delocalized exciton state.

Plasmonic systems like supercrystals out of noble metal nanoparticles have a large spatial extent and can easily be tailored for different applications by changing the size, shape, or the material of the particles as well as by incorporating molecules into the crystal. [19–22] The choice of the material affects the wavelength range in which the plasmonic structure is optical active. Using gold the plasmonic resonances occur in the visible spectral range making the structures interesting for a variety of applications like surface-enhanced Raman spectroscopy. [23] The mixture of plasmonic gold nanoparticles with smaller catalytic platinum particles creates an interesting platform to study the H_2 generation rate in photo-catalytic experiments. [24]

In Chapter 2 of my thesis, I introduce the optical transitions in single molecules based on fluorescence and Raman scattering. I will explain the different types of line broadening and narrowing that play a role in the context of the emission from molecule aggregates and introduce the oscillator strength that is a measure for the probability of an electron transition. [25] I give an introduction to molecular aggregates, especially to one- and two-dimensional aggregates that form collective states *via* the coupling of their transition dipole moments and discuss the transitions that are dipole allowed or forbidden. In comparison to random agglomerates or three-dimensional crystals, highly ordered low-dimensional molecular crystals show a strong and narrow emission band and due to the delocalization of their exciton state they are often called organic semiconductors. I will discuss the difference between J- and H-aggregates and present a model that explains the optical response of the two molecular aggregates in case of a Coulomb coupled dimer.

In a second microscopic model, I present the extension of the dipole coupling to two-dimensional lattices where the J- and H-type of coupling needs to be taken into account. Further, I explain the strong emission that is based on the creation of a giant dipole moment in J-aggregates that is often named superradiance. I emphasize the importance of the right substrate for the formation of large scale, highly ordered molecule assemblies as well as the different types of lattices that the molecules form on the surface. At the end of the chapter, I introduce the two molecules that I will use for the formation and study of collective states in this thesis.

In the following chapter, I give an introduction to plasmonics with a focus on localized surface plasmons in spherical gold nanoparticles. Plasmons describe the collective oscillation of electrons in metals excited by light. Localized plasmons are non propagating electron oscillations that are confined in a nanoparticle which creates a strong, non-uniform near field around the metal particle. I derive the dielectric function of the metal nanoparticle that determines a majority of the optical properties by a quasi-static approximation as well as the localized plasmon resonance frequency. Size, shape, and material can tune the optical response of the plasmonic particles over the whole visible wavelength range. I further discuss the decay channels of the extremely lossy excitations and the possibility of tailoring them for specific applications. The coupling of plasmonic particles and the generation of strong electric fields, so called hotspots, is discussed, before I focus on supercrystals that are built out of hundreds of coupled gold nanoparticles. I review the synthesis as well as the unique optical properties of the supercrystals resulting out of the excitation of dark modes and deep strong light matter coupling. The last part of the chapter discusses the use of plasmonic systems for photocatalytic experiments. In this thesis, I will use bimetallic supercrystals to study the H_2 production rate during the photocatalytic decomposition of formic acid.

Chapter 4 presents the experimental methods that were used for the sample preparation and investigation. I explain the deposition of the molecules into a two-dimensional lattice, the encapsulation of the molecules into boron-nitride nanotubes, and the synthesis of the gold nanoparticles and their self-assembly into three-dimensional supercrystals. Additionally, I introduce the different fluorescence, absorption, and scattering techniques that were used to investigate and study the optical response of the samples.

In Chapter 5, I present my results on the growth of two-dimensional molecule lattices on different layered materials. Fluorescence microscopy images indicate the growth of molecular monolayers on hexagonal boron nitride. The molecular lattice constants and lattice type could be determined from high-resolution atomic force microscopy measurements. Further, I show by fluorescence spectroscopy the strong and narrow emission of those layers indicating a monolayer and, therefore, a collective state of coupled molecules. The absorption measurements that show a vanishing Stokes shift confirmed the hypothesis of a monolayer. I compare these results with molecular lattices grown on graphene and discuss if the collective state can also exist on metallic materials that quench the fluorescence. At the end of the chapter, I discuss the experimental results in comparison to calculations that were obtained with a real space microscopic dipole model in which different types of disorder were included.

In contrast to the highly emissive two-dimensional molecule layers, discussed in the previous chapter, I study one-dimensional molecular chains that are encapsulated into boron-nitride nanotubes in Chapter 6. Depending on the tube diameter it is possible to incorporate more than one chain into these tubes. Using spatial modulation spectroscopy I measured the absorption of a tube bundle that gives a superposition of single-file and multi-file chains. I compare the optical response of the bundle with the one of the single molecule, which gives information on the aggregate type. With scattering-type scanning near-field optical microscopy I confirm the results of the extinction measurement. At the end of the chapter, I compare and discuss the results with theoretical spectra calculated with the extended microscopic dipole model introduced in the previous chapter.

In the third chapter of my research results, Chapter 7, I take a look at a different type of dipole coupled system. I study plasmonic bimetallic supercrystals and focus on their ability to enhance the H_2 generation during formic acid dehydrogenation. To characterize the crystals I first use a transmission microscope to identify the size of the different layers. With absorption measurements I show that the optical response of the crystals remains almost constant when small platinum particles are inserted into the gaps of the gold supercrystal. Photocatalytic experiments on the bimetallic crystals show an approximately threefold enhanced

H_2 production rate even without illumination (twofold enhancement). At the end of the chapter, I compare the wavelength dependency of the H_2 generation rate with the electric field strength of the gold particles near fields and discuss the results.

In the last chapter of my thesis, I summarize my experimental results and give and outlook on future research ideas.

2 | Organic Systems

In this thesis, I study different molecular systems. The first system consists of organic molecule chains encapsulated in nanotubes and the second system are two-dimensional lattices of organic molecules. Both systems have in common that due to the close packing of the molecules a coupling of the transition dipole moments occurs that leads to a collective state with a strong optical response. In this chapter, I will introduce a selection of topics that are necessary for the understanding of the molecule deposition on solid surfaces and for the experimental results obtained on the two systems that are discussed in Chapter 5 and 6.

2.1 Optical Transitions in Molecules

In molecules electron transitions can occur that are based on different mechanisms. In this section, I introduce two different types of electron transitions that will be used in this thesis for the characterization of Coulomb coupled molecules. Fluorescence which probes the molecular states by the absorption and emission of photons and Raman scattering which probes the vibrations of matter due to a scattering process. Further, I will discuss homogeneous and inhomogeneous broadening as well as motional and exchange narrowing that influence the spectral line width of the fluorescence.

2.1.1 Fluorescence

When illuminated by light a molecule can undergo an optical transition. The molecule absorbs a photon that excites an electron from the electronic ground state (S_0) to an electronically excited state (S_1). Depending on the type of molecule, different excitation energies are needed to excite an electron from the so called highest occupied (HOMO) to the lowest unoccupied molecular orbital (LUMO).

Usually, the excitation energy of molecules ranges from the ultra-violet for small molecules through the whole visible spectral range for dyes. [26]
The absorption process is followed by emission. If the absorption took place into a higher vibronic state ($\nu \neq 0$) non-radiative vibrational relaxation into the vibronic ground state ($\nu = 0$) takes place before the electron relaxes back into its electronic ground state. During the electron transition into the ground state a photon is emitted which is known as fluorescence. [27, 28]
The different transitions in molecules are labeled after the vibronic state out of which the electron is excited and the vibronic level into which the electron is excited. For a transition out of $S_{0,\nu=0}$ into $\nu = 0$ of the higher electronic state S_1 the notation is 0-0 and is called zero-phonon line, Fig. 2.1a. [28]

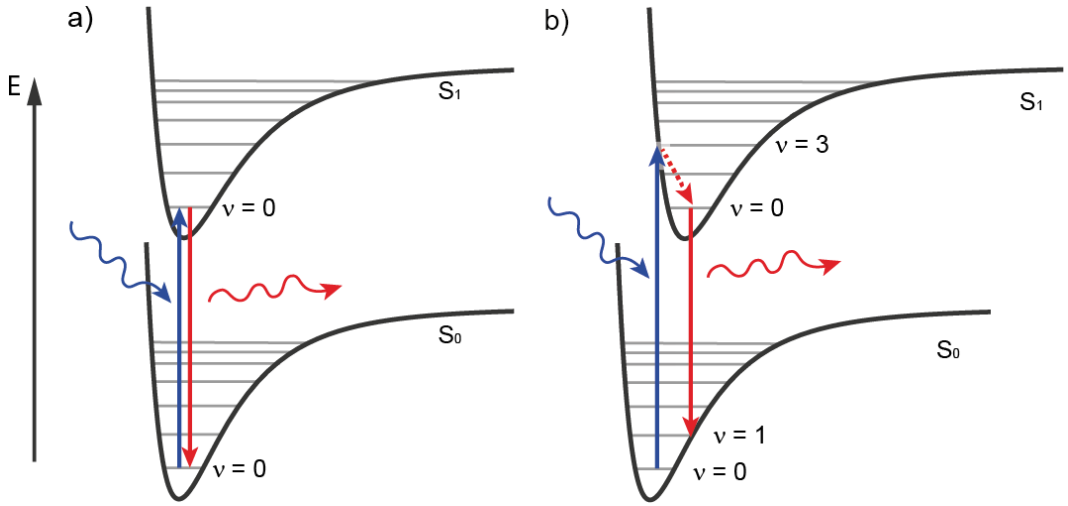

Figure 2.1 **Franck-Condon Principle.** Illustration of the absorption and fluorescence process in a molecule. **a)** Without and **b)** with displacement of the nuclei in the ground and excited state causing a Stokes shift between fluorescence and absorption.

Since the electron movement is much faster than the movement of the heavier nuclei, only vertical transitions are allowed, known as Franck-Condon principle. Usually, a displacement between the nuclei of the ground state S_0 and the excited state S_1 is caused by the bonding properties of the molecular orbitals that represent those two states. [29] Thus, the 0-0 transition becomes unlikely and the absorption into higher vibronic states occurs, Fig. 2.1b, leading to a change in the fluorescence peak ratios. [29, 30] The Franck-Condon principle that is valid for both absorption

and emission in addition to the similar spacing of the vibrational spacing in the ground and excited state entails that the absorbance and emission are normally mirror images of each other. [27, 28] The shift between absorption and emission maximum of the same transition is called Stokes shift and is for single molecules larger if the there is a displacement of the potential curves of the ground and excited state. [29] Thereby, the fluorescence is always red shifted compared to the absorption due to non-radiative relaxation processes.

Homogeneous and Inhomogeneous Spectral Line Broadening

Broadening of emission spectra is a widely observed phenomenon in physics and chemistry. Two main kinds of spectral line broadening are distinguished: homogeneous and inhomogeneous broadening.

In general homogeneous broadening can be seen as a sum of signals with the same frequency (ω) and line width, Fig. 2.2a. [31] It is caused by so called dynamic disorder which involves natural (lifetime) broadening that stems from the finite life time of the excited state and collision (thermal) broadening. [32] For both, the lifetime of the state can directly be determined by the full-width-at-half-maximum (FWHM) of the spectral peak. For low temperatures homogeneous broadening becomes neglectable, since no collisions occur. In collective states thermal line broadening, due to exciton-phonon scattering, influences the spectral line width strongly. [15]

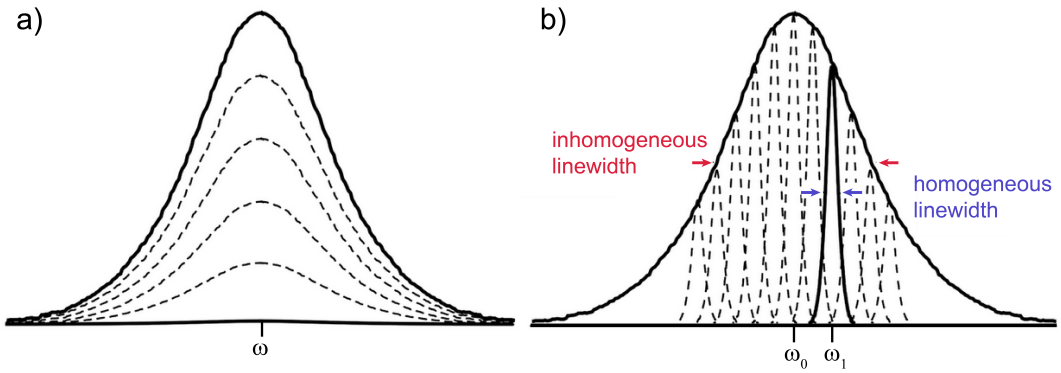

Figure 2.2 **Homogeneous and Inhomogeneous Spectral Line Broadening.** **a)** Homogeneous broadening, all dipoles oscillate with the same frequency ω **b)** Inhomogeneous broadening, slight changes in the frequency ω_0, ω_1, ..., ω_N cause a broadening of the collective signal. Adapted from Ref. [31].

In two-dimensional molecular lattices in addition to homogeneous also inhomogeneous broadening occurs. In contrast to homogeneous broadening the molecules do not emit at the same frequency for inhomogeneous broadening of the line width. Slight changes in the frequency (ω_0, ω_1, ..., ω_N) lead therefore to a broadening of the emission spectrum, Fig. 2.2b. [31] Thus, the lifetime of the excited state can no longer be directly calculated from the FWHM. Inhomogeneous broadening is caused by static disorder which includes disorder in the molecule energies, orientations, and positions which leads to a locally different environment, resulting in different interactions, and thus, to frequency shifts. [32,33] Inhomogeneous broadening affects immensely the spectral line width of two-dimensional molecular systems. [15]

Motional and Exchange Narrowing

Related to one- and two-dimensional coupled molecular aggregates, that will be studied in this thesis (*cf.* Sec. 2.2), two additional mechanisms are frequently mentioned that affect the line shape of the molecular spectral response: motional and exchange narrowing. They are often used as synonyms but describe different processes. [34, 35] While exchange narrowing is related to a process in aggregates, motional narrowing occurs in monomers, as well. [34]

Motional narrowing in aggregates is referred to the reduction of the homogeneous broadened line width due to fast dynamic fluctuations. [34, 36] This implies that the motional narrowing strongly depends on the temperature. [35] While exchange narrowing describes the decrease of the inhomogeneous broaden line shape based on an averaging effect of the delocalized exciton states over a number of statistically independent disorder contributions. [34, 37, 38] The spectral line width of a coupled system can be written as [39]

$$\Gamma = \frac{\gamma}{\sqrt{N_{coh}}}, \tag{2.1}$$

where Γ is the line width of the aggregate, γ the line width of the monomer, and N_{coh} is the number of coherently coupled molecules in the aggregate. Thus, the spectral line width of the aggregate is narrowed by a factor of $1/\sqrt{N_{coh}}$. [39, 40] Since exchange narrowing relies on inhomogeneous broadening it is also limited by static disorder. [40]

Oscillator Strength

During a transition process molecules oscillate for some finite time between the the ground and excited state. Therefore, they can be seen as oscillating dipoles with a transition dipole moment that characterizes the charge displacement by the transition. [25] The probability or strength of an electron transition can thus be described by the oscillator strength f which is proportional to the molar absorption coefficient $\epsilon(\nu)$ [25]

$$f = \frac{4m_{\mathrm{e}}c\epsilon_0}{N_A e^2}\ln(10)\int \epsilon(\nu)d\nu, \tag{2.2}$$

where m_e is the electron mass, c is the speed of light, and ϵ_0 is the electrostatic constant. The Avogadro constant and elementary charge are given by N_A and e, respectively. Thus, the oscillator strength can be direly calculated by the absorption of the molecules in solution using the Lambert-Beer law [28]

$$I = I_0\mathrm{e}^{-\alpha Cl}, \tag{2.3}$$

where I_0 and I give the initial and transmitted light intensity, α a constant of proportionality, C the concentration of the solution, and l the optical path length which corresponds in an absorption experiment to the width of the cuvette. Solving Eq. (2.3) for α gives

$$\alpha = -\frac{1}{Cl}\ln\left(\frac{I}{I_0}\right). \tag{2.4}$$

To find the connection to the measured absorbance A a basis transformation is done and under the assumption that no scattering occurs the relationship $A = -\log(T) = -\log(I/I_0)$ between the absorbance and transmittance T is used [25]

$$\alpha = -\frac{1}{Cl}\ln(10)\log\left(\frac{I}{I_0}\right) \tag{2.5}$$

$$= \frac{1}{Cl}\ln(10)A. \tag{2.6}$$

Using $\epsilon = \alpha / \ln(10)$ results in an expression for the molar absorption coefficient

$$\epsilon(\nu) = \frac{A(\nu)}{Cl}, \tag{2.7}$$

with $[\epsilon] = \text{L mol}^{-1}\ \text{cm}^{-1}$, $[c] = \text{mol L}^{-1}$ and $[l] = \text{cm}$ which is proportional to the area under an absorption band. [28] The oscillator strength is dimensionless and can attain values up to 1 for molecules states with high emission rates. [25]
Using the oscillator strength f the transition dipole moment of a molecule can be calculated by [41]

$$\mu = \sqrt{\frac{3\hbar e^2}{2m_e\omega_0} f}, \tag{2.8}$$

where $\hbar$ is the reduced Planck constant, e the electric charge, m_e the mass of an electron, and ω_0 the transition frequency. The transition dipole moment is a measure for the interaction of light with a molecule. [28]

Fluorescence and absorption spectra can give a variety of information on the aggregate formation of molecules as well as on the dimensionality of the aggregates. In more detail this will be discussed for a molecular dimer in Sec. 2.2.2. The fluorescence of molecules may be quenched by their surrounding medium, for example by the substrate on which the molecules are adsorbed. In such a case the information obtained by the fluorescence are no longer available. Instead the quenching gives access to the much weaker Raman modes of the molecules that are often covered by strong fluorescence. [42]

2.1.2 Raman Scattering in a Molecule

In contrast to fluorescence that is based on the absorption of a photon, Raman spectroscopy studies the inelastic scattering of light by molecules or solids. It measures the vibrational frequency ω_m of the matter as a shift of the incident laser beam frequency ω_0. [42] Two different Raman processes are distinguished: Stokes and anti-Stokes Raman scattering. While in the Stokes process energy is added to the system in terms of vibrations, in the anti-Stokes process energy is removed from the system. Since the population of the molecules at $\nu = 0$ is much lager than $\nu \neq 0$ (Maxwell-Boltzmann distribution) the Stokes process is much stronger. [42]
Raman scattering can be explained by two different approaches. The macroscopic

theory gives an intuitive explanation of the Raman process with classical equations. In case of a molecule it is based on a Taylor expansion of the molecules polarizability with respect to the nuclear displacement. [42–45] The second approach is the microscopic theory which is a quantum mechanic ansatz based on time-depend perturbation theory. It has the advantage to give an insight into the intermediate steps of a Raman scattering process and therefore enables to obtain an expression for the polarizability. [43, 44]

In the microscopic picture the Stokes process is based on the annihilation of an incident photon with frequency ω_0 and an optical transition of the molecule from its electronic and vibronic ground state (g) to a virtual intermediate state (i), that is far below the molecules first electronic state (S_1). [43] A new photon with frequency ω_{if}, that is smaller than the incident photon energy ω_0, is created and the molecule is transferred into a finale state (f). The electronic state of the final state is thereby identical with the initial state (S_0) but the vibronic state changes, Fig. 2.3a. [30] In the special case that the excitation corresponds to the energy of an electronic transition the intermediate state is no longer a virtual state and the process is called resonant Raman scattering, Fig. 2.3b. [42, 43]

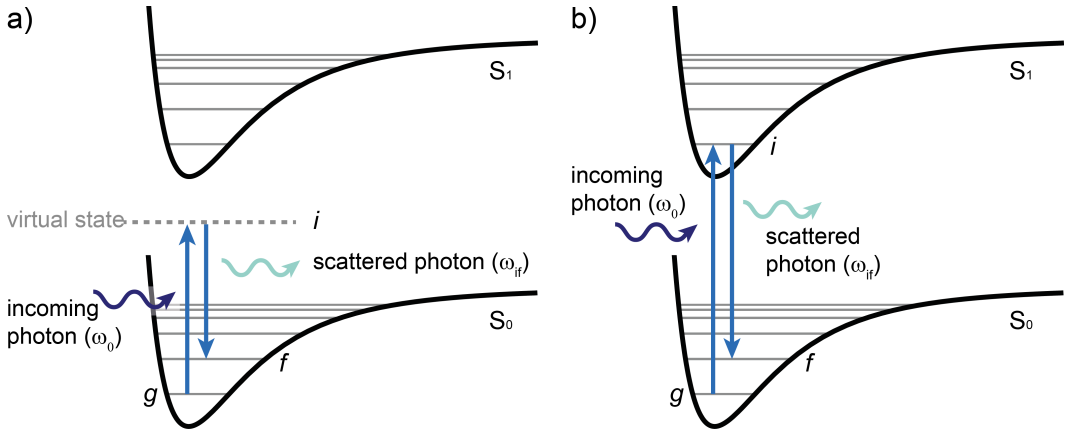

Figure 2.3 **Raman Scattering in a Molecule - Stokes Process.** The incoming laser light excites the molecule into an energetically higher intermediate state (i). From this excited state the molecule is transferred into a final state (f) which has the same electronic state (S_0) as the initial state but a different vibronic state (ν). Is the intermediate state **a)** a virtual state it is the standard Raman scattering process or **b)** resonant Raman when it is a real molecular state. Adapted from Ref. [43].

In the classical macroscopic picture the Raman process in an infinite, isotropic medium can be described by a dipole moment μ_{ind} that is induced in the molecule when placed in an external electric field E [45]

$$\mu_{ind}(t) = \alpha E = \alpha E_0 \cos(2\pi\omega_0 t) \tag{2.9}$$

where α is the polarizability that describes the distortion of the electron cloud by an external electric field and E_0 the amplitude of the electric field. [45] In the case of the isotropic medium the polarizability is a scalar otherwise it is a second rank tensor. Since at room temperature the molecule vibrates at a frequency ω_m the variation of the nuclear position q is given by [45]

$$q(t) = q_0 \cos(2\pi\omega_m t) \tag{2.10}$$

with q_0 being the amplitude of the distortion. The polarizability of the molecule varies with respect to the displacement of the nuclei due to a change of the molecule's conformation. Thus, the polarizability can be written as [45]

$$\alpha(t) = \alpha_0 + \left(\frac{\partial\alpha}{\partial q}\right)_0 q + ..., \tag{2.11}$$

where the first term is the polarizability of the molecule at fixed nuclei and the second term the variation of the polarizability due to the molecule oscillation at equilibrium position. Raman scattering can be observed, if $(\partial\alpha/\partial q)_0$ is different from zero. [45] In this case the mode is called "Raman active". Substituting the term of the polarizability and the distortion into the equation of the induced dipole moment, Eq. (2.9), gives [45]

$$\begin{aligned}\mu_{ind}(t) &= \alpha_0 E_0 \cos(2\pi\omega_0 t) + \left(\frac{\partial\alpha}{\partial q}\right)_0 q_0 \cos(2\pi\omega_m t) E_0 \cos(2\pi\omega_0 t) \\ &= \alpha_0 E_0 \cos(2\pi\omega_0 t) + \left(\frac{\partial\alpha}{\partial q}\right)_0 \frac{E_0 q_0}{2}[\cos(2\pi(\omega_0 - \omega_m)t) + \cos(2\pi(\omega_0 + \omega_m)t)].\end{aligned} \tag{2.12}$$

Here, the first term represents the Rayleigh scattered light that is elastically scattered by the molecule (no change in the frequency). The other two terms describe the Raman scattered light where the term with $\omega_0 - \omega_m$ is the Stokes and

$\omega_0 + \omega_m$ the anti-Stokes term.

The intensity of the scattered radiation is proportional to the squared second derivative of the dipole moment [45]

$$I \propto \left(\frac{d^2 \mu_{ind}}{dt^2} \right)^2 , \tag{2.13}$$

thus, the intensity of a Stokes Raman mode at $\omega_0 - \omega_{gf}$ is theoretically given by [42, 46]

$$I_{gf} \propto I_0 \cdot (\omega_0 - \omega_{gf})^4 \left| \left(\frac{\partial \alpha_{gf}}{\partial q} \right)_0 \right|^2 , \tag{2.14}$$

where g and f denote the initial and final vibronic states of the electronic ground (S_0) state, and I_0 the intensity of the laser beam with frequency ω_0.

An expression for the polarizability in Eq. (2.14) can be found in the microscopic picture using second-order quantum mechanic perturbation theory [42, 43]

$$\alpha_{gf} = \frac{1}{h} \sum_i \left(\frac{M_{gi} M_{if}}{\omega_{gi} - \omega_0 + \mathrm{i}\Gamma_i} + \frac{M_{gi} M_{if}}{\omega_{if} + \omega_0 + \mathrm{i}\Gamma_i} \right) , \tag{2.15}$$

with the sum running over the intermediate states i. ω_{gi} and ω_{if} denote the frequencies which correspond to the excitation and relaxation process, respectively. h is the Planck constant, M the electronic transition moment of the respective transition, and $\mathrm{i}\Gamma_i$ is the damping constant which is related to the life time of the scattering state. In case of resonant Raman scattering, the frequency of the incoming light ω_0 corresponds to the electron-transition (resonance) frequency ω_{gi} of the molecule, thus the denominator of the first term in Eq. (2.15), which describes the Stokes process, becomes nearly zero and as a consequence α becomes large. Hence, the intensity I_{gf} in Eq. (2.14) of the Raman mode $\omega_0 - \omega_{gf}$ increases enormously. [42] The second (anti-Stokes) term can be neglected since it does not become dominant. [43]

By changing the excitation energy (ω_0) a resonance profile can be recorded. Therefor, the integrated Raman intensity (area below the peak) of one Raman mode is plotted over the respective excitation energy. [14, 47, 48] The resulting resonance profile can be seen as pseudo absorption spectrum of the molecule, Fig. 2.4. Thereby, the Raman resonance frequency (ω_{gi}) corresponds to the absorption maximum.

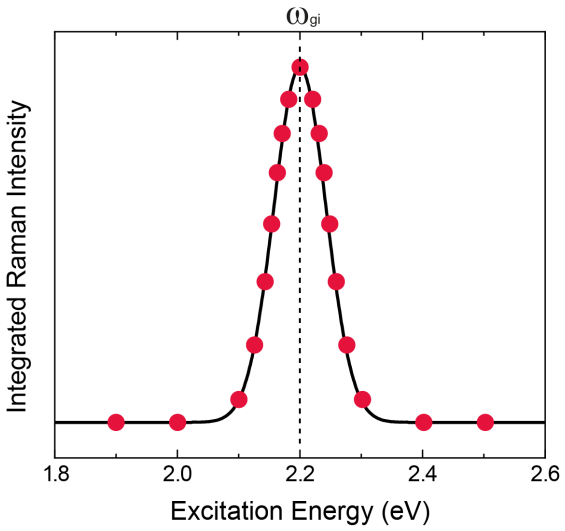

Figure 2.4 **Scheme of a Resonant Raman Profile.** The red circles represent the integrated Raman intensities of a Raman mode at different excitation energies. The black line is a fit. When the illuminating light corresponds to a transition in the molecule the integrated Raman intensity is maximum.

2.2 Collective States

There are several possibilities for two or more molecules to interact in clusters, *e.g.*, *via* $\pi - \pi$ stacking, charge transfer, van der Waals interaction, or dipole coupling. [49] The optical response of the molecule system changes dramatically through their interaction, especially, when going from single molecules *via* two-dimensional systems to bulk materials. [3]

In this thesis I will focus on one-dimensional chains and two-dimensional lattices of molecules coupling through transition moments (Coulomb coupling) in aggregates. Considering two molecules, two main types of aggregates are distinguished, so called J- and H-aggregates. In J-aggregates the transition dipole moments of the molecules are aligned in a "head-to-tail" configuration, while in H-aggregates the dipole moments are aligned parallel in a "side-by-side" manner. [49] When extended to a two-dimensional lattice J-aggregates form a giant dipole due to attractive coupling of the transition dipole moments of each molecule leading to a delocalization of the excitons over the molecule lattice, Sec. 2.2.1, resulting in a narrow and strong emission combined with a short life time. [3, 50, 51]

In this section, the characteristic features and optical properties of highly ordered

molecular aggregates in comparison to single molecules and bulk material will be discussed. First, excitons and the concept of the delocalization of an excited state will be introduced. The coupling of molecules and the resulting optical response of molecular aggregates will first be explained on the basis of a dimer model. Afterwards an extended model for two-dimensional molecular aggregates in real-space will be introduced followed by the the superradiance phenomenon. At the end of the section, the substrate and molecule choice as well as the favored lattice structures of two-dimensional molecule layers will be discussed.

2.2.1 Excitons

Excitons describe bound electron-hole pairs that can be excited by light and appear in different types depending on the system. In a two-dimensional lattice molecular excitations can couple *via* their transition dipole moments. In this case the collective excitations are no longer localized, they become spatially delocalized over the molecule lattice. [52] In a two-dimensional molecular system they are called Frenkel excitons. Frenkel excitons are excitons where the electron-hole pair is located at one molecule, Fig. 2.5a, strongly bound by Coulomb interactions. [51] The strong coupling of the Frenkel excitons leads to a small spatial extent, resulting in outstanding properties like high radiative rates, and high charge carrier mobility. For Frenkel excitons the temperature as well as spatial disorder have effects on

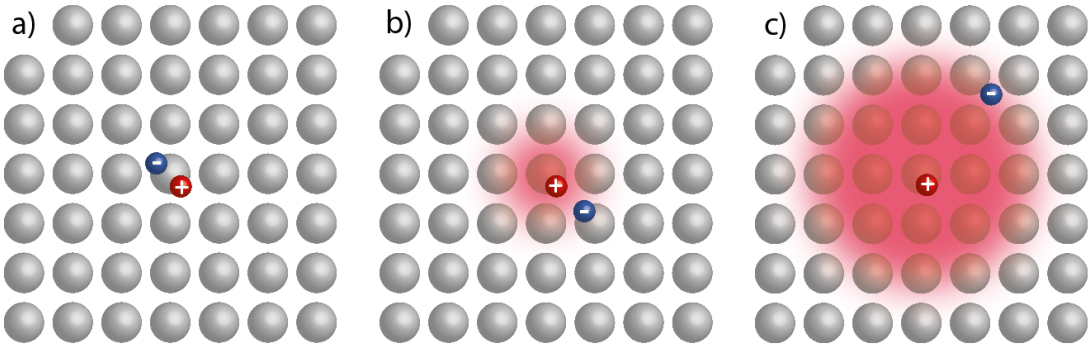

Figure 2.5 **Different Types of Excitons and their Spatial Size. a)** Frenkel exciton, **b)** charge-transfer exciton, and **c)** Wannier Mott exciton. While Frenkel excitons are located at a single molecule (atom), the exciton radius (indicated by the red circle) of the Wannier Mott and charge-transfer exciton are larger. The electron (blue) and hole (red) are located at different molecules (atoms). The gray spheres symbolize the molecules (atoms).

the delocalization which directly affects the line shape of the optical response of the collective state, as previously discussed in Sec. 2.1.1 (in-/homogeneous broadening). [53]
In bulk crystals of organic molecules additionally to Frenkel excitons, charge-transfer excitons exist, Fig. 2.5c. [53] Charge transfer excitons host electron-hole pairs that are not located at only one single molecule leading to small recombination rates and a damping of the delocalization.
In contrast to organic semiconductors, inorganic two-dimensional semiconductors host a third type of excitons called Wannier Mott excitons. Like in charge-transfer excitons the electron and hole is located on different atoms, Fig. 2.5c, giving rise to only weak but long range Coulomb interactions. [54] In comparison to charge-transfer excitons, electron and hole in Wannier Mott excitons are even further separated.

2.2.2 Dipole Coupling of Two Molecules

The coupling of two molecules can be described by a hybridization model. The creation of a molecular dimer leads to a splitting of the excited states. The two molecular configurations of J- and H-aggregates lead to completely different optical properties. In J-aggregates the Coulomb force that acts between the molecules is attractive (binding) while in the case of an H-aggregate the Coulomb force is repulsive (antibinding). To describe the Coulomb coupling J_C between molecules usually the point-dipole approximation is used that neglects vibronic coupling and other interactions and only considers the Coulomb force between the molecules [49, 55, 56]

$$J_C = \frac{1}{4\pi\epsilon}\left(\frac{\boldsymbol{\mu_1}\cdot\boldsymbol{\mu_2}}{r^3} - \frac{3(\boldsymbol{\mu_1}\cdot\boldsymbol{r})(\boldsymbol{\mu_2}\cdot\boldsymbol{r})}{r^5}\right) \tag{2.16}$$

$$= \frac{\mu^2(cos(\alpha) - 3cos^2(\theta))}{4\pi\epsilon r^3}. \tag{2.17}$$

Here, $\boldsymbol{\mu_1}$ and $\boldsymbol{\mu_2}$ are the transition dipole moments of the two molecules, $\boldsymbol{r}$ the displacement vector between the two dipoles, and ϵ the dielectric constant of the surrounding medium. Further, α is the angle between the dipole orientation and θ the slip angle between the transition dipoles. Illustrations of the two angles and

the resulting aggregates are shown in Fig. 2.6a,b.
Assuming that the dipoles are of equal strength ($\mu_1 = \mu_2 = \mu$) and point in the same direction ($\alpha = 0°$ or $180°$) the equation reduces to

$$J_C = \frac{\mu^2(1 - 3cos^2(\theta))}{4\pi\epsilon r^3}. \tag{2.18}$$

If the angle θ becomes lager than 54.7° (magic angle) the Coulomb coupling becomes positive and the transition from J- to H-aggregates occurs, Fig. 2.6c. The coupling of the two transition dipole moments leads to two delocalized exited states (S'$_1$ and S"$_1$) that are split by twice the Coulomb coupling ($2|J_C|$). The states form by a linear combination out of the localized excited states of the single molecules. The symmetric in-phase combination is an optically allowed bright state and shifted by J_C while due to the summation of the single transition dipole moments the antisymmetric out-of-phase state is a dark state and shifted by -J_C. [49]

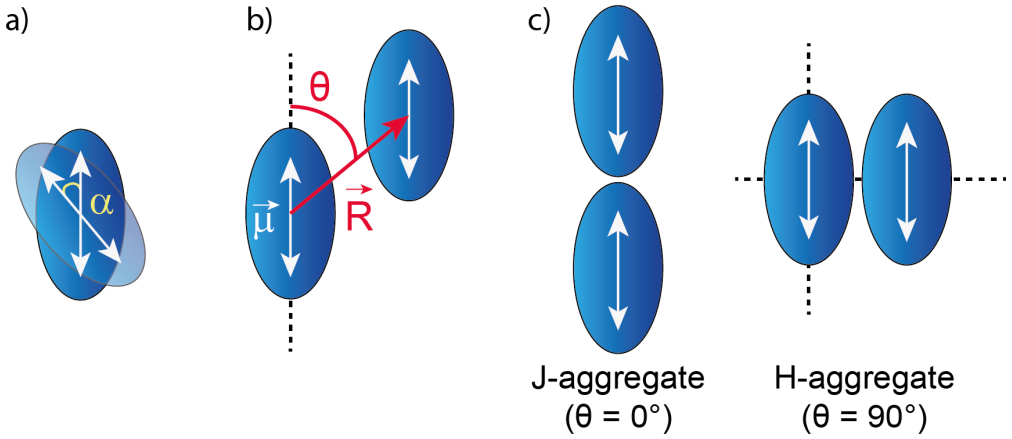

Figure 2.6 **Angle Dependent Dipole Coupling of Two Molecules.** Illustration of **a)** the dipole orientation angle α and **b)** the slip angle θ. **c)** Sketch of two molecules that point into the same direction ($\alpha = 0°$) and couple *via* their transition dipole moment. A slip angle of $\theta = 0°$ leads to the formation in a head-to-tail fashion (J-aggregate) while $\theta = 90°$ results in a side-by-side packing (H-aggregate).

This results for the J-aggregates ($J_C < 0$) in an optical active lower excited state (S'$_1$) while for the H-aggregates ($J_C > 0$) this state is dipole-forbidden and the energetically higher state (S"$_1$) is allowed, Fig. 2.7. As can be seen in the energy diagram the coupling of the transition dipole moments has a huge influence on the optical response of the different aggregate types. Since for H-aggregates the higher excited state is optically active the absorption is blue shifted compared to

the monomer, while for J-aggregates typically a red shift is observed. [49, 55] The splitting of the side-by-side configuration is usually larger than for the head-to-tail configuration since the dipoles are closer packed leading to stronger shifts. Thus, conclusions about the coupling strength can directly be drawn on the basis of the shift in the absorption spectrum. [57]

The absorption process is followed by emission. Rapid internal conversion from the higher to the lower and dipole forbidden exciton state results in a vanishing probability for the fluorescence of H-aggregates leading to a weak 0-0 emission, Fig. 2.7. [49, 55, 58]

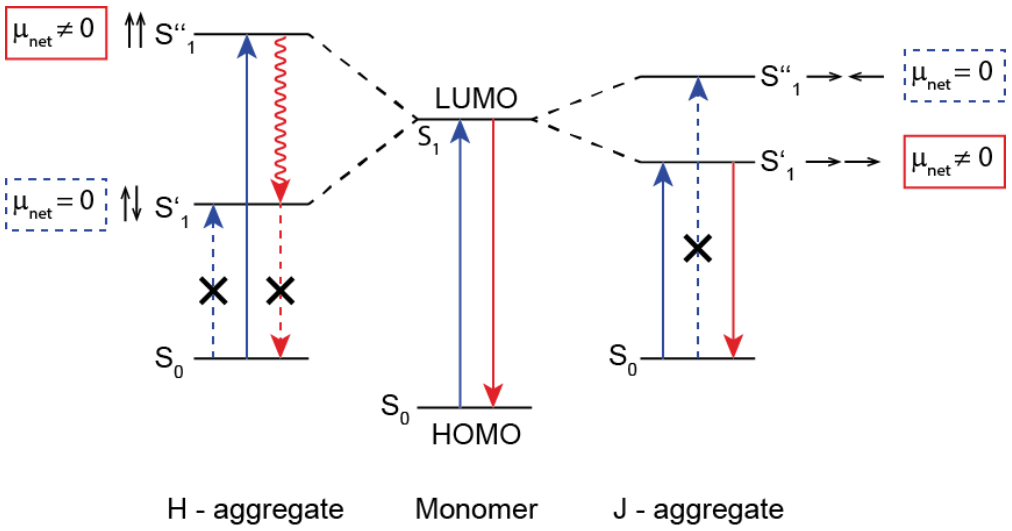

Figure 2.7 **Energy Diagram of the Optical Transitions in J- and H-Aggregates in Comparison to a Monomer.** The blue and red arrows depict the absorption and emission, respectively. For J-aggregates only the transition into the lower level of the excited state is allowed, while H-aggregates absorb into the higher level due to selection rules. In H-aggregates non-radiative intraband transitions (wavy red arrow) cause an electron population of the lower excited state which is not followed by fluorescence due to the selection rules that do not allow that transition. Adapted from Ref. [50].

The Stokes shift between the absorption and emission is a measure for the different types of aggregates. For molecules aligned in the head-to-tail configuration the Stokes shift is expected to tend towards zero, since the fluorescence and the absorption are red shifted. For H-aggregates on the other hand a strong Stokes shift occurs due to the opposite shift of the emission and absorption, Fig. 2.8.

The characteristic narrowing of the spectral line width of the J-aggregate emission is due to exchange narrowing, as previously discussed in the context of the fluorescence process, *cf.* Sec. 2.1.1. H-aggregates typically show a less intense emission, due to vanishing small transition dipole moments (low quantum yield). [28] The line width of H-aggregates is usually much broader due to various band energy levels formed by the vibronic coupling between Frenkel and charge-transfer excitons. [4, 59] In literature π-stacks of molecules are often referred as H-aggregates these show a broad line width, as well. [60]

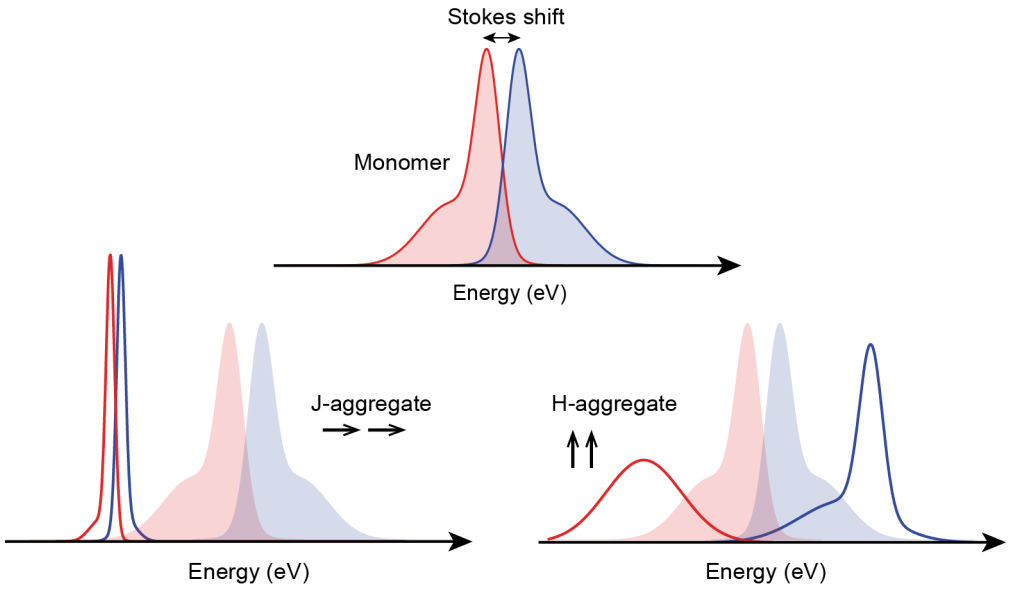

Figure 2.8 **Stokes Shift of Molecular Aggregates and a Monomer.** Illustration of the Stokes shift of a J- and H-aggregate in comparison to a monomer. J-aggregates show a small Stokes Shift and red shifted emission (red) and absorption (blue). Whereas H-aggregates exhibit a large Stokes shift with red shifted emission and blue shifted absorption. Adapted from Ref. [50].

The model described above works well for the dipole-dipole coupling of a dimer. For (multi-)chains and two-dimensional molecular lattices the model needs to be extended to take several molecules as well as the J- and H-type of inter-molecular interactions into account. In the literature, the two-dimensional configuration is often referred to as HJ-aggregate or is extend by an I-aggregate that usually includes additional types of interactions. [11] In this thesis, I will only consider dipole-dipole coupling when talking about two-dimensional molecule systems. [49, 61–64]

2.2.3 Microscopic Model of Collective Dipoles[1]

To model (multi-)chains and two-dimensional lattices of molecules that contain contributions of J- and H-aggregates, Fig. 2.9, a real space approach based on Greens functions can be used. [11, 65] The advantage in comparison to reciprocal space approaches is that spatial as well as frequency disorder and lattice defects can easily be incorporated in a real-space model. [11] In the microscopic model the transitions of each molecule are described as point dipoles $d = \alpha E_0$ that are excited by an external electric field E_0. Here, α is the polarizability of each individual molecular dipole and is given by

$$\alpha = \frac{d_{ge}^2}{\hbar(\omega_0 - \omega - \mathrm{i}\gamma_0)}, \tag{2.19}$$

where d_{ge} is the transition dipole moment, ω_0 the exciton frequency, ω the driving frequency, and $2\gamma_0$ the spectral broadening. Considering a monolayer of molecules, the dipole moments of each molecule are modified by the coupling to the electric fields of other transition dipoles, Fig. 2.9. This leads to changes of the dipole moment at lattice site i which can be written as

$$d_i = \alpha E_0(\mathbf{r}_i) + \alpha \sum_{i \neq j} \mathrm{G}_{ij} d_j, \tag{2.20}$$

where $\mathrm{G}_{ij} \equiv \mathrm{G}(\mathbf{r}_{ij})$ is a Green function that accounts for near-field and far-field coupling, with

$$\begin{aligned} \mathrm{G}(\mathbf{r}_{ij})\mathbf{d}_j = & \frac{k^3}{4\pi\epsilon_0\epsilon_m} \mathrm{e}^{\mathrm{i}kr_{ij}} \left[\left(\frac{1}{kr_{ij}} + \frac{\mathrm{i}}{(kr_{ij})^2} - \frac{1}{(kr_{ij})^3} \right) \mathbf{d}_j \right. \\ & \left. - \left(\frac{1}{kr_{ij}} + \frac{3\mathrm{i}}{(kr_{ij})^2} - \frac{3}{(kr_{ij})^3} \right) (\hat{\mathbf{r}}_{ij} \cdot \mathbf{d}_j)\hat{\mathbf{r}}_{ij} \right]. \end{aligned} \tag{2.21}$$

Here $\mathbf{r}_{ij} = \mathbf{r}_i - \mathbf{r}_j$, $r_{ij} = |\mathbf{r}_{ij}|$ represents the distance between the interacting molecules, ϵ_m is the dielectric screening by the surroundings, and k is the wavenumber.

[1] Parts of this section were published as *Collective States in Molecular Monolayers* in Juergensen et al. ACS Nano **17**, 17350–17358, DOI: 10.1103/PhysRevB.107.235122 (2023). The microscopic model was developed within this work by N.S. Mueller.

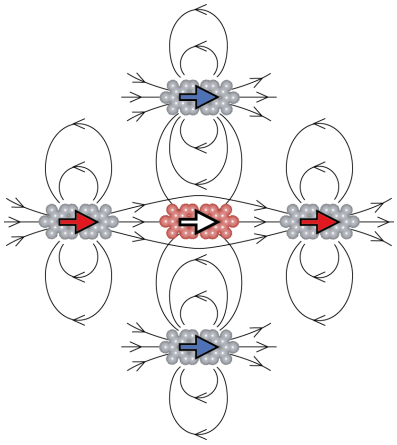

Figure 2.9 **Dipole Coupling of a Two-Dimensional Molecular Lattice.** The scheme illustrates the nearest neighbor interactions of molecules in a two-dimensional layer. The red arrows depict a J-aggregate (attractive forces) with respect to the molecule (white arrow) in the center and the blue arrows represent a H-aggregate with repulsive character. [11]

When all dipoles oscillate along the same spatial direction the vector notation can be omitted. Following Ref. [65], Eq. (2.20) can be written in terms of a coupling matrix M as $\mathbf{E}_0 = \mathrm{M}\mathbf{d}$. The coupling matrix has the general form $\mathrm{M}_{ij} = \delta_{ij}\alpha^{-1} - (1-\delta_{ij})\mathrm{G}_{ij}$, where δ_{ij} is the Kronecker delta function, and the entries of the vectors $\mathbf{E}_0$ and $\mathbf{d}$ stand for each lattice site. To understand the collective behavior, an eigenmode expansion

$$\mathrm{M}\mathbf{m}_p = \mu_p \mathbf{m}_p, \tag{2.22}$$

is used with the complex eigenvectors $\mathbf{m}_p$ and eigenvalues μ_p of M. The polarizability α_{coll} of the collective mode is given by the sum of the polarizability α_p of each mode

$$\alpha_{\mathrm{coll}} = \sum_p \alpha_p = \sum_p \frac{1}{\mu_p} = \sum_p \frac{d_{ge}^2}{\hbar(\omega_0 - \omega + \Delta_p) - \mathrm{i}\hbar(\gamma_0 + \gamma_p)}. \tag{2.23}$$

The interaction of the transition dipoles leads to a shift in the frequency $\Delta_p = d_{ge}^2\,\mathrm{Re}(g_p)$ and a broadening $\gamma_p = d_{ge}^2\mathrm{Im}(g_p)$ of each mode, where g_p are the complex eigenvalues of the Green function G. The response of the dipole lattice to an external electric field is described by the collective dipole moment

$$\mathbf{d} = \alpha_{\mathrm{coll}}\mathbf{E}_0 = \sum_p b_p \alpha_p \mathbf{m}_p, \tag{2.24}$$

with the expansion coefficients b_p defined by a vector decomposition of the electric field $\mathbf{E}_0 = \sum_p b_p \mathbf{m}_p$. The collective optical response can be measured experimentally by the extinction of the molecule layer

$$\sigma_{\text{ext}} = \frac{k}{\epsilon_0 E_0^2} \text{Im}(\mathbf{E}_0^\dagger \cdot \mathbf{d}) \approx \frac{k}{\epsilon_0 E_0^2} \sum_p |b_p|^2 \text{Im}(\alpha_p). \tag{2.25}$$

This model allows to calculate and compare the different eigenmodes and transition dipole moments of a dipole lattice as well as the energetic shift in the extinction.

Besides the arrangement in a plane, molecules can also stack together building multi-layer systems. Particularly organic molecules with their large conjugated π-electron system tend to build π-π stacks. In molecular multi-layer films the coexistence of Frenkel charge transfer electrons, that occur from the π-stacking, result in a broad and red shifted emission compared to the monomer. [3, 51, 66]

2.2.4 Superradiance

Superradiance describes a phenomenon of strong and narrow emission. It is often referred as Dicke superradiance named after its explorer. [67] It occurs when molecules couple coherently, creating a giant dipole. When spontaneously emitting photons, the intensity (I) of the emission scales no longer with the number (N) of molecules, like for an ensemble of incoherent emitters, but with the square of the amount of molecules [68, 74]

$$I_{SR} \propto N^2. \tag{2.26}$$

This results further in an N times increased and therefore much faster decay rate τ_{SR} [68, 74]

$$\tau_{SR} = \frac{\tau}{N}, \tag{2.27}$$

where τ is the spontaneously radiative decay time of the uncoupled emitters, Fig. 2.10. [69] For a single layer of highly ordered organic molecules on hexagonal boron nitride short radiative lifetimes of 27 ps for the superradiance were reported compared to 556 ps for a monomer or even 1.73 ns for multi-layers of the same molecules. [3]

Superradiance is observed from 0 - 0 transitions and goes along with a suppression of transitions to higher vibronic states, *cf.* Sec. 2.2.2. As a consequence the

intensity ratio of the 0 - 0 and 0 - 1 transition is an indication for the presence of superradiance. [33]
The coherence length which is the number of coupled molecules is an essential measure for the strength of superradiance and can be calculated by the intensity ratio of the 0 - 0 and 0 - 1 transition [70, 71]

$$N = \frac{I_{0-0}}{I_{0-1}}\lambda^2, \tag{2.28}$$

where λ^2 is the dimensionless Huang-Rhys factor that describes the strength of vibrational coupling. Since dynamic disorder controls the coherence length especially for a highly ordered collective system, superradiance strongly depends on the temperature. [15, 32] The coherence length shows usually a $N \propto 1/T$ behavior where T is the temperature. [15, 72, 73] Due to negligible exciton-phonon scattering at low temperatures the emission of collective states strongly increases at those temperatures. Additionally, the FWHM of the zero-phonon line decreases by $1/\sqrt{N}$ due to reduced homogeneous broadening, see Sec. 2.1.1. [15, 32, 53, 72]

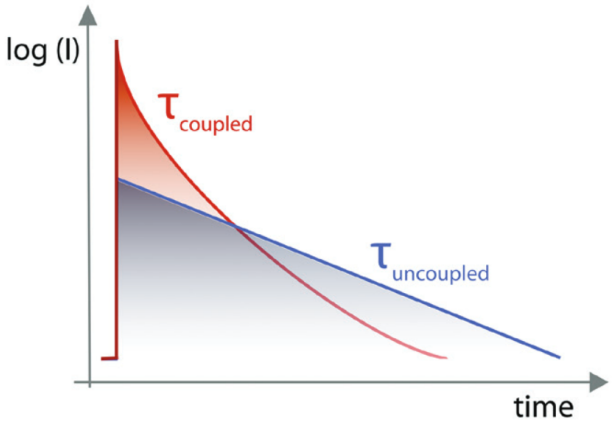

Figure 2.10 **Radiative Decay Rates.** Characteristic radiative decay rates of coupled (red) and uncoupled (blue) emitters, showing the much faster decay of the coupled system. Adapted from Ref. [74].

There are ongoing discussions if a cross over temperature ($\sim 40\,\mathrm{K}$) exists below which static disorder controls the decrease of the coherence length [75] or if dynamic disorder dominates the coherence length at all temperatures and static disorder controls the coherence time. [32] Eisfeld *et. al* reported further that the temperature dependency of superradiance in brick-wall aggregates (see Sec. 2.2.6) depends on

the size and shape of the aggregate domain. [73] They did not assume the normal exciton-localization ansatz by increasing temperature but explained the temperature dependence by thermal population with different transition strength. Depending on the size and shape of the ordered molecule domain the attractive forces are reduced or completely canceled by the repulsive forces between the molecules which results in lower transition strength or even in dark states. [76] For rectangular domains it was shown that the resulting wave function is asymmetric leading to an intensity of the superradiant state that first increases with temperature up to $\sim$16 K before it starts to decrease again. [73]

2.2.5 Substrate Choice and Possible Substrate Influences

The choice of the substrate plays an important role for the alignment of molecules on its surface as well as for the optical response of the molecular structure. Factors that must be considered when choosing a substrate are the energy transfer between substrate and molecule, the affinity of the molecule to the substrate and the surface topography. Particularly for monolayers of molecules the substrate strongly affects the optical response of the molecule system and therefore becomes crucial. [33]

Materials, like hexagonal boron nitride (hBN) and chlorine alkali halides, *e.g.*, sodium (NaCl) or potassium chloride (KCl) that provide a large optical band gap are perfect substrates to observe the fluorescence of a collective state. This makes it possible to distinguish easily between the different types of molecular aggregates (c.f. Sec. 2.2.2). Whereas, zero-band gap materials like graphene or other (semi-)metals (Au, Ag, Cu) quench the emission of the molecules totally due to charge and energy transfer from the molecule to the underlying conductive material. [33, 77, 78] One example for quenching is the non-radiant Förster resonant energy transfer (FRET). The mechanism relies on dipole-dipole interaction between a donor and acceptor. When an organic molecule is adsorbed, *e.g.*, on graphene, the fluorescence of the molecules is quenched due to energy transfer between both $\pi-$systems. [79] Thereby, the excited molecules go back into their ground state while creating an exciton in the graphene. [77, 78, 80] Important to note is that there is no intermediate photon created. [27] Since graphene has a broad absorption over the visible spectral range, it overlaps with the emission of nearly every dye molecule. Therefore, FRET occurs for the majority of dyes that are placed close

to graphene. [77] As mentioned at the end of Sec. 2.1.1 in case of fluorescence quenching, the Raman signal of the molecules becomes measurable since the Raman modes are no longer covered by the much stronger fluorescence. In contrast to fluorescence the Raman signal does not give a direct conclusion on the present type of aggregate. To prevent the loss of information a single layer of hBN can decouple the molecules from the substrate and stop the full quenching of the fluorescence by the substrate. [81] Alternatively, functional groups can serve as spacers to prevent quenching of the fluorescence by the support. [33]

Different kinds of materials have different affinities to molecules. Usually, the bonding of organic molecules to metals is stronger than for the less reactive dielectric surfaces. This typically leads to less ordered systems on dielectric surfaces or to layers in which the molecules are aligned perpendicular to the substrate surface, due to stronger inter molecular interactions. This causes the formation of collective states with strong H-aggregate character. [33] Thus, a certain surface to molecule interaction is needed to obtain highly ordered monolayers.

Another important factor for the choice of a growth substrate is the surface topography or roughness. The surface of a substrate affects the alignment of the molecules. Materials like graphene, hBN, and chlorine alkali halides have ultraflat surfaces. Here, the orientation of the molecules is not influenced by the surface topography of the underlying growth material. If the material is thick enough it also protects against the roughness of the bottom substrate. [82] Instead of aligning with the topography, for ultraflat chlorine alkali halides, it was shown that molecules align with respect to the underlying cations and chlorine atoms and therefore may start to bend. [83] Depending on the type of molecules epitaxial growth of molecule lattices either along the zig-zag or parallel to the armchair direction of the underlying hBN was reported. [53, 82]

In this thesis, I will use hBN and (multi-layer) graphene to study collective state of organic molecules. Both materials have ultra-flat surfaces and are easy to exfoliate to obtain flakes for the molecular lattice growth. The difference in their band gap gives the opportunity to study if a collective state also exist on zero-band gap materials or if in that case the substrate quenching prevents the creation of the collective state.

2.2.6 Two-Dimensional Molecular Lattice Structures

The origin of molecular layer growth occurs at surface steps, grain boundaries, or defects. [84] Single molecules are rarely found on solid substrates at room temperature. [84] Molecules form typical lattice structures during the self-alignment process. Often observed are herring bone, brick wall, and Q-phase structures, Fig. 2.11a-c. [3, 15, 16, 72, 84, 85] Other structures that are found are often unstable at room temperature. [33] Crucial is the alignment of the molecules with respect to each other. Depending on the slip angle and the orientation of the molecules the attractive or repulsive forces between the transition dipole moments prevail leading to a more J- or H-like response of the collective state. [63] The lattice constants of the lattices differ depending on the packing density, the deposition temperature, and the molecule size. [86–88] This affects the coupling strength and the optical response of the collective state. [33] The number of molecules per unit cell differs for the different types of lattices as well. While the herring bone and Q-phase structure contain two molecules, the brick wall has only one molecule per unit cell, black squares in Fig. 2.11. [15] If the unit cell contains two or more molecules a splitting of the molecule's electronic state occurs due to interactions in the unit cell which is called Davydov splitting. [89]

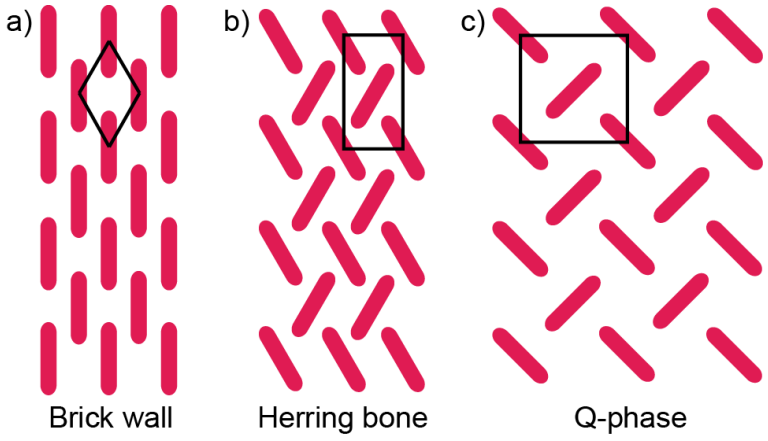

Figure 2.11 **Self-Assembly Lattice Structures of Molecules.** The three most common molecular lattices that show J-aggregate response: **a)** Brick wall, **b)** herring bone, and **c)** Q-phase lattice. The black rectangle depicts the unit cell of the respective lattice.

The size of the molecular layer is limited by the flake size of the underlying material. [72] A monolayer normally consists out of many differently orientated

domains due to surface defects and steps. [15] For the organic dye molecule PTCDA[2] on KCl(100) domain sizes of roughly 12×12 molecules were observed. [73] In case of hBN, it was shown that the thickness of the hBN does not influence the deposition of the molecules. Nearly on every hBN flake monolayers were found. [72]

2.2.7 Organic Molecules for Collective States

The two molecules that form J-aggregates and will be investigated in the experimental part of this thesis are introduced in this section. As discussed theoretically in Sec. 2.2.2 and 2.2.3, collective states of molecular aggregates can be achieved in one-dimensional as well as in two-dimensional systems. Templates, containers, or structured surfaces are often used to create coupled one-dimensional systems. One possibility is the encapsulation of molecules in nanotubes. [47, 90, 91] Since nanotubes are restricted by their inner diameter not every molecule is suitable for the encapsulation process. Oligothiophenes are commonly used molecules to study molecular aggregates of different dimensionality. Due to their rod-like shape they fit perfectly into nanotubes. One example is α-sexithiophene (6T), Fig. 2.12a. [47, 90, 91] It consists of six thiophene units that are connected at their α carbon atoms. The transition dipole moment of the 6T is parallel to the long axis of the molecule. This results in J-aggregates if the molecules are aligned in a head-to-tail fashion inside the nanotube.

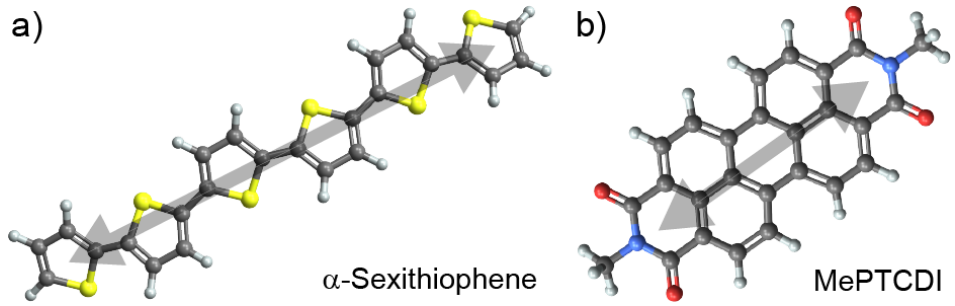

Figure 2.12 **Organic Molecules Organizing in J-Aggregates.** Two example molecules that self-assembly in J-aggregates: **a)** α-sexithiophene (6T) and **b)** MePTCDI. The transition dipole moment is indicated by the gray arrow.

An organic molecule group that forms two-dimensional crystals are perylene-based molecules. Perylene derivatives are planar molecules that are based on a

[2] perylenetetracarboxylic dianhydriden

perylene core. Different functional groups can be substituted to the perylene to vary the optical properties of the molecule or to be used as spacer to change the interaction of the molecules with the substrate underneath. [92] N,N'-dimethyl-3,4,9,10-perylentetracarboxylic diimide (MePTCDI), Fig. 2.12b, is one example. MePTCDI has an imide group added to both sides of the perylene core. To both imide groups a methyl group is attached *via* the nitrogen atom. The transition dipole moment of MePTCDI is oriented along the long molecular axis equal to 6T. When adsorbed onto a surface the molecules stabilize *via* inter molecular hydrogen-oxygen interactions. [53, 88, 93]

The two molecules described above are two examples out of a pool of organic molecules that are used to study collective states. Both belong to the family of dye molecules and are optically active in the visible spectral range. As part of this thesis I will probe the optical response of aggregates built by these two molecules.

3 | Plasmonics

Plasmonics is a research area in optics and solid state physics. It studies the interaction of light and free electrons, mostly light and electrons in small particles out of noble metals or highly doped semiconductors. By irradiating metallic nanoparticles the free electrons interact with the light and start to oscillate, creating plasmons. Plasmons focus light in small volumes below the diffraction limit and generate strong near fields at the particle surface. [94] The optical properties of plasmonic nanoparticles differ strongly from the bulk material and depend essential on the dielectric function of the material as well as the size and the shape of the nanoparticle.

The unique optical properties of small metal particles have been known for hundreds of years. The Romans used them to color, *e.g.*, drinking vessels, and in medieval times it was common to mix metal particles into glass to color church and cathedral windows. [1, 2] Nowadays, plasmons are not only used because of their color. Plasmonics is currently a wide research area in physics, biology, and chemistry since the possibility of light-harvesting and enhancing processes is a key to boost development and technologies. [95] Electronic devices are supposed to become smaller and faster, and biological and chemical reactions to get more efficient. [94] In addition, the production methods for plasmonic structures like electron beam lithography made progress, making it possible to produce precise nanostructures for different applications giving an additional research boost.

This chapter introduces in Sec. 3.1 the fundamentals of plasmonics using the example of a gold nanoparticle. The influence of the dielectric function on the optical properties of plasmons as well as the derivation of the localized surface plasmon resonance *via* an quasi static approximation, and the coupling and decay of plasmons will be discussed. The synthesis of nanoparticles and the formation of plasmonic supercrystals and their optical properties are explained in Sec. 3.2. In

the last section of this chapter, Sec. 3.3, the application of plasmonic structures in catalytic experiments is discussed.

3.1 Localized Surface Plasmons

Surface plasmon-polaritons (short plasmons), which are mixed plasmon-photon modes that occur at the interface between two materials with different dielectric functions are divided into two main groups depending on their propagation behavior. [26] Propagating plasmon-polaritons propagate along the materials interface whereas localized surface plasmons are electron oscillations that are localized by the size of a nanostructure. [96] The name plasmon-polariton comes from the generation of plasmons by the interaction of light with metal surfaces, Fig. 3.1. Their optical properties can be calculated by the laws of classical electrodynamics and depend strongly on the dielectric function of the materials. [96] In the following, I will focus on localized surface plasmons in metallic nanoparticles. The dielectric constant of the plasmonic particle will be established by the Drude model and the resulting optical properties of the plasmon will be discussed afterwards.

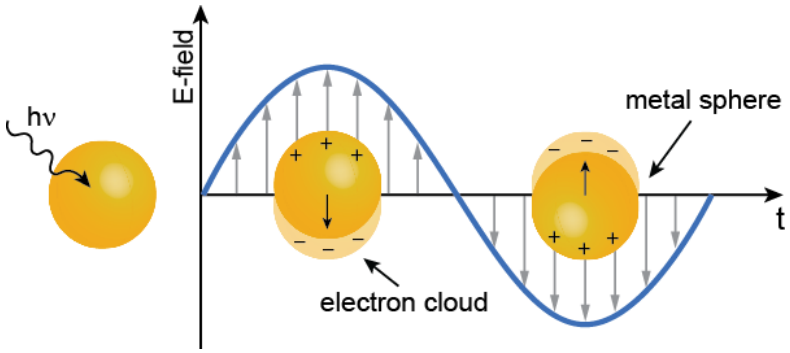

Figure 3.1 **Sketch of the Excitation of a Plasmon by an External Light Field.** An external electric field (blue wave) drives the free electrons inside a gold nanoparticle into a collective oscillation, generating a plasmon. Adapted from Ref. [44].

3.1.1 Dielectric Function of a Plasmonic Particle

Considering a metal nanoparticle in an external electromagnetic field the equation of motion of the free electrons in the conduction band of the metal can be written

as [96]

$$m\ddot{\boldsymbol{x}} + m\gamma\dot{\boldsymbol{x}} = -e\boldsymbol{E}, \tag{3.1}$$

where m is the mass of an electron, γ the damping (losses), and e the charge of the electron. Compared to the Lorentz model, Drude used the approximation that the electrons are not "bound" to the ion core and therefore have no restoring force (ω_0=0). With $\boldsymbol{E}(t) = \boldsymbol{E_0}e^{i\omega t}$ being the external electric field, the solution of the equation is $\boldsymbol{x}(t) = \boldsymbol{x_0}e^{i\omega t}$ describing the oscillation of the electrons in the metal. Inserting this expression into Eq. (3.1) yields [96]

$$\boldsymbol{x}(t) = -\frac{e}{m(\omega^2 + i\gamma\omega)}\boldsymbol{E}(t). \tag{3.2}$$

With this formula the induced dipole $\boldsymbol{P}$ per unit volume can be calculated [97]

$$\boldsymbol{P} = -\mathcal{N}e\boldsymbol{x} = -\frac{\mathcal{N}e^2}{m(\omega^2 + i\gamma\omega)}\boldsymbol{E}(t), \tag{3.3}$$

where $\mathcal{N}$ is the number of oscillators per unit volume. This equation shows that a polarization is generated due to the displacement of the free electrons by the external electric field.

Maxwell's equation in matter (macroscopic Maxwell equation) for the induced displacement field $\boldsymbol{D} = \epsilon_0\boldsymbol{E} + \boldsymbol{P} = \epsilon_0\epsilon\boldsymbol{E}$ gives [96]

$$\begin{aligned}
\boldsymbol{D} &= \epsilon_0\boldsymbol{E} + \boldsymbol{P} \\
&= \epsilon_0\boldsymbol{E} + \frac{\mathcal{N}e^2}{m(\omega^2 + i\gamma\omega)}\boldsymbol{E} \\
&= \epsilon_0\left(1 - \frac{\omega_p^2}{\omega^2 + i\gamma\omega}\right)\boldsymbol{E} = \epsilon_0\epsilon\boldsymbol{E},
\end{aligned} \tag{3.4}$$

with ϵ_0 being the electric permittivity and $\omega_p = \sqrt{\frac{\mathcal{N}e^2}{\epsilon_0 m}}$ the plasma frequency which depends on the electron density $\mathcal{N}$ of the material. The plasma frequency describes the natural oscillation frequency of the free-electron-plasma charge density. [26] Therefore, the dielectric function of a metal nanoparticle in an external electric filed is given by [96]

$$\epsilon(\omega) = 1 - \frac{\omega_p^2}{\omega^2 + i\gamma\omega} \tag{3.5}$$

which is related to the refractive index $n(\omega) = \sqrt{\epsilon(\omega)}$ of the particle's material.

Thus, the plasma frequency of the material determines the optical properties of the plasmonic material.

The dielectric function in Eq. (3.5) can be separated in a real and imaginary part

$$\epsilon(\omega) = \epsilon_1(\omega) + i\epsilon_2(\omega) \tag{3.6}$$

where the expressions for the real and imaginary part are [96]

$$\mathrm{Re}[\epsilon(\omega)] = \epsilon_1(\omega) = 1 - \frac{\omega_p^2}{\omega^2 + \gamma} \approx 1 - \frac{\omega_p^2}{\omega^2}, \tag{3.7}$$

$$\mathrm{Im}[\epsilon(\omega)] = \epsilon_2(\omega) = \frac{\omega_p^2 \gamma}{\omega(\omega^2 + \gamma^2)} \approx \quad \frac{\omega_p^2 \gamma}{\omega^3}, \tag{3.8}$$

by using the approximation that the damping γ in this systems is usually much smaller than the frequency ω of the illuminating light. [98] For frequencies smaller than the plasma frequency the real part of the dielectric function becomes negative. The imaginary part on the other hand is small if ω is not far below ω_p. The combination of negative $\mathrm{Re}[\epsilon(\omega)]$ and small $\mathrm{Im}[\epsilon(\omega)]$ implicates a variety of interesting optical properties such as plasmon resonances, that occur if $\mathrm{Re}[\epsilon(\omega)]$ becomes zero which is the case when the incident light corresponds to the plasma frequency. [26] The plasma frequency of the metal divides the optical properties of the material into two regimes. The negativity of the real part for frequencies smaller than the plasma frequency gives metals their property of reflecting light and thus the shiny appearance. On the other hand for frequencies larger than the plasma frequency light can penetrate through the metal that acts more like a dielectric at these energies as far as the optical properties are concerned. [52]

So far the optical response of the positive charged metal ions have been ignored completely and only the intraband transitions in the conduction band of the metal have been considered. To take also the bound (inner) electrons into account a further term $\epsilon_b(\omega)$ needs to be implemented. Therefore, the dielectric function, Eq. (3.5), is extended to [26, 96]

$$\epsilon(\omega) = \epsilon_b(\omega) - \frac{\omega_p^2}{\omega^2 + i\gamma\omega}. \tag{3.9}$$

In the Drude model $\epsilon_b(\omega) = \epsilon_\infty$ is a constant that describes the screening from the inner electrons. The real part becomes therefore $\mathrm{Re}[\epsilon(\omega)] \approx \epsilon_b(\omega) - (\omega_p^2/\omega^2)$ and

the imaginary part $\mathrm{Im}[\epsilon(\omega)] \approx \omega_p^2\gamma/\omega^3$.
The dielectric function from gold can be fitted well with these equations, Fig. 3.2, but for energies above 2 eV the model fails. [96] This is where the gold interband transitions from the *d*- to the *s*-band start to appear. Thus, for higher energies a more complex expression for $\epsilon_b(\omega)$ is needed that takes the interband transitions of the bound electrons into account. [26] Further, the plasma (resonance) frequency is shifted by the interband transitions. The resonance occurs now at $\omega = \omega_p/\epsilon_b(\omega)$.
This section introduced the dielectric function of a metal nanoparticle. In the following section the optical response of metallic nanoparticles and their dependency on the dielectric function as well as the resonance frequency will be discussed in more detail.

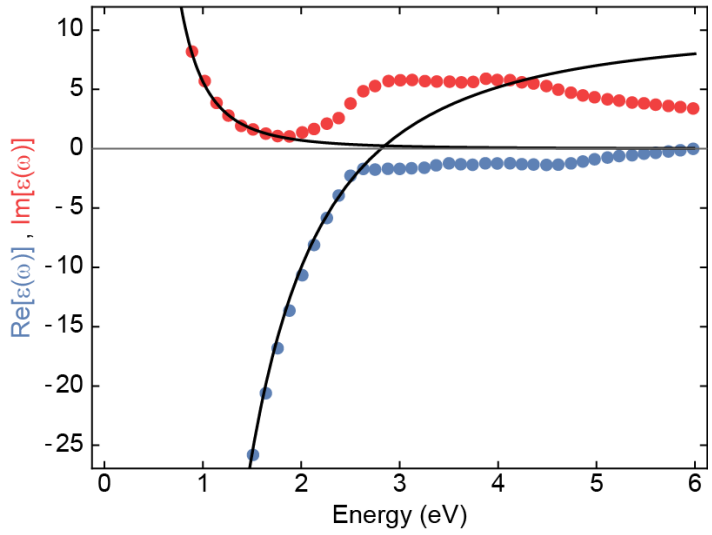

Figure 3.2 **Real and Imaginary Part of the Dielectric Function of Gold.** The data points are experimental data from Johnson and Christy [99] fitted with the Drude model, Eq. (3.7) and (3.8). As fitting parameters $\epsilon_b(\omega) = \epsilon_\infty = 9.75$, $\omega_p = 8.85\,\mathrm{eV}$, and $\gamma = 70\,\mathrm{meV}$ were used.

3.1.2 Localized Surface Plasmon Resonance

Describing the localized surface plasmons by the quasi-static approximation assumes that the particle size is much smaller than the wavelength of the incident light. [96] In this case the particle is located in an electrostatic field $\boldsymbol{E} = E_0\hat{\boldsymbol{z}}$. Further approximations are: the particle is a homogeneous, isotropic sphere of radius a placed at $\boldsymbol{r} = 0$ and has a material specific complex dielectric function $\epsilon(\omega)$. The

surrounding medium of the particle is set to be isotropic and non-absorbing with dielectric constant ϵ_m. A sketch of this configuration is shown in Fig. 3.3.

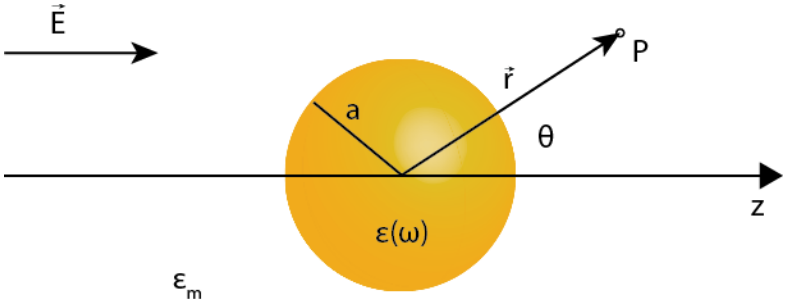

Figure 3.3 **Sketch of a Spherical Metal Nanoparticle in an External Electric Field.** Sketch of a homogeneous, isotropic sphere with sub-wavelength radius a and dielectric function $\epsilon(\omega)$ placed in a medium with dielectric function ϵ_m. The applied electrostatic field $\boldsymbol{E}$ is parallel to the z-axis. Adapted from Ref. [96].

To calculate the electric field $\boldsymbol{E} = -\nabla\Phi$ outside the particle it is necessary to solve the Laplace equation $\nabla^2\phi = 0$. Because the problem has azimuthal symmetry, the general solution is of the form [96]

$$\Phi(r,\Theta) = \sum_{l=0}^{\infty} \left[A_l r^l + B_l r^{-(l+1)}\right] P_l \cos(\Theta), \tag{3.10}$$

where $P_l\cos(\Theta)$ are the Legendre Polynomials of order l, and Θ is the angle between the z-axis and the position vector $\boldsymbol{r}$ at point P. From the boundary conditions $r \to \infty$ and $r = a$ the coefficients A_l and B_l are determined. With the requirement that the potential at the origin remains finite, the potential outside the sphere is given by [96]

$$\Phi_{out} = -E_0 r\cos(\Theta) + \frac{\epsilon(\omega)-\epsilon_m}{\epsilon(\omega)+2\epsilon_m} E_0 a^3 \frac{\cos(\Theta)}{r^2}. \tag{3.11}$$

Physically Eq. (3.11) describes the superposition of the applied field and that of a dipole located at the particle center. Using the definition of the dipole moment [96]

$$\boldsymbol{p} = 4\pi\epsilon_0\epsilon_m a^3 \frac{\epsilon(\omega)-\epsilon_m}{\epsilon(\omega)+2\epsilon_m}\boldsymbol{E} \tag{3.12}$$

the potential outside the sphere can be written as [96]

$$\Phi_{out} = -E_0 r\cos(\Theta) + \frac{\boldsymbol{p}\cdot\boldsymbol{r}}{4\pi\epsilon_0\epsilon_m r^3}. \tag{3.13}$$

Equation (3.13) shows that a dipole moment is induced inside the particle by the applied field with a magnitude that is proportional to $|\boldsymbol{E}|$. *Via* $\boldsymbol{p} = \epsilon_0 \epsilon_m \alpha \boldsymbol{E}$ the dipole moment can be set in relation to the polarizability α of a small sphere with sub-wavelength diameter [96]

$$\alpha = 4\pi a^3 \frac{\epsilon(\omega) - \epsilon_m}{\epsilon(\omega) + 2\epsilon_m}, \tag{3.14}$$

$$= 3V_{NP} \frac{\epsilon(\omega) - \epsilon_m}{\epsilon(\omega) + 2\epsilon_m} \tag{3.15}$$

which depends on the volume V_{NP} of the spherical nanoparticle. A strong resonance between the free electrons and the electric field appears under the condition that the denominator of Eq. (3.14) becomes minimal. This is the case at the frequency for which the *Fröhlich Condition* [96]

$$\mathrm{Re}\left[\epsilon(\omega)\right] = -2\epsilon_m \tag{3.16}$$

is satisfied. Here, $\epsilon(\omega)$ is the dielectric function, Eq. (3.5), of free electrons. The frequency ω, which fulfills the resonance condition, corresponds to the localized surface plasmon resonance frequency of the nanoparticle. Within the Drude model the Fröhlich condition for a spherical metal particle is fulfilled at [96]

$$\omega_{pl} = \frac{\omega_p}{\sqrt{1 + 2\epsilon_m}} \tag{3.17}$$

which is called the localized surface plasmon resonance bulk frequency. It depends on both the type of metal (ω_p) and the surrounding environment (ϵ_m) of the sphere. With increasing dielectric constant of the surrounding medium the localized surface plasmon resonance will blue shift.

3.1.3 Near- and Far-Field Response

Using $\boldsymbol{E} = -\nabla\Phi$ and Eq. (3.13) the electric field of a localized surface plasmon outside the sphere can be evaluated as [96]

$$\boldsymbol{E_{out}} = \boldsymbol{E} + \frac{3\boldsymbol{n}(\boldsymbol{n} \cdot \boldsymbol{p}) - \boldsymbol{p}}{4\pi\epsilon_0\epsilon_m r^3}, \tag{3.18}$$

where $\boldsymbol{n}$ is the unit vector in direction of the point of interest P. Equation (3.18)

shows that the resonance in the polarizability leads to a resonant enhancement of the field outside the particle. The field that surrounds the plasmonic nanoparticle is called near field. It is not uniformly distributed and decays rapidly with $1/r^3$. [100] Figure 3.4a shows a simulation of a single gold nanosphere with its locally strong electric near field that is generated in the direction of the polarization of the external electric field.

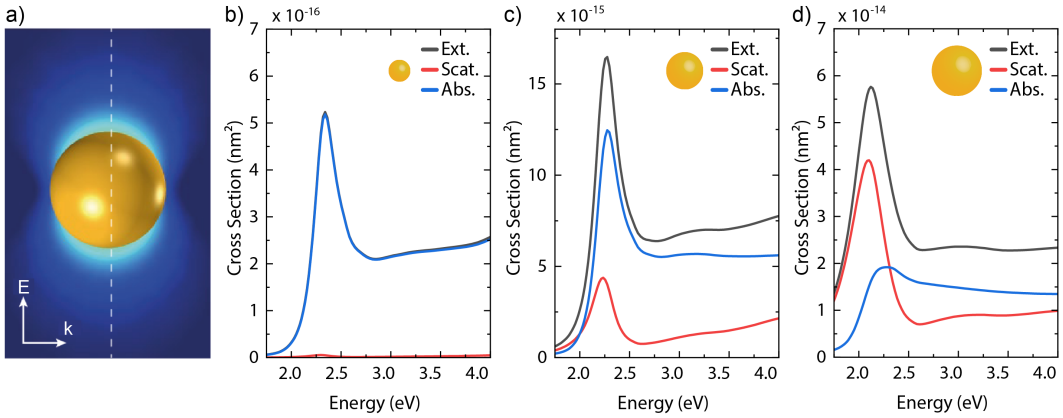

Figure 3.4 **Near-Field Distribution and Optical Cross Sections of a Single Gold Nanoparticle. a)** Near-field distribution around a single gold particle. [101] Extinction (black), scattering (red), and absorption (blue) cross section of a single spherical gold nanoparticle with **b)** 20 nm, **c)** 60 nm, and **d)** 100 nm diameter in a surrounding medium with refractive index 1.4, *e.g.*, polystyrene. For the cross section calculations the "Mie Theory Calculator" was used. [102, 103]

The polarizability influences not only the near-field response of plasmonic particles but also the cross sections of the far-field response. The scattering (C_{sca}) and absorption (C_{abs}) cross section of the metallic nanoparticle in the external electric field can be calculated by the quotient of the power that is scattered (P_{sca}) or absorbed (P_{abs}) by the particle and the power density of the incident light (S_{inc}) using the polarizability [26, 96, 97]

$$C_{sca} = \frac{P_{sca}}{S_{inc}} = \frac{k^4}{6\pi}|\alpha|^2 = \frac{3k^4 V_{NP}^2}{2\pi}\left|\frac{\epsilon(\omega)-\epsilon_m}{\epsilon(\omega)+2\epsilon_m}\right|^2, \tag{3.19}$$

$$C_{abs} = \frac{P_{abs}}{S_{inc}} = k\,\mathrm{Im}[\alpha] = 3kV_{NP}\,\mathrm{Im}\left[\frac{\epsilon(\omega)-\epsilon_m}{\epsilon(\omega)+2\epsilon_m}\right]. \tag{3.20}$$

Here, $k = 2\pi/\lambda_m = \sqrt{\epsilon_m}\omega/c$ is the wavenumber of the incident light. The resulting two expressions are proportional to the volume of the nanoparticle in the case

of C_{abs} and the volume squared for C_{sca}. This shows that for small particles the absorption is dominant while for particles with larger diameter the scattering increases until it dominates. [96] Figure 3.4b-d depict this relation based on three different gold particles sizes. The sum of C_{sca} and C_{abs} gives the extinction cross section.

Further, the dependency of the cross sections on the polarizability leads to shifts of the optical far-field response that are induced by the size, shape, and the kind of material (dielectric function) of the nanoparticles. [19–22] The effect can directly be seen when comparing gold spheres in solution, Fig. 3.5a. Depending on the size of the particles the color of the solution changes from red to purple for large spheres, indicating a shift in the resonance frequency. For colloidal gold particles with diameters up to 100 nm, the extinction (resonance) lies in the range between 500 nm and 650 nm (1.9 - 2.5 eV), Fig. 3.5b, shifting to larger wavelengths (smaller energies) by increasing the particle diameter. [104, 105] The effect of the particle shape on the optical response is shown in Fig. 3.5c based on silver particles for spheres, pentagons, and triangles.

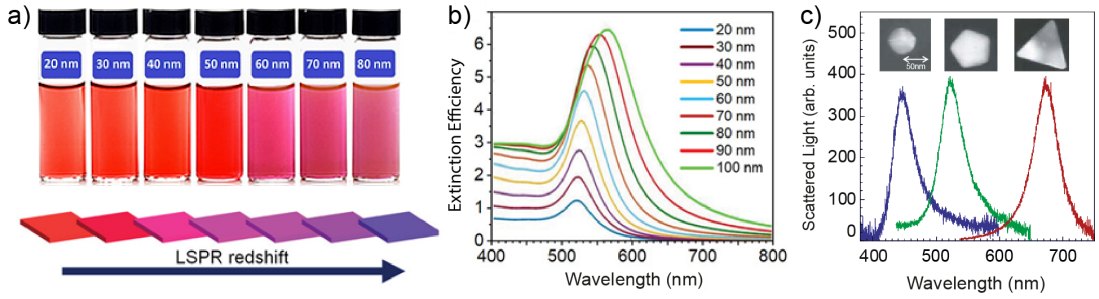

Figure 3.5 **Size and Shape Dependence of the Plasmon Resonance. a)** Spherical gold nanoparticle of different size in solution. The shift of the plasmon resonance is indicated by the different color of the solutions. **b)** Extinction spectra of gold particles between 20 and 100 nm showing a red shift in their optical response. **c)** Scattering spectra of differently shaped silver nanoparticles. Showing a resonance shift depending on the shape. Adapted from Refs. [96, 106, 107]

In the next subsection the different pathways of plasmon decay and their dependency on the particles size will be discussed. I will show that the possibility to tune the decay processes is useful for a number of applications.

3.1.4 Plasmon Dynamics and Decay (Losses)

Plasmons have a short life time τ_{pl}. Already after a few femtoseconds (∼10 fs) the collective oscillation of the free metal electrons decays. [108] The short life time of the plasmon is directly connected to the spectral line width $\Gamma_{pl} = 2\hbar/\tau_{pl}$ of the plasmon resonance, resulting in a broad resonance. [44, 109] The total line width depends on different radiative (Γ_{rad}) and non-radiative (Γ_{nr}) loss channels that are sketched in Fig. 3.6. The resulting total spectral line width can be written as [44, 110, 111]

$$\Gamma_{pl} = \Gamma_{rad} + \Gamma_{nr} = \Gamma_{rad} + \Gamma_b + \Gamma_{surf}, \tag{3.21}$$

where Γ_b are bulk and Γ_{surf} surface losses. A measure for the damping of a system and the sharpness of the optical response is the quality factor $Q = \omega_{pl}/\Gamma_{pl}$ that depends on the total line width and the plasmon resonance frequency ω_{pl}. [112, 113] Besides gold, silver is a commonly used material for plasmonic systems. Even though the quality factor of small silver nanoparticles is much higher than for gold, because of smaller non-radiative losses, gold nanoparticles are mostly used in experiments since silver oxidizes quickly destroying the plasmonic properties. [26]

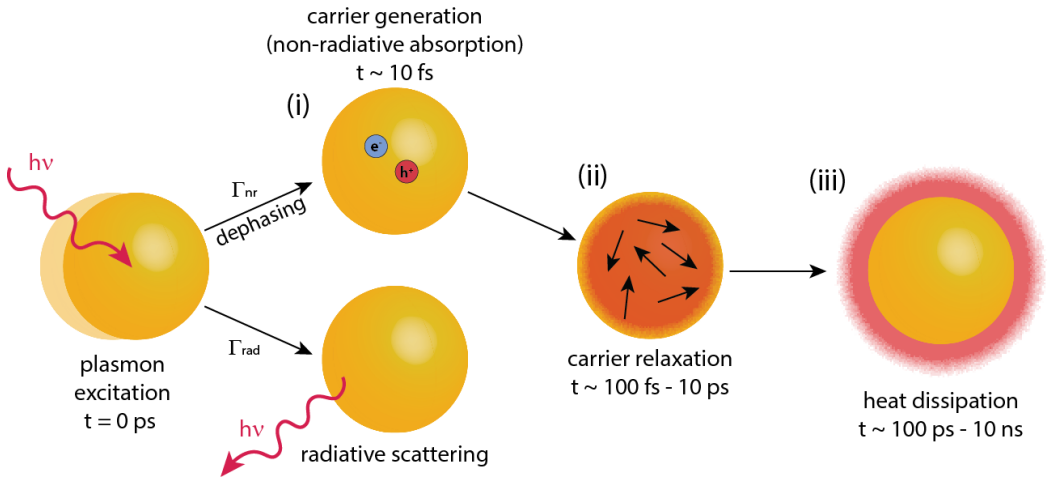

Figure 3.6 **Plasmon Decay and Hot Carrier Relaxation.** The sketch shows radiative and non-radiative decay channels. The excitation of a plasmon by an external electric field is followed by radiative and non-radiative decay processes. (i)-(iii) describes the different steps of the non-radiative decay. Adapted from Refs. [115, 116].

The radiative losses stem from photons that are send out during the plasmon decay. This process dominates the decay process of large nanoparticles with a diameter of more than 70 nm since the scattering cross section is proportional to the square of the volume, Eq. (3.19). [108, 114]

Γ_b and Γ_{surf} are non-radiative, internal losses that are based on the generation of hot charge carriers (electron-hole pairs) during the plasmon decay. Thereby, the hot electrons are located above the Fermi energy and the holes below the Fermi level. These non-radiative losses are proportional to the absorption cross section, Eq. (3.20), that scales only linear with the volume of the particle. Thus, the non-radiative decay channels dominate for the smaller particles where the surface-to-volume ratio is large.

Γ_b are losses that occur from inter- and intraband transitions in the bulk material creating hot electrons. [114] The bulk damping rate depends only on the dielectric function of the material [110]

$$\Gamma_b = \frac{2\mathrm{Im}[\epsilon(\omega)]}{\frac{\partial}{\partial\omega}\mathrm{Re}[\epsilon(\omega)]} \tag{3.22}$$

and gives the minimum damping of the system. It increases strongly at the onset of the interband transitions. Equation (3.22) shows that metals with small imaginary part of the dielectric function are preferred to obtain narrow resonances. On the other hand surface damping (Γ_{surf}), also known as Landau damping, occurs due to electron-surface (plasmon) collisions which depend on the particle size, the Fermi velocity, and the surrounding environment. [110, 111, 117] During this collision an electron hole pair is created. [118]

The carrier generation (i) in the non-radiative decay process is followed by the relaxations (ii,iii). The relaxation process of the hot electrons includes different types of scattering events on a time scale between 100 fs and 10 ns that are independent of the particle size, Fig. 3.6. [119] In the time frame (ii) of 100 fs - 10 ps after the excitation of the plasmon electron-electron scattering and electron-phonon coupling dominate the redistribution process. In this phase the hot electrons above the Fermi level collide with electrons below, transferring some energy. Further, the collision of electrons with the ionic core of the nanoparticle metal lattice leads to the heating of the particle. On a timescale (iii) of 100 ps to 10 ns phonon-phonon scattering leads to thermal dissipation, transferring heat to the environment. [108,115,116,120]

The ratio of the radiative losses and the non-radiative losses can be obtained by the ratio of the cross sections in Eq. (3.19) and (3.20) [121]

$$\frac{\Gamma_{rad}}{\Gamma_{nr}} = \frac{C_{sca}}{C_{abs}}. \tag{3.23}$$

The cross section ratios of 60 nm and 100 nm gold sphere of Fig. 3.4 are calculated and shown in Fig. 3.7. For the 60 nm sphere the ratio of the damping at the resonance is below 1 while for the larger sphere it is above 1, showing that the radiative damping is smaller or larger than the non-radiative damping depending on the particle size/volume. Since the majority of gold nanospheres is smaller than 100 nm the radiative scattering for gold nanoparticles is mostly larger than the non-radiative scattering.

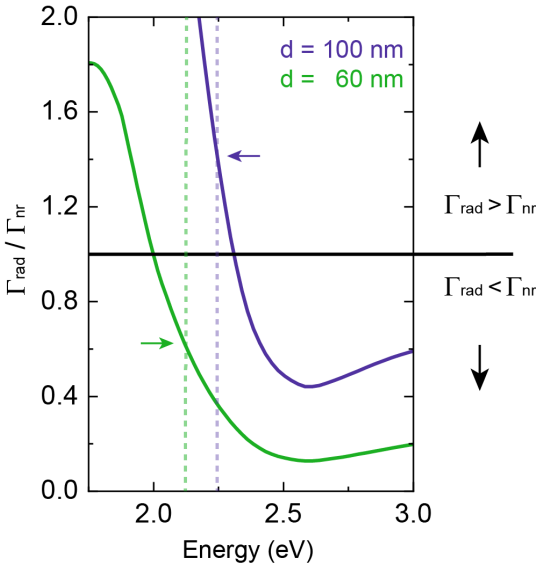

Figure 3.7 **Ratio of Radiative and Non-Radiative Damping.** The plot shows the ratio of the radiative damping and the non-radiative damping for a 60 nm (green) and 100 nm (blue) gold sphere. For the 60 nm sphere non-radiative damping dominates and for the 100 nm the radiative damping. The dotted lines show the resonance frequency for both particle sizes.

The different decay channels of the plasmons can be tuned depending on the purpose they will be used for. [111] Decreasing radiative damping, for example, benefits the hot electron generation which is preferred for many catalytic experiments. [111, 122]

So far the discussed properties of plasmonic nanoparticles account for single particles. When two or more particles are brought into close proximity they start to couple and new interesting features arise that can be used for optical experiments.

3.1.5 Plasmon Coupling

Like molecules, plasmons can couple *via* their dipole moment (Coulomb coupling) creating a hybridized system. [123–125] Assuming two single plasmonic structures that couple to a dimer, the excited state splits into four plasmon modes, Fig. 3.8a. Two of the modes are optically allowed "bright" modes (b1,b2) where the dipoles are pointing into the same direction, either in a parallel configuration (b1) or in a "head-to-tail" configuration (b2). [126] These modes correspond to the H- and J-aggregate of coupled molecules, respectively, and can easily be activated by the illumination with linear polarized light from the top either perpendicular or along the dimer axis. The excitation of the mode labeled by (b2) is essential for a row of experimental methods like surface- (SERS) and tip-enhanced Raman spectroscopy (TERS), or photocatalysis.

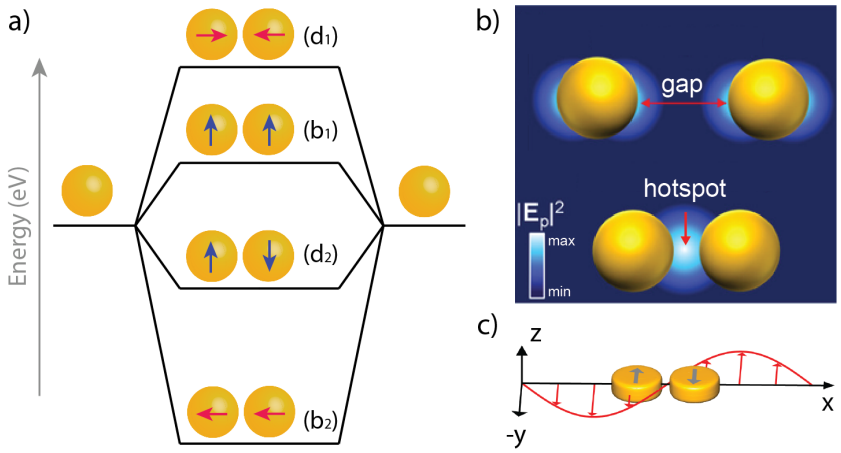

Figure 3.8 **Dimer Coupling in Plasmonic Structures. a)** Hybridization diagram of two nanospheres showing a splitting into four plasmon modes. **b)** Coupling of two gold nanospheres generating a hotspot in between. The hotspot intensity depends on the distance between the spheres. The arrow indicates the polarization along the dimer axis. **c)** Side illumination of a dimer with linear polarized light, exciting the dark plasmon mode (d2). Adapted from Refs. [107, 126].

The strong confined electric fields that build up in between the particles when excited by light polarized along the interparticle axis are so called hotspots, Fig. 3.8b.

They can for example enhance the signal of a weak Raman scatterer by a factor of 10^4-10^6, [115] making it possible to measure single molecules under special conditions. [26, 127] Likewise, the catalytic activity of metals can be increased in the hotspots. [24] The closer two plasmonic particles are packed together the stronger the electric near field becomes. [128] The coupling and the packing of the particles further influences the plasmon resonance. The coupling of the plasmons leads to a red shift in the resonance, Fig. 3.8a, due to the energetic lowering of the state. The shift increases the stronger the coupling between the particles, *i.e.*, the closer the particles are packed. [125, 129]
The other two modes that are created due to hybridization are "dark" modes (d1,d2) that show a narrower line width and a longer life time due to the absence of radiative losses. They exhibit a total net dipole moment that is zero. The dark modes do not interact with the far field and can, therefore, normally not be excited by unpolarized or linear polarized light. [130–132] To activate the dark plasmon modes with light incident to the normal it needs structured light with a polarization that fits to the respective sample structure or specially designed nanostructures that break the symmetry. [130, 131, 133] With linear polarized light the dark plasmon modes of a dimer can only be excited from the side, Fig. 3.8c. [134] Another system that allows the activation of dark modes *via* linear polarized light are plasmonic supercrystals that consist out of nanoparticle layers. [126] This system breaks down the quasi-static approximation that the wavelength is much larger than the plasmonic system so that the external field is no longer constant over the whole material. Therefore, the symmetry-derived selection rules are not valid anymore and the excitation of the d2-mode in Fig. 3.8a becomes possible with linear polarized light with normal incident. [126, 132]
So far the general concepts of plasmonic systems were introduced. In the following section different light matter coupling regimes will be discussed. Further, I will introduce nanoparticle supercrystals as one interesting plasmonic system that will later be used in the context of photocatalytic experiments. I will give a short overview about the synthesis of the crystals as well as on their optical properties.

3.2 Nanoparticle Supercrystals

Ordered supercrystals can be synthesized out of single plasmonic nanoparticles that are stabilized by polystyrene ligands, *cf.* Sec. 3.2.2. [12, 135] These supercrystals

consist of stacked layers of nanoparticles and change their optical properties due to the crystal thickness. [23, 126] When the particles are closely packed these supercrystals can show a form of very strong light-matter coupling. [10] In this section, I will first introduce the different types of light matter coupling and how they can be distinguished. Further, an introduction into the field of gold nanoparticle supercrystals and their optical properties will be given.

3.2.1 Light-Matter Coupling

Depending on the strength of interaction light-matter coupling is divided into different regimes, Fig. 3.9. The first two regimes are defined by the coupling constant g and the losses γ of the system. In the weak coupling regime, Fig. 3.9a, the coupling constant is smaller than the losses. A famous effect in this regime is the Purcell effect. [136] Here, the spontaneous emission of an emitter is increased by a resonant cavity. Optical cavities are also used to reach the strong coupling regime, Fig. 3.9b, by reducing losses or increasing the coupling strength

$$g \propto \sqrt{\frac{f}{V_m}}, \tag{3.24}$$

where f is the oscillator strength of the material filling the cavity and V_m the mode volume of the cavity. [137, 138] In the strong coupling regime the coupling constant g is comparable to the amount of losses or larger and light and matter are no longer considered as separate entities. They form a hybridized system with an upper and lower polariton. The energy splitting is called Rabi-splitting and is twice the coupling constant g. [137] For both coupling regimes the ground state of the system remains unchanged. This will differ for the regimes explained next.
The last two regimes are ultrastrong coupling, Fig. 3.9c, and deep strong coupling, Fig. 3.9d. The coupling strength is no longer compared with the losses of the system but with the excitation frequency ω. The ultrastrong regime is reached if $g \geq 0.1\omega$ and the deep strong coupling is reached for $g \geq \omega$. [10] To realize ultrastrong coupling usually more than one oscillator needs to be inserted into a cavity leading to collective interactions. Often the whole cavity is filled. For molecules this regime can already reached when up to 1000 molecules in a cavity couple. [140] In this case the coupling strength scales with the square root of the number of oscillators ($g_{USC} = \sqrt{N} g_{mol}$). [141–143]

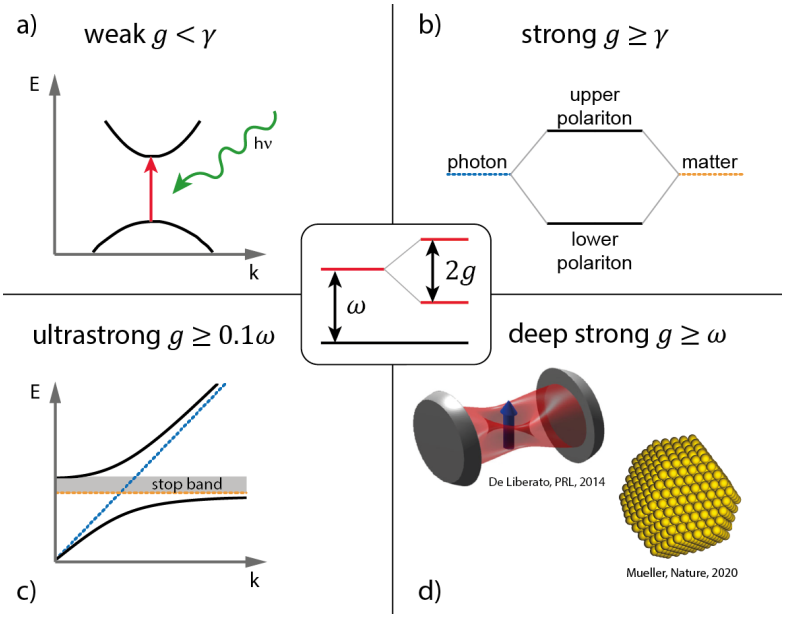

Figure 3.9 **Light-Matter Coupling Regimes.** Overview of the different coupling regimes of light and matter, from weak to deep strong coupling. The graphics in d) are adapted from Refs. [10, 139].

One system that realizes the deep strong coupling are gold nanoparticle supercrystals. Since the crystals have quite large spatial extent the light-matter interactions are even strong enough that no cavity is needed. Additionally, gold nanoparticles have a large oscillator strength because of the large number of conduction electrons which makes them ideal building blocks of a material entering the deep strong coupling regime. [10] Due to the outstanding light-matter coupling and the resulting optical properties, that will be discussed next, the supercrystals are very interesting systems for a variety of experiments like surface enhanced Raman spectroscopy or photocatalysis since they are relatively large and can be tuned for the respective requirements. [24] Besides the variation of the particle and gap size, the mixing of different particles sizes or materials can tune the crystals. Further, molecules can be included into the supercrystal or the shape of the particles that form the crystal can be changed, *e.g.*, to cubes. [144, 145]

3.2.2 Supercrystals - Synthesis and Structure

Supercrystals are built of single gold nanoparticles that are stabilized by thiol-terminated polystyrene. The particles are grown by a seeded growth method. That

is followed by a ligand exchange to obtain the polystyrene covered particles for the crystal. [10, 12, 135] The ligand covers the particles in a kind of micelle or brush. The choice of the ligand is thereby very important. Not every ligand can stabilize large particles. Further, the length of the ligand defines the gap size between the particles. A transmission electron microscopy image of seed grown particles is shown in Fig. 3.10a.

The crystals are formed in a self-assembly process on a liquid-liquid interface, Fig. 3.10b. Therefor, the gold nanoparticles in toluene were added in a little well with diethylene glycol (EG). Both solutions do not mix creating a clear phase separation. In the next step, the well is covered with a cover slip to ensure a slow evaporation of the toluene. After 16-24 h the toluene is evaporated and highly ordered self-assembled thin films of gold nanoparticles are floating on the diethylene glycol surface that can be fished out of the liquid by, *e.g.*, a glass slide or transmission electron microscopy grid. [12]

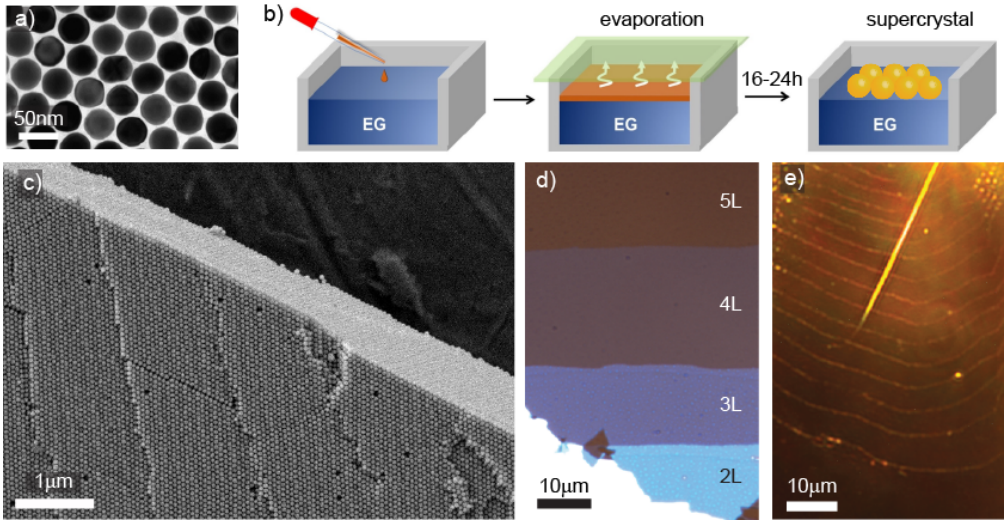

Figure 3.10 **Nanoparticle Supercrystals: Synthesis and Structure. a)** Transmission electron microscopy image of a single layer of hexagonally packed gold nanoparticles. **b)** Crystalization process of the supercrystal. **c)** Scanning electron microscopy image of a crystal edge showing different number of layers. **d)** Microscopy image in transmission mode. The different blue tones indicate different layer numbers. **e)** Dark field microscope image of a supercrystal. The light scattering on the layer edges enables the counting of the layer number. Adapted from Refs. [10, 24, 146].

The hexagonally packed thin films range from monolayers up to thick crystals of 18 or even more layers that build up a face center cubic (fcc) lattice structure. [10] An

exemplary scattering electron microscopy image of a gold supercrystal is shown in Fig. 3.10c. It shows an edge of a crystal with increasing number of gold nanoparticle layers. Experimentally the thickness of thinner crystals can easily be determined by transmission microscopy, Fig. 3.10d, due to different blue hues. For thicker crystals dark field microscopy can be used to identify different layers due to the light scattering of the layer edges, Fig. 3.10e. [10]

3.2.3 Optical Properties of Gold Supercrystals

The light-matter interaction in a gold nanoparticle supercrystal can lead to a coupling strength that is located in the deep strong coupling regime if the particles have a certain size and are closely packed. [10] The coupling in the crystal results in the creation of an upper and a lower transversal plasmon-polariton branch in the dispersion relation of the crystal due to the anti-crossing of the photon and plasmon dispersion, Fig. 3.11a. [147] Since the upper polariton branch is located above the onset of the gold interband transitions, where all light is absorbed, it is not accessible. Both branches are separated by a stop band (Reststrahlenband) in which no dipole-active states are located, Fig. 3.11a. [10]

The optical response of a nanoparticle supercrystal changes with the number of particle layers. In general three different regions can be observed in the optical spectra of the crystals: (i) the interband transitions of gold, (ii) a polaritonic stop band and, (iii) polaritonic modes, Fig. 3.11b. [10] The absorption peaks in range (iii) correspond to the standing waves of the plasmon-polaritons in the nanoparticle crystal that fulfill the open cavity boundary conditions which depend on the thickness of the crystal. Thus, only certain polaritonic wavelengths (λ_{pp}) that are compatible with the crystal thickness can travel and transmit light through the crystal, Fig. 3.11c. They are given by [126]

$$\lambda_{pp} = \frac{2h}{j} \text{ with } j = 1, 2, ..., N_L - 1, \tag{3.25}$$

where h is the total thickness of the crystal, j an integer, and N_L the number of gold nanoparticle layers. With increasing number of particle layers more polaritonic modes are allowed due to the large optical thickness. This results in additional peaks and red shifts in the absorption spectrum. [23, 126]

In the polaritonic stop band (area ii) light cannot enter the crystal due to missing

electromagnetic states at these energies, so no plasmon-polaritons can be excited inside the supercrystal in that range. [10] It is interesting and useful for sensing experiments in the visible spectral range that the top layer shows a strong field enhancement in the stop band while the enhancement of the bulk is suppressed in this spectral range, Fig. 3.11d. [23] The reason for that are higher-order plasmonic resonances that do not depend on the crystals boundary condition. [23] In the near infrared the field enhancement of the surface follows the one of the bulk material with maxima at plasmon-polariton resonances which lead to a strong excitation-wavelength dependence. [23]

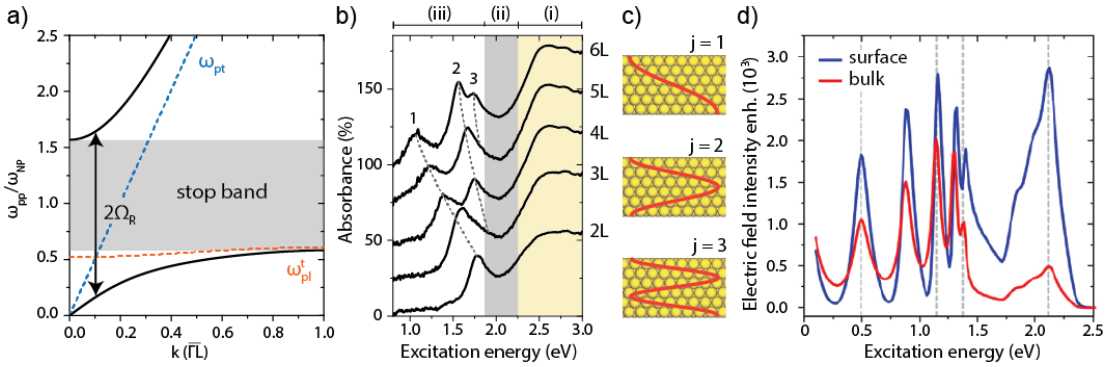

Figure 3.11 **Optical Properties of Plasmonic Supercrystals. a)** Plasmon-polariton dispersion (black lines) of a nanoparticle supercrystal along the ΓL direction of an fcc crystal. Light-matter coupling leads to an anti-crossing of the photon (blue) and plasmon dispersion (orange) resulting in a stop band (gray area). **b)** Absorption spectra of a supercrystal with 30 nm gold nanoparticles and changing layer number (L). Offset by 25 % increments. **c)** Standing waves in the supercrystal that belong to the peaks of the absorption spectra in b). **d)** Field enhancement in the interparticle gaps at the crystal surface and in the bulk for a supercrystal out of 60 nm gold nanoparticles. In addition to the polariton resonances, a strong field enhancement occurs at the surface in the spectral range of the stop band. Taken and adapted from Refs. [10, 23].

The optical transmittance (T) and reflectance (R), and therefore, the absorption $A(\%) = 100\% - T(\%) - R(\%)$ of the crystals can be calculated from the dielectric function obtained by the Lorentz model [10]

$$\epsilon_L(\omega) = \epsilon_\infty + \frac{f'\omega_{pl}^2}{\omega_{pl}^2 - \omega^2 - i\gamma\omega}, \tag{3.26}$$

where ϵ_∞ is the high-frequency dielectric constant, f' is the reduced oscillator

strength, ω_{pl} the plasmon resonance frequency, and γ its line width. Using the approach that the supercrystal is an open cavity in which radiative damping occurs due to cavity losses in addition to the intrinsic loss γ the optical spectra can be calculated by [10]

$$T = \left| \frac{4ne^{ihn\omega/c}}{(1+n)^2 - (1-n)^2 e^{2ihn\omega/c}} \right|^2 \tag{3.27}$$

and

$$R = \left| \frac{(1-n^2)(1-e^{2ihn\omega/c})}{(1+n)^2 - (1-n)^2 e^{2ihn\omega/c}} \right|^2 \tag{3.28}$$

where $n = \sqrt{\epsilon_L}$ is the refractive index of the material, h the thickness of the crystal, and c the speed of light.

3.3 Plasmons for Catalysis

In chemistry substances that trigger or increase chemical reactions are widely used, they are called catalysts. The catalyst decreases the activation barrier of a chemical reaction and remains unchanged during the reaction. [148] Over the last decades plasmonic structures became an important factor in the field of catalysis either used as catalyst or as supportive substrate, Fig. 3.12. [149] The previously discussed properties of plasmonic materials are ideal to trigger and boost chemical reactions.

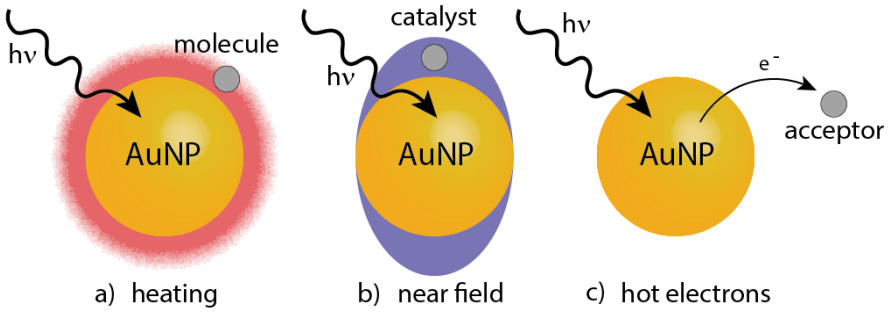

Figure 3.12 **Different Catalytic Pathways Induced by Gold Nanoparticles. a)** Reduction of thermal activation barrier. **b)** Boosting the activity of a traditional catalyst by the near-field of a nanoparticle. **c)** Electron transfer to an electron acceptor. Adapted from Ref. [156].

For example, the heat produced during plasmon decay can reduce the thermal barrier for chemical reactions, Fig. 3.12a, [150] or the strong electric field in the gaps between plasmonic particles can increase the hot carrier production in traditional

catalysts like platinum or palladium that are placed in the hotspot, Fig. 3.12b, since the production of the carriers is proportional to the internal field-intensity enhancement. [151,152] Further, the hot carrier generation by non-radiative plasmon decay can lead to the transfer of a hot electron from the nanoparticle into a nearby electron acceptor, *e.g.*, a molecule, Fig. 3.12c, either directly or indirectly. [153,154] The fact that the plasmon resonance for the majority of gold and silver nanoparticles is located in the visible regime, and not in the UV like for the traditional semiconductor or transition metal (platinum, palladium) catalysts, makes them ideal candidates for photocatalytic experiments that are activated with white light illumination or sunlight. [155]

In Chapter 7, I will focus on the use of bimetallic supercrystals for photocatalyis. It is shown that this new substrate enhances the H_2 production rate in the catalytic decomposition of formic acid immensely due to its near fields.

4 | Preparation, Characterization, and Numerical Methods

This chapter introduces and explains the experimental methods to produce the different types of samples used in this thesis as well as the setups used to study their optical properties. In the last part of the chapter, a short introduction into a numerical approach is given that was used to calculate the optical spectra and electric fields of the plasmonic supercrystals.

4.1 Sample Preparation

Three main types of different samples were studied in this thesis. In Chapter 5 the optical properties and behavior of collective states of two-dimensional molecular lattices are investigated. Chapter 6 probes single- and multi-file one-dimensional molecular chains encapsulated in boron-nitride tubes, and in Chapter 7 bimetallic plasmonic supercrystals are studied for the usage of H_2 production. The synthesis and preparation of the used samples will be discussed in this section.

4.1.1 Two-Dimensional Molecule Layers

The sample production of a two-dimensional molecule layer on a support is a two-step process. First, the substrate with the support is prepared by mechanical exfoliation followed by physical vapor deposition of the molecules. A main task of my research was to build up the physical vapor deposition system and to find the optimal parameters to grow monolayers of organic molecules onto different van der Waals materials.

Mechanical Exfoliation

The sample preparation for the study of collective states in molecular monolayers was done by cleaving layered materials with sticky tape into few-layers and transferring them onto a substrate. Therefor, the sticky tape was attached to the surface of a crystal of layered material. By peeling of the tape, the van der Waals forces are overcome and the top few layers of the material stuck to the tape. To obtain flakes of a few layers or even a single layer the process was repeated by pressing another piece of tape onto the first tape. For the deposition of the molecules the thickness of the material below has not a large effect but the micro-absorption measurements described in Sec. 4.2.3 are easier to perform on thinner flakes that give only a small background. In the last step the sticky tape was pressed onto a substrate to transfer the few-layers of the two-dimensional material from the tape to the substrate.
As substrate quartz or Si/SiO_2 wafers were used. They are heat resistant which is needed for the deposition of the molecules. Further, quartz substrates are transparent which is necessary for the micro-absorption measurements.

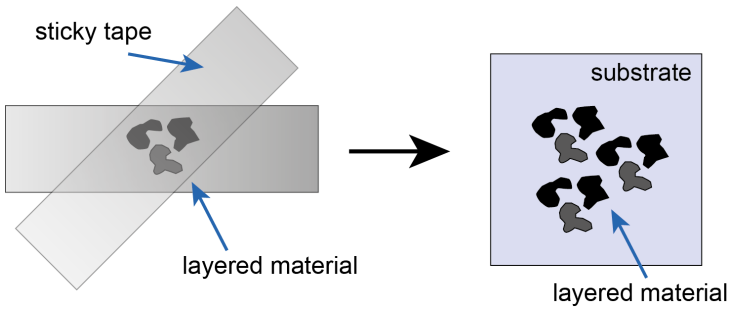

Figure 4.1 **Sketch of the Mechanical Exfoliation Process.** The layered material is picked up and cleaved with a scotch tape before exfoliated onto the substrate.

Physical Vapor Deposition

Physical vapor deposition (PVD) was used to prepare the molecule monolayers on different types of van der Waals materials. The first step describes the baking process to clean the substrate from water and any other residuals that arise from the exfoliation process to ensure a growth process on a smooth surface for optimal results. The sample with the two-dimensional material is placed in the middle of the tube furnace (*Heraeus*) where the temperature is the highest and is heated up

under vacuum (10^{-3} bar) for one hour at 400°C. An example image (a) before and (b) after the baking procedure is shown in Fig. 4.2. It shows the reduction of the disturbing residuals in the left part of the image.

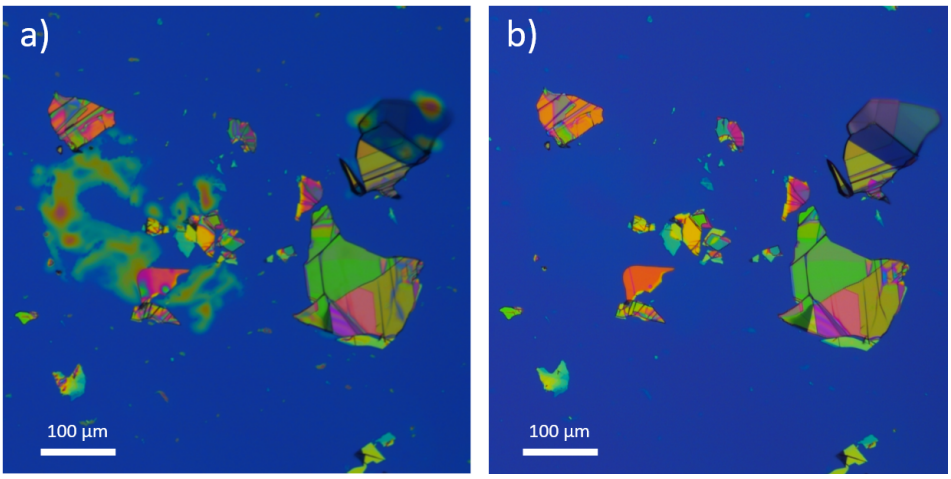

Figure 4.2 **Cleaning Procedure after Exfoliation.** Exfoliated hBN flakes of different thickness **a)** before and **b)** after baking out the sample for one hour at 400°C. It shows that the residues on the left side in panel a) disappeared after the heat treatment.

When the furnace is cooled down to ∼ 100°C the substrate is shifted toward the end of the glass tube and an evaporation boat with a small amount of organic molecules (source) is placed in the middle of the tube furnace, Fig. 4.3. A set of different parameters is important for the successful growth of a molecular monolayer. The parameters that influence the growth are the flow constant of the inert gas, the temperature, the time, and the distance between the molecule source and the substrate.

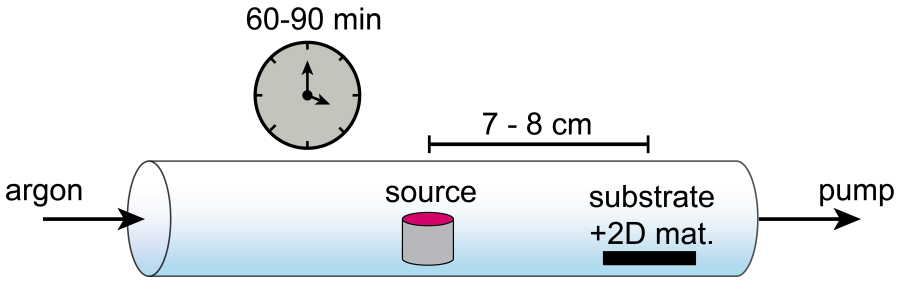

Figure 4.3 **Sketch of the PVD Setup.** The evaporation boat with the molecules (source) is placed in the middle of the tube furnace and the exfoliated support on the substrate is placed at the end of the tube.

The right evaporation temperature of the molecules was found with the help of thermal gravimetric analysis (TGA) measurements that show at which temperature the molecules start to lose weight due to the breaking of bonds and the loss of atoms or side chains. As growth temperature 230°C was chosen that lies slightly below the degradation temperature of the MePTCDI molecules. [157, 158]

To find the right combination of the remaining parameters with the set temperature a vast number of growth attempts were carried out and pre-characterization of the samples by imaging the emission of the molecule layers was done. Therefor, I built up a fluorescence microscope (*cf.* Sec. 4.2.1) that quickly gives a good insight into the layer number, homogeneity, and size of the molecule layer(s). In the beginning no molecules or only a very few adsorbed to the hBN, tending to multi-layer growth (red fluorescence), Fig. 4.4a. After a series of experiments it turned out that placing the substrate 7-8 cm away from the molecule source yields the highest rate of adsorbed molecules, and a tendency towards monolayers was recognizable (green emission), but the spatial extent of the layers was clearly smaller than the flake, Fig. 4.4b. It is important to note that for molecular deposition it is necessary to have a temperature gradient towards the sample so that the molecules adsorb onto the surface. Therefore, the substrate is shifted towards the furnace end for the growth process.

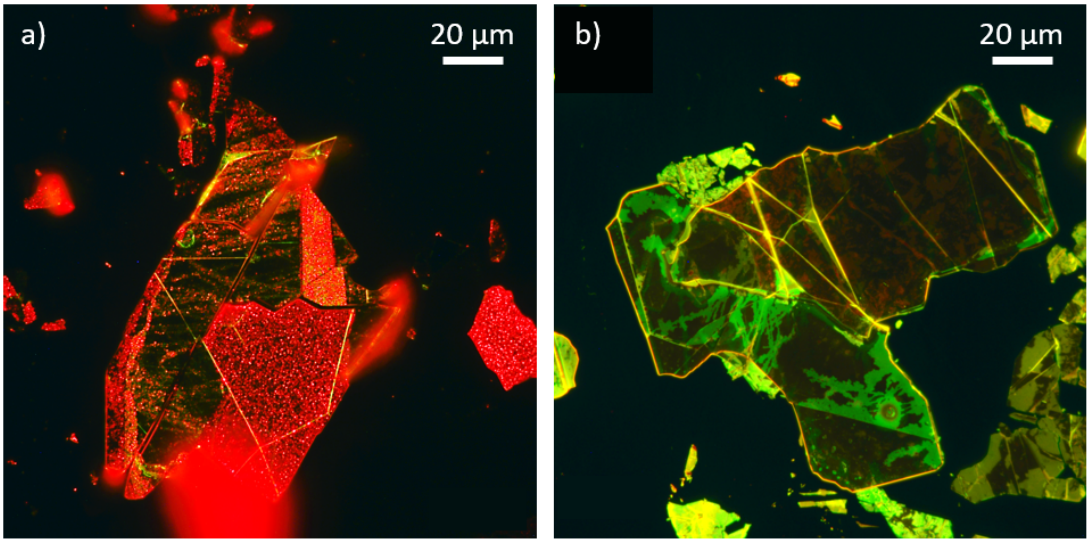

Figure 4.4 **Fluorescence Images of MePTCDI on hBN - First Growth Runs. a)** Inhomogeneous distribution of molecules that tend to $\pi-\pi$ stacking (red emission). **b)** Partial monolayer growth of MePTCDI molecules (green emission).

Another idea that I followed to optimize the growth was the orientation of the sample with respect to the gas flow. I crafted different sample holders to realize different sample orientations. Besides horizontally, I placed the sample upright, front face, and sideways to the flow direction of the inert gas. It turned out that the flat laying samples showed the best tendency towards monolayer formation. Thus, for all further runs I placed the samples flat in the furnace.
With knowing the right source-to-substrate distance and sample placement different growth times were tried out to realize large-scale and homogeneous monolayers that cover whole flakes of hBN. For too long growth times I observed either flakes that show red emission indicating two or more molecule layers, Fig. 4.5a, or I observed crystalline looking bulk growth, Fig. 4.5b. Between 60 min and 90 min I usually observed the layers that showed besides homogeneously covered hBN flakes the brightest and narrowest emission, Fig. 4.5c, indicating a monolayer.

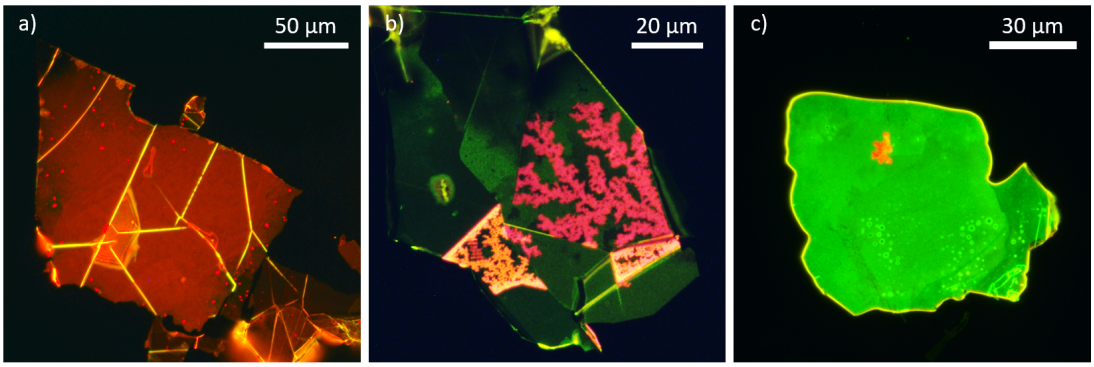

Figure 4.5 **Fluorescence Images of MePTCDI on hBN - Process of Finding the right Growth Parameters. a)** Multi-layer, **b)** bulk crystal seed, and **c)** monolayer of MePTCDI molecules. Identified by the color of the florescence.

The strength of the argon flow that is used to transport the evaporated molecules to the substrate seemed not to change the result dramatically but ensured a homogeneous growth. The flow rate was regulated by a mass flow meter (*Omega - FMA-2619A*) which was typically set to 100 sccm. The whole evaporation and deposition process is done under vacuum (10^{-3} bar) to minimize molecule collisions with atoms in the atmosphere.

4.1.2 Encapsulation of 6T Molecules in BNNTs[1]

For the experiments in Chapter 7 rod shaped thiophene-based α-sexithiophene (6T) molecules were encapsulated in boron nitride nanotubes (BNNTs), Fig. 4.6. In a first step for cleaning and opening the BNNT powder was annealed for 2 hours at 800°C under ambient conditions and afterwards sonicated in dimethylformamide (DMF) using a cup sonicator until complete dispersion was observed. In the next step, the BNNT solution was centrifuged at 12000g and the top half of the centrifuge tube was collected and filtered by a polytetrafluoroethylene (PTFE) membrane with a pore size of 0.22 μm.

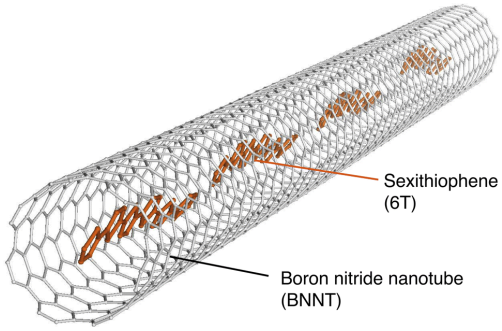

Figure 4.6 **6T Molecules Encapsulated in a BNNT.** Schematic of a single chain of head-to-tail aligned 6T molecules in a single walled BNNT. Taken from Ref. [159].

The encapsulation was done under reflux for 48h at 85°C by mixing the 6T molecules and the cleaned BNNTs with toluene in a round-bottom flask equipped with a condenser. Thereby, the concentration of the 6T was fixed at 5×10^{-6} M. Intense DMF rinsing of the solution on a PTFE membrane (pore size 0.22 μm) was applied to remove non-encapsulated 6T molecules. Afterwards soft piranha solution treatment was done to remove the last free 6Ts and the 6Ts that were adsorbed on the outer wall of the BNNTs.

To dispose the 6T@BNNTs *via* spin coating onto a Si/SiO_2 substrate, the 6T@BNNTs were dispersed in DMF. Before disposition the Si/SiO_2 substrate was sonicated 10 min in acetone and 10 min in isopropanol for cleaning.

[1]Parts of this section were submitted as *Collective States of α-Sexithiophene Chains Inside Boron Nitride Nanotubes* in Juergensen et al. Nano Lett. (July, 2024). The encapsulation was developed and performed by J.-B. Marceau and E. Gaufrès.

4.1.3 Synthesis of Gold-Platinum Nanoparticle Crystals[2]

The synthesis of the gold-platinum supercrystals, that I use in Chapter 7 to study the catalytic activity, is a three-step process. First, the gold particles are synthesized followed by the synthesis of platinum particles and in the last step both types of nanoparticles are assembled to a binary crystal in a self-assembly approach.

Synthesis of Gold Nanoparticles (AuNPs)

AuNPs were synthesized based on the seeded growth protocol from Zheng *et al.* [160] and functionalized with thiolated polystyrene (PSSH) as described previously in Ref. [12]. Several batches were prepared: AuNPs with a core diameter of $\langle D \rangle = (22.0 \pm 1.0)\,\mathrm{nm}$ and a particle concentration of $c = 9.5\,\mathrm{nM}$ were functionalized with PSSH2k (molecular weight $2000\,\mathrm{g\,mol^{-1}}$ - 2k). AuNPs with $\langle D \rangle = (39.0 \pm 1.0)\,\mathrm{nm}$ and $c = 2.4\,\mathrm{nM}$ and AuNPs with $\langle D \rangle = (38.7 \pm 0.9)\,\mathrm{nm}$ and $c = 2.0\,\mathrm{nM}$ were functionalized with PSSH5k (molecular weight $5000\,\mathrm{g\,mol^{-1}}$ - 5k) and AuNPs with $\langle D \rangle = (35.5 \pm 1.0)\,\mathrm{nm}$ and $c = 2.6\,\mathrm{nM}$ were functionalized with PSSH5k as well as with PSSH2k.

Synthesis of Platinum Nanoparticles (PtNPs)

PtNPs with $2.8 \pm 0.5\,\mathrm{nm}$ in diameter were synthesized as follows: $500\,\mu\mathrm{L}$ of hexachloroplatinic acid (H_2PtCl_6) 0.05 M were added to 8.6 mL of ultra-pure water (stirred at 500 rpm), succeeded by the addition of $500\,\mu\mathrm{L}$ of sodium citrate 0.1 M, which served as the stabilizing agent. The Pt precursor was reduced upon quick addition of $500\,\mu\mathrm{L}$ of sodium borohydride ($NaBH_4$; 0.015 M), evidenced by the dark brown color of the final solution. Finally, the solution was left undisturbed for 10 minutes. [161]
The as-synthesized PtNPs were functionalized with PSSH2k by phase transfer as described in a previous report in Ref. [135]. In detail, the aqueous PtNPs dispersion ($1000\,\mu\mathrm{L}$) was mixed with PSSH2k ($1100\,\mu\mathrm{L}$, 0.18 mM) in toluene and ethanol ($1000\,\mu\mathrm{L}$). After vigorous shaking, phase separation was facilitated by addition of some mg sodium chloride. The toluene phase with the PtNPs was then carefully

[2]Parts of this section were published as *Plasmonic Bimetallic Two-Dimensional Supercrystals for H_2 Generation* in Herran and Juergensen et al. Nature Catalysis **6**, 1205–1214, DOI: 10.1038/s41929-023-01053-9 (2023). The colloidal synthesis was done by M. Herran, A. Sousa-Castillo, and F. Schulz. The colloidal assembly was developed and performed by F. Schulz.

removed and used for self-assembly experiments without further purification. The PtNPs had a diameter of 2.7 ± 0.6 nm and the platinum concentration in the final dispersion in toluene was 9.6 mg/L corresponding to 65 nM particle concentration.

Self-Assembly

Self-assembly of pure and mixed samples of polystyrene-functionalized NPs took place on diethylene glycol (EG) as a liquid subphase, described previously in Sec. 3.2.2. [12, 162] Different volume ratios of AuNP@PSSH and PtNP@PSSH2k were pipetted onto the EG and the sample cell was covered with a glass cover slip to slow down the evaporation of the toluene. After 16-24 h crystalline films had formed, which were carefully skimmed of with TEM grids or transferred to indium tin oxide (ITO) substrates for catalysis experiments. The samples differed in platinum loading and resulting interparticle spacing, Fig. 4.7. For the controls, just AuNP@PSSH or just PtNP@PSSH2k were used accordingly.

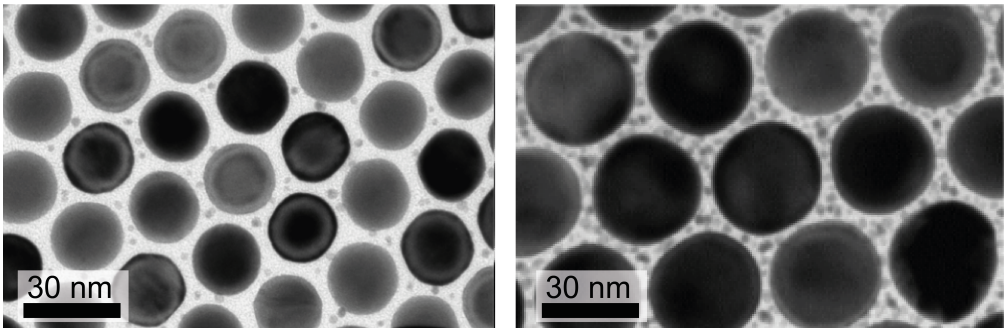

Figure 4.7 **Transmission Electron Microscopy Images of Crystalline Bimetallic Monolayers. a)** 22 nm AuNPs and **b)** 35 nm AuNPs with different amount of platinum loading in the gaps of the supercrystal. Adapted from Ref. [24].

4.2 Characterization Experiments

For the optical characterization of the above described samples, different microscopic and spectroscopic methods were used. This chapter will give an introduction to the most important characterization tools that I used during the study. All measurements were performed under ambient conditions if not noted otherwise.

4.2.1 Fluorescence Microscopy

Fluorescence images for the pre-characterization of molecule layers were taken with a *Nikon Eclipse LV 100* microscope in bright field configuration. A sketch of the experimental setup is shown in Fig. 4.8. A halogen lamp serves as illumination source. The white light of the halogen lamp is guided through a band-pass filter. For the imaging of the MePTCDI emission a *Thorlabs - FLH532-4* band-pass filter was used. The filter transmits only a narrow wavelength range (FWHM 4 nm) in the green around 532 nm and reflects all other wavelengths. The transmitted green light is collected by an objective and focused onto the sample. The by the sample emitted and reflected light passes through a long-pass filter *(Thorlabs - FELH0550)* that is mounted in the imaging path in front of the camera. The filter cuts off the exciting green light that is only scattered by the sample and passes the emitted light at longer wavelength. A high definition color camera *DS-Ri2* from *Nikon* records the fluorescence images.

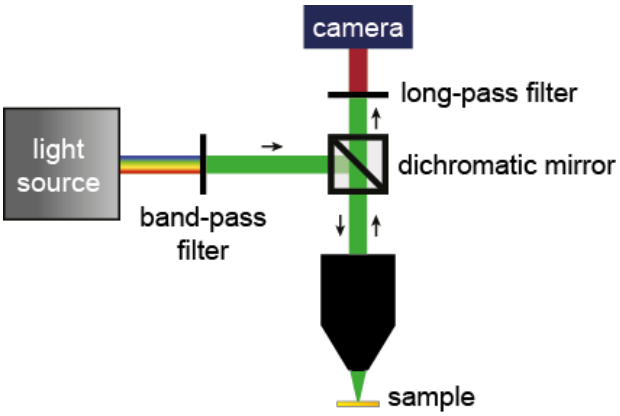

Figure 4.8 **Sketch of the Functional Principle of a Fluorescence Microscope.** A band-pass filter is used to illuminate the sample with light of the requested wavelength and a long-pass filter to cut off the reflected light and transmit the by the sample emitted light imaged by the camera.

4.2.2 Fluorescence and Raman Spectroscopy

The wavelength and polarization dependent fluorescence and Raman measurements of the two-dimensional molecular crystals were performed with a Raman setup, illustrated in Fig. 4.9. Wavelength depended measurements were done by the use of different fully tuneable continuous-wave (CW) lasers to cover the wavelength range

from 500 nm to 750 nm. The advantage of CW lasers is the high time-averaged power and narrow line width. The setup is equipped with a solid state Ti:Sa (titanium-sapphire) ring laser (*Coherent - MBR-110*). The emission wavelength range of this laser lies between 690 nm and 1050 nm, covering the red and near-infrared region. For the visible range a ring dye laser (*Radiant Dyes - Dye Ring*) is used. As lasing medium, different wavelength specific fluorescent dyes are available. The laser dye DCM[3] is used for wavelengths between 625 nm and 675 nm and Rhodamine 6G (R6G) for the wavelength range between 560 nm and 620 nm. Both lasers are pumped by a Nd:YAG laser (*Coherent - Compass 415M-200*) with a wavelength of 532 nm. For smaller wavelengths down to the blue an Ar/Kr-laser (*Coherent - Innova 70C Spectrum*) is used.

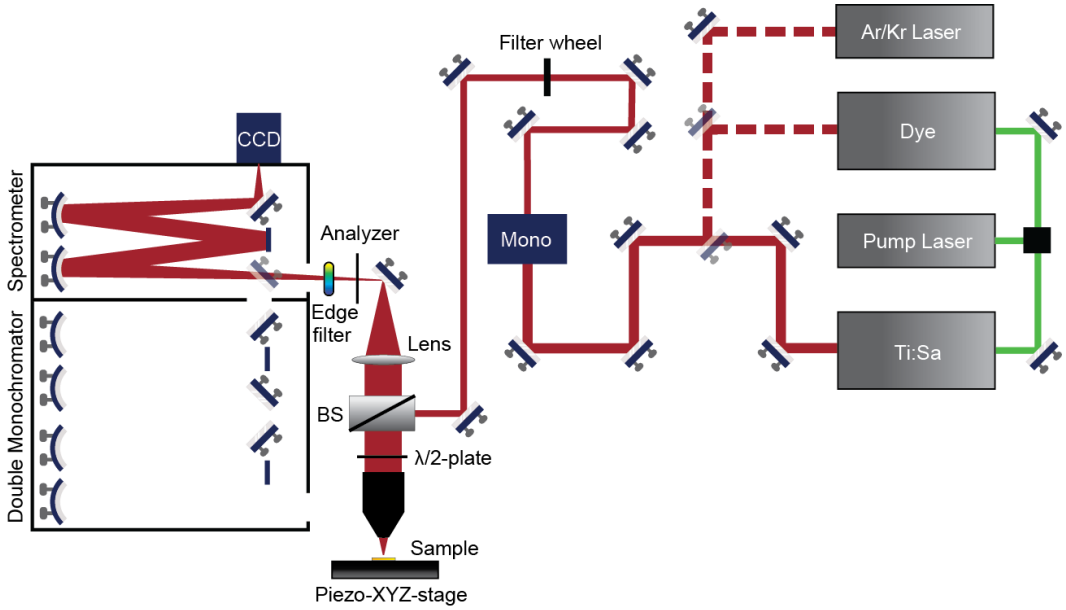

Figure 4.9 **Schematic of an open Beam-Path Raman Setup in Back-Scattering Configuration.** The setup is equipped with different tuneable lasers to perform wavelength dependent measurements.

To eliminate the Rayleigh scattered light (reflected laser beam), wavelength dependent long-pass edge filters are used. For the sample alignment, the setup is equipped with a confocal microscope (*Olympus - BX41*) with different exchangeable objectives (100x, NA=0.9 and 10x, NA=0.25), a multi-axis piezo nanopositioning/scanning stage, and a camera. Additionally, gray filters (filter wheel) are

[3] 4-(Dicyanomethylene)-2-methyl-6-(4-dimethylaminostyryl)-4H-pyran

available to regulate the laser power coming onto the sample to avoid sample damage. The inelastically scattered light is dispersed by a *Horiba Jobin-Yvon T64000* spectrometer in single-grating configuration and detected by a charge couple device (CCD) detector. To consider the polarization dependence of the spectrometer an analyzer is placed in front of the entrance slit. To further account for wavelength-dependent changes in the sensitivity of other components of the Raman setup the Raman intensity of the MePTCDI was calibrated on benzonitrile that has a constant Raman cross section. [163, 164] Since the setup is an open beam-path setup further optical elements like polarizers can be insert into the beam path to measure the polarization dependence of the samples.

For testing the homogeneity and intensity of the molecule lattices fluorescence maps were recorded using the *XploRA* by *Horiba*. The setup is composed of a standard bright field microscope (*Olympus - BX51*) with exchangeable objectives and *xy*-piezo nanopositioning stage (*PI - P-562*). Further, the microscope is equipped with three different laser diodes, allowing to excite the samples at 532 nm, 638 nm and 785 nm. For probing the MePTCDI and 6T molecules the 532 nm laser was used. The *XploRA* uses a single grating spectrometer to disperse the emitted or the inelastically scattered Raman light. The dispersed light is afterwards detected by a CCD. In contrast to the previously described Raman setup the *XploRA* is more sensitive but not equipped to record resonant Raman profiles.

4.2.3 Micro-Absorption Spectroscopy

To measure the absorption of a solid sample at a certain position, a home build micro-absorbance setup, built out of an inverse bright field microscope, was used. A schematic of the setup is shown in Fig. 4.10. A supercontinuum laser (*NKT-FIU15*) with a broad spectral range (390-2400 nm) was used as excitation source. The white light was guided to a microscope (*Olympus - IX71*) equipped with a 100× objective (NA 0.9) that focuses the light onto the sample, and a second 100× objective (NA 0.8) to collect the transmitted light (T). *Via* an optical fiber the collected light was guided to the spectrometer (*Avantes - AvaSpec-ULS2048CL-EVO* for the visible or *AvaSpec-NIR512-1.7TEC* for the IR). For the reflectance measurements the reflected light (R) was guided back through two beam-splitter (BS) to a collector lens that was connected *via* an optical

fiber to the spectrometer. Afterwards, the absorbance (A) was calculated by $A(\%) = 100\% - R(\%) - T(\%)$.

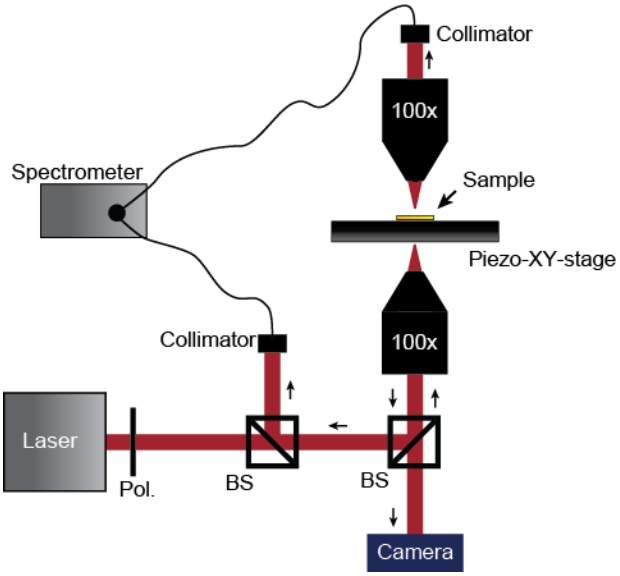

Figure 4.10 **Sketch of the Micro-Absorption Setup.** The setup enables the measurement of transmittance and reflectance to calculate the absorbance of a specific position of a solid sample. The small black arrows illustrate the back-path of the beam after sample illumination.

4.2.4 Spatial Modulation Spectroscopy[4]

The extinction (absorption plus scattering) of the filled nanotubes was measured with a home build spatial modulation setup, Fig.4.11. As excitation source a supercontinuum laser (*NKT - FIU15*) was used. The laser was coupled to a laser line tunable filter (*Photon etc. - LLTF Contrast*) to filter out single wavelengths. The laser beam was guided to an inverse microscope that was equipped with a *xy*-piezostage from PI and focused with an 100× objective (NA 0.9) to the sample. The sample was mounted in a special sample holder that was equipped with a piezo-electric element to modulate the sample position at frequency f in the focal spot of the objective. The reflected signal was collected by the same 100× objective and detected with a switchable gain detector (*Thorlabs - PDA36A2*) that was connected to a lock-in amplifier (*AMETEK - Model 7270*) to demodulate the signal

[4]Parts of this section were submitted as *Collective States of α-Sexithiophene Chains Inside Boron Nitride Nanotubes* in Juergensen et al. Nano Lett. (July, 2024).

and further to a digital voltmeter (*NI - myDAQ*) to measure the total reflection, yielding to a relative change in the reflectance $\Delta R/R$.
For the polarization dependent measurements a polarizer was inserted into the beam path before the sample and an analyzer was added in front of the detector. The analyzer was kept constant to avoid changes in the signal intensity due to the spatial sensitivity of the detector while the polarizer was rotated.

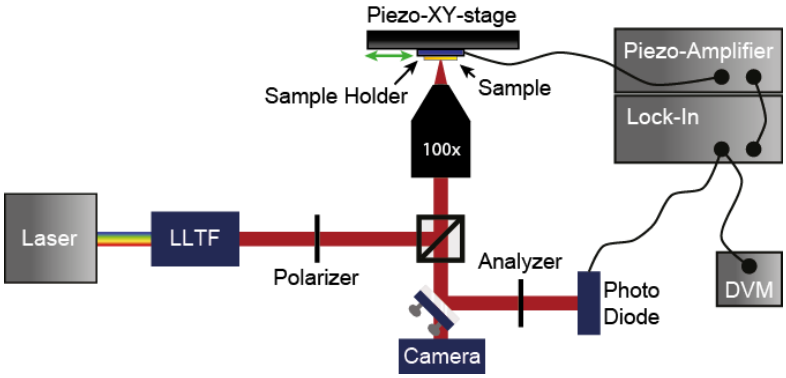

Figure 4.11 **Sketch of the Spatial Modulation Spectroscopy Setup in Reflection Mode.** The special sample holder modulates the sample position during the measurements. Demodulation of the signal by an lock-in amplifier gives the extinction. The LLTF allows to measure wavelength dependent extinction profiles.

4.2.5 Scattering-Type Scanning Near-Field Microscopy[5]

Scattering-type scanning near-field optical microscopy (s-SNOM) is a microscopy technique that is based on atomic force microscopy (AFM), coupled with a laser. s-SNOM enables to measure the optical phase (absorption) and amplitude (reflectivity) of the tip scattered light simultaneously to the sample topography. In this thesis it was used to measure the absorption of encapsulated 6T molecules inside BNNTs.
The measurements were performed with a commercial *NeaSNOM* from *attocube* in pseudoheterodyne configuration for background subtraction, Fig. 4.12. As a probe we used platinum coated AFM tips from *Nano World* (*Arrow-NCPt*). As an excitation light source a wavelength-tuneable laser from *Hübner* (*C-Wave*) was used, covering the visible spectral range from 450 to 650 nm.

[5]Parts of this section were submitted as *Collective States of α-Sexithiophene Chains Inside Boron Nitride Nanotubes* in Juergensen et al. Nano Lett. (July, 2024).

The laser beam was guided through a beam expander onto a parabolic mirror (NA 0.4) that focuses the beam onto the AFM tip which acts as a near-field probe in the visible spectral range. The incoming laser light creates a strong localized electromagnetic near field at the tip apex. When the tip is in the proximity of the sample the near field interacts with the sample changing the tip-scattered field. The detected light is composed of near-field signal from sample and background signal.

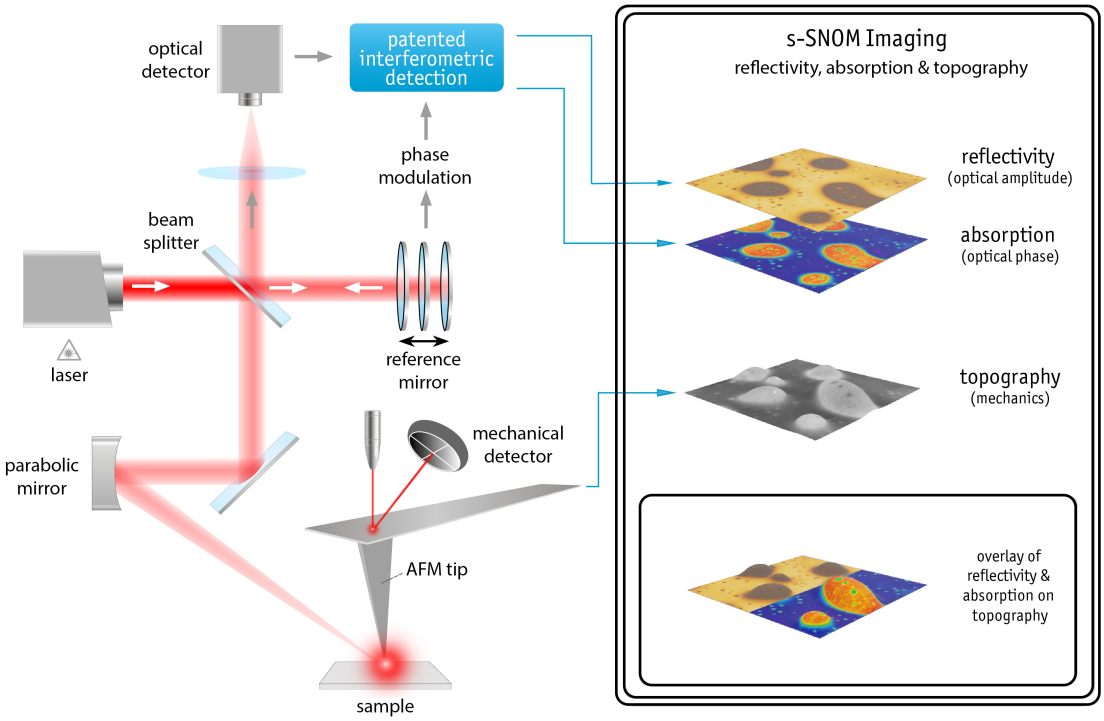

Figure 4.12 **Schematic of the s-SNOM.** The s-SNOM enables to measure the phase and amplitude of the tip-scattered light simultaneously to the sample topography. Adapted from Ref. [166].

To extract the near-field signal from the background signal the tip is oscillated at a certain characteristic frequency Ω (300 kHz). For further noise reduction a reference beam is send to a modified Michelson interferometer with oscillating mirror at frequency $M \ll \Omega$. The detected interfering beam is modulated at frequencies $f = n\Omega \pm mM$ leading to side bands next to the fundamental harmonic (nΩ). [165] Here n and m are integers expressing the order of the modulation. Demodulation suppresses the background signal and extracts the phase and the amplitude of the

elastically scattered light. Thereby, the phase is proportional to the absorption of the investigated material and the amplitude to the reflectivity. Calibration of the encapsulated 6T molecule (6T@BNNT) phase signal was done by an empty BNNT to account for wavelength-dependent changes in the sensitivity of the setup.

4.3 Numerical Approach: Finite-Difference Time-Domain[6]

The optical properties like reflectance, transmittance and absorbance as well as the electric near fields of plasmonic systems can be modeled by different numerical approaches that are based on a discretization of space and a solution of Maxwell's equations. One approach is the finite-difference time-domain (FDTD) method which uses the Yee algorithm. [167–169] The method solves Maxwell's equations by discretizing time and space using finite differences. This means that all spatial and temporal derivatives in Maxwell's curl equations are replaced by finite difference quotients. [170] The discretization of space is sketched in Fig. 4.13a,b. Not only the nanostructure is divided into little cubes (Yee cells) also the sub- and superstrate.

The electric (E) and magnetic (H) fields are separated on staggered grids building up the Yee cells, Fig. 4.13c. The calculation of both is done in a leapfrog manner. [168, 170, 172] This means that the electric field at time t is calculated from the electric and magnetic field of the last time step and *vice versa*, Fig. 4.13d. Thereby, an offset of 1/2 (with respect to the cubic mesh cell) exists in space and time between the grid points where the electric and magnetic fields are computed, Fig. 4.13c,d. [170]

One disadvantage of this method is that due to the discretization by the cubic mesh it is difficult to model curvatures which results in staircase artifacts. [173] Choosing the mesh suitably small improves the outcome but increases the memory requirements and calculation time. [174]

[6]Parts of this section were published as *Plasmonic Bimetallic Two-Dimensional Supercrystals for H_2 Generation* in Herran and Juergensen et al. Nature Catalysis **6**, 1205–1214, DOI: 10.1038/s41929-023-01053-9 (2023).

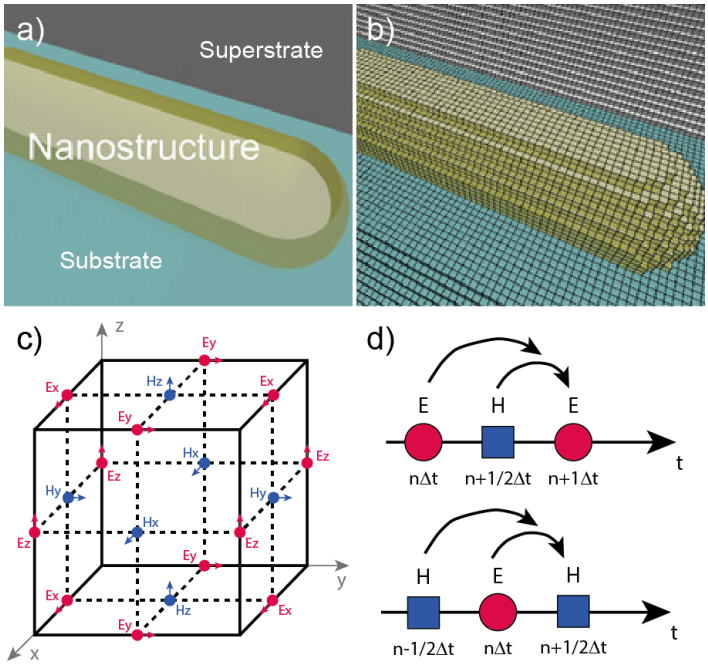

Figure 4.13 **Numerical Approach for the Calculation of the Optical Properties of Plasmonic Systems. a)** Sample structure: a gold nanorod on a substrate. **b)** Sample structure after applying a cubic mesh on it, which leads to staircasing. **c)** Sketch of a Yee cell demonstrating the field vector compounds. **d)** Sketch of the leapfrog manner calculation. Adapted from Refs. [170, 171]

For the simulations of the bimetallic supercrystals in this thesis *Lumerical FDTD Solutions*, a commercial software package, was used as described in Ref. [10,126,175]. The crystals were simulated by defining a unit cell and using periodic boundary conditions along x and y, and perfectly matched layers along z. Spherical gold nanoparticles with a diameter of 22 nm and interparticle gaps of 2 nm were packed into a hexagonal lattice. To simulate crystals with different layer numbers one to three layers were stacked in the *abc* sequence of an fcc crystal. The cell size of the mesh was set to 0.2 nm to accurately model the geometry of the supercrystal. By fitting the experimental data from Olmon et al. [176] the dielectric function of gold was determined. For the ligand molecules (polystyrene) a dielectric medium with refractive index $n = 1.4$ was assumed that fills the space between the gold particles. A broadband plane-wave source along the z-direction was used as excitation source. The reflectance (R) was recorded with a power monitor behind the source while the transmittance (T) was measured with a monitor behind the supercrystal. The absorbance (A) was subsequently calculated by $A = 1 - R - T$.

For the gold platinum crystal simulations 3 nm platinum particles were added in the gaps of the gold nanoparticles and the gap size was changed to 3.5 nm as determined from transmission electron microscopy images, *cf.* Fig. 7.1. The dielectric function of the platinum was determined by fitting the experimental data from Palik. [177] All the other parameters were kept the same.
To simulate unpolarized light every simulation was performed twice. Once with x- and once with y-polarized light. Subsequently, the mean value was taken to model the response to unpolarized light. For the simulations of the electric field enhancement the enhancement of the topmost layer for crystals of one, two and three layers were summed up and weighted by the relative surface coverage to simulate the case of the photocatalytic experiments.

5 | Collective States in Molecular Monolayers[1]

In this chapter, I will study collective states in two-dimensional (2D) molecular monolayers. The collective state emerges due to the Coulomb coupling of the transition dipole moments in the molecule film. First, I will theoretically show the optical behavior of a perfect dipole lattice and I will evaluate on a theoretical basis how strong energetic and spatial disorder as well as homogeneous broadening affect the optical response of the collective state. Subsequently, I investigate monolayers of the perylene derivate MePTCDI (see Sec. 2.2.7) evaporated by PVD (see Method Sec. 4.1.1) on hBN and few-layer graphene. With different florescence and absorption microscopy and spectroscopy techniques I measure the optical response of the MePTCDI monolayer and investigate the lattice structure. I compare the results with the simulations of the real lattice. In the end of the chapter, I will show that the lattice structure on graphene is the same as on hBN and prove that collective states can also exist on substrates that provide an additional radiative loss channel.

5.1 Theory of Collective Molecular Excitations

To model collective molecular states in 2D systems we consider a finite 2D arrangement of molecules that interact through their transition dipole moments. [65, 178,

[1]Parts of this chapter were published as *Collective States in Molecular Monolayers on 2D Materials* in Juergensen et al. ACS Nano **17**, 17350–17358, DOI: 10.1103/PhysRevB.107.235122 (2023). The project was conceived and planned by S. Reich and me. The microscopic model of collective dipoles was developed and the simulations done by N. S. Mueller. Sample preparation was done by M. Kessens and me. Fluorescence and absorption measurements were performed by M. Kessens and me. Resonant Raman spectroscopy was performed by C. Berrezueta-Palacios and me. Atomic force microscopy (AFM) was done by N. Severin, S. Ifland, and J. R. Rabe. I interpreted the data and wrote the manuscript. All authors commented on the manuscript.

179] We use a real space model, *cf.* Sec. 2.2.3 - developed by N. S. Mueller [11], for its ability to describe any arrangement of dipoles in space without imposing, *e.g.*, translational symmetry. Each molecular transition is represented by a point dipole $d = \alpha E_0$ induced by the field E_0 with the polarizability

$$\alpha = \frac{d_{ge}^2}{\hbar(\omega_0 - \omega - \mathrm{i}\gamma_0)}, \tag{5.1}$$

where ω is the driving frequency, ω_0 the molecular transition frequency, $2\gamma_0$ its spectral broadening, and d_{ge} the transition dipole moment. Each individual dipole interacts *via* its electric field with all other transition dipoles. The interaction changes the dipole moment at each lattice site and gives rise to collective dipolar eigenmodes $\mathbf{m}_p$ with polarizability α_p, see Sec. 2.2.3 for details. The individual polarizability α is replaced by the collective lattice polarizability [65]

$$\alpha_{\mathrm{coll}} = \sum_p \alpha_p = \sum_p \frac{d_{ge}^2}{\hbar(\omega_0 - \omega + \Delta_p) - i\hbar(\gamma_0 + \gamma_p)}. \tag{5.2}$$

The collective transitions are shifted in frequency by $\Delta_p = d_{\mathrm{ge}}^2 \mathrm{Re}(g_p)$ compared to ω_0, where g_p is the complex eigenvalue of the Green's tensor describing the near- and far-field dipole-dipole coupling, see Sec. 2.2.3. In addition, the decay constant is increased by $\gamma_p = d_{ge}^2 \mathrm{Im}(g_p)$, which is the characteristic increase in the emission rate, observed in molecular aggregates. The collective response of the molecular lattice can be measured experimentally by the extinction and compared to a calculated extinction coefficient that depends on the sum over α_p, see Sec. 2.2.3 for details. Figure 5.1 shows dipole chains (one-dimensional) of increasing length as calculated with the microscopic dipole model reproducing the well-known frequency shifts of pure J- and H-aggregates.

In Fig. 5.2a, we show the shift in energy of selected collective states in an $N \times N$ square lattice. The absolute magnitude of the shift depends on the collective eigenvector, the individual transition dipoles, the packing density, the lattice size and type, and the dielectric screening. The eigenenergies shift with N but for most modes saturate for 100 dipoles in the finite lattice ($N = 10$), Fig. 5.2a. The eigenmode with the strongest dipole moment, eigenvector I in Fig. 5.2b, has all dipoles oriented parallel resulting in a maximum shift of 200 meV or 10% of the transition frequency. The mode with the second strongest dipole moment

corresponds to an anti-bonding configuration with three stripes of dipoles that are aligned side-by-side (vector II). For very small lattices it results in a strong blue shift of the collective state, because of the purely repulsive nearest-neighbor interactions for $N = 2$ and 3. With increasing lattice size ($N \geq 4$), the dipole-dipole coupling along the x direction becomes partly attractive (parallel dipoles along x) and partly repulsive (antiparallel along x and parallel along y). The frequency shift of eigenvector II converges towards zero for larger N since all attractive and repulsive contributions cancel approximately.

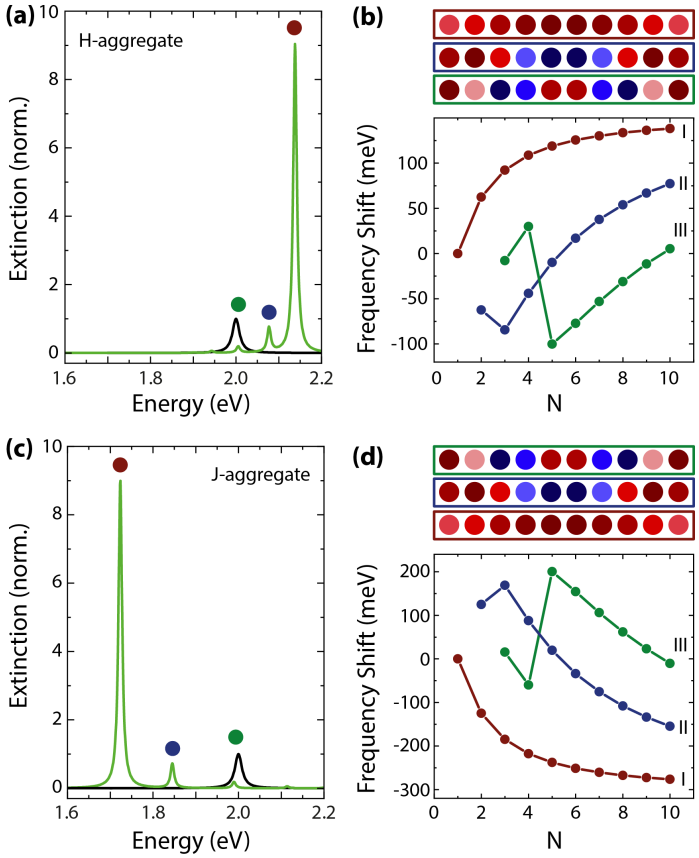

Figure 5.1 **Collective Extinction of a One-Dimensional (1D) Dipole Chain. (a,c)** Collective extinction of a 1D dipole chain with dipole orientation in y-direction (H-aggregate) and along x (J-aggregate) showing the typical blue/red shift, respectively. The colored dots indicate to which eigenmode in (b,d) the spectrum belongs to. The spectra are normalized to the extinction of a single dipole with $\omega_0 = 2\,\text{eV}$, $d_0 = 10\,\text{D}$ and $\gamma_0 = 5\,\text{meV}$. **(b,d)** Energy shifts of selected eigenstates with eigenvectors shown above. Eigenstate I (red curve) has the strongest dipole moment and is optical active. For the eigenvectors red and blue correspond to opposite orientations of transition dipoles.

Interestingly, eigenvector III with a corresponding pattern varying along the y axis has a red shift of $\sim 300\,\mathrm{meV}$, Fig. 5.2a, *i.e.*, higher than for the perfectly parallel dipoles in eigenvector I. When all dipoles oscillate in-phase along x the coupling is attractive for dipoles along the oscillation direction but repulsive perpendicular to it, Fig. 5.2c. Modes with anti-parallel stripes of dipoles perpendicular to the oscillation direction, therefore, have a stronger binding contribution and a larger frequency shift. The mode with the highest energy shift, eigenvector IV, has single lines with alternating polarization direction resulting in the configuration with the strongest bonding character along the lines and perpendicular to them. This means that for this 2D square lattice the excited state with the lowest energy is dipole forbidden and fluorescence needs to be activated thermally. [61]

Absorption and emission of the perfect 2D dipole lattice is dominated by a few bright modes, while the majority of the eigenvectors are dipole forbidden. [180] Eigenvector I has a dipole moment of 94 D, which increases its radiative decay γ_p by a factor of 88 compared to the individual dipole ($N = 10$). For mode II and III the increase amounts to a factor of five and two, respectively. The increase in the radiative decay by approximately $\Gamma_{\mathrm{rad}}(\omega) \propto N^2$ is known as the Dicke superradiance [181] that arises from the collective emission of many molecules. While the rate of spontaneous emission increases for specific modes in Fig. 5.2b, the overall integrated intensity remains the same for arrays of coupled and uncoupled dipoles. The absorption or extinction spectrum of the 2D lattice is governed by the total response of all collective eigenstates resulting in a single dominant peak at the energy of the collective mode with the strongest dipole moment, Fig. 5.2d. The integrated intensity of the extinction peak follows $\sigma_{\mathrm{ext}} \propto 0.9N^2$. This means that the extinction spectrum of a 2D lattice is of similar intensity for coupled and uncoupled transition dipoles, because individual dipole intensities have an overall extinction $\sigma_{\mathrm{ext}} \propto N^2$ through the sum of all uncoupled contributions. Nevertheless, the peak position is a clear fingerprint for a collective state.

The formation of the collective 2D state, its energetic position, and even the intensity of the extinction spectrum are surprisingly robust against spatial disorder and inhomogeneous broadening of the molecular transition as we show now with our real space simulations, Fig. 5.3. [179] We first consider spatial disorder that may arise from variations of the dipole positions so that the dipole monolayer deviates from the perfect 2D lattice. We model this by varying the dipole positions $\mathbf{r}_i + \delta\mathbf{r}_i$ in the xy plane around the sites $\mathbf{r}_i$ of the perfect lattice, where $\delta\mathbf{r}_i$ is obtained

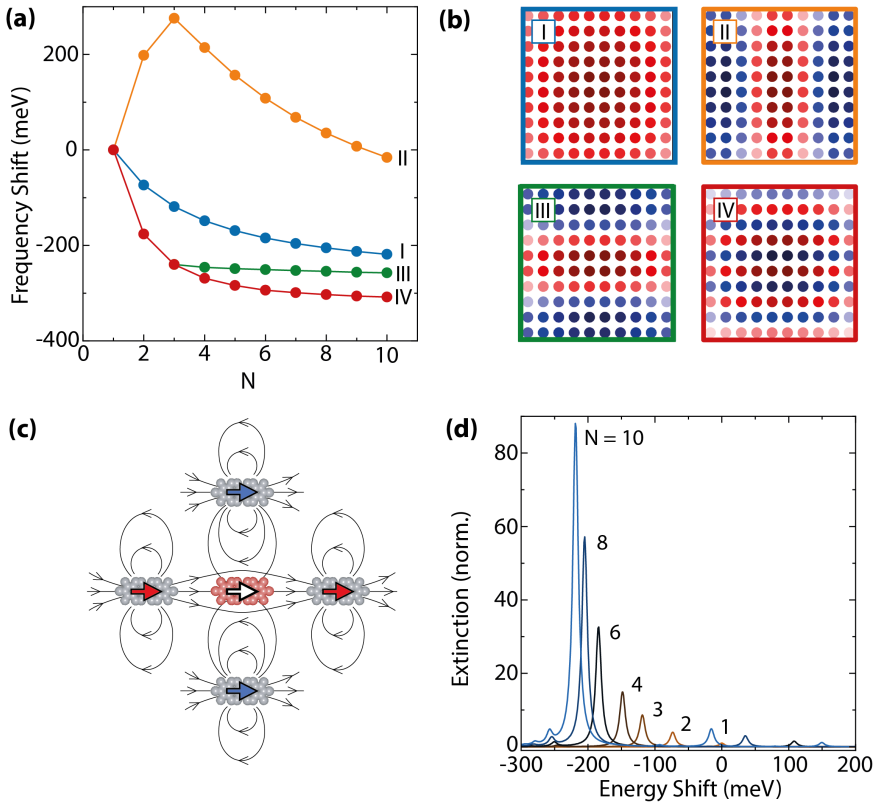

Figure 5.2 **Microscopic Model of Collective Excitons. (a)** Energy shift of selected eigenstates with eigenvectors shown in (b) for an $N \times N$ square lattice. Eigenstate I (blue) has the strongest dipole moment, eigenstate IV (red) is optically inactive, but has the largest energy shift. The labels connect the eigenenergies to the eigenvectors in (b). **(b)** Selected collective eigenmodes of a molecular 10×10 lattice in real space. Red (blue) dots indicate positive (negative) dipole moment along x. **(c)** Nearest-neighbor interactions of dipoles (bold arrows) through their electric fields (black lines). Two neighbors (red arrows) are in an attractive interaction with the centered dipole (white arrow), whereas the other two neighbors are in an anti-bonding configuration (blue arrows). **(d)** Collective extinction of an $N \times N$ square lattice of dipoles with increasing N (see labels). The spectra are normalized to the extinction of a single dipole with $\omega_0 = 2\,\text{eV}$, $d_0 = 10\,\text{D}$ and $\gamma_0 = 5\,\text{meV}$. Lattice constant $a = 1\,\text{nm}$, $\epsilon_m = 1$, and dipole polarization along x in all simulations.

through random sampling from a multivariate Gaussian distribution. To account for the large sample area that is typically probed in experiments we averaged the extinction spectrum over several random lattices, Fig. 5.3a. Disorder increases the width and decreases the maximum intensity of the extinction spectrum, but the peak area remains within 95% of the original intensity for a standard deviation

of $\sigma = 10\%$, inset in Fig. 5.3a. Collective states continue to form despite the spatial disorder, but the delocalized eigenvectors of the perfect lattice become more localized with disorder, right panels in Fig. 5.3a. The frequency shift of the collective excitation increases slightly in the disordered lattice, Fig. 5.3a, because the dipole-dipole interaction scales with $1/|\mathbf{r}_i - \mathbf{r}_j|^3$. [182] A (random) decrease in the dipole distance causes a larger red shift than the blue shift induced by the corresponding increase in dipole distance.

Another source of disorder is inhomogeneous broadening or fluctuations in the transition frequency from one dipole to the next. For most dye molecules the emission and absorption line widths under ambient conditions at room temperature ($\approx 10 - 100\,\mathrm{meV}$) are dominated by inhomogeneous broadening compared to the much smaller radiative decay constants ($\hbar\gamma_{\mathrm{rad}} \approx 10^{-8} - 10^{-6}\,\mathrm{eV}$). At first sight, this appears to be a more serious distortion for the formation of a collective state that depends on the Coulomb coupling of transition dipoles (or the absorption and emission of virtual photons). However, the collective state remains present despite random fluctuations in excitation frequencies, see Fig. 5.3b. While the dominant collective mode continues to be delocalized in the lattice, it is formed by a subset of dipoles, right panels in Fig. 5.3b. As for spatial disorder, inhomogeneous broadening has little effects on the integrated intensity (90% intensity for 4% disorder). Although the width of the collective extinction peak increases with the inhomogeneously broadened dipoles, its line width is smaller than expected from the variations in the individual peak positions, an effect that is known as exchange narrowing in molecular aggregates. [37] We fitted the spectra in Fig. 5.3b with a single Lorentzian and determined the inhomogeneous contribution to the FWHM. The inhomogeneous contribution in the 10×10 dipole lattice was only 30% of the inhomogeneous broadening for the individual dipoles, because the collective eigenvectors combine dipoles of similar frequency in the formation of the collective state, see right panels in Fig. 5.3b. For the inhomogeneously broadened dipole response, we modeled the eigenstates and the extinction spectra for 2D lattices in which the individual dipole frequencies vary randomly $\omega_0 + \delta\omega_i$; $\delta\omega_i$ is obtained through random sampling from a Gaussian distribution with standard deviation σ. As for spatial disorder we report an average over many simulation runs. Average spectra are calculated from 5, 10, 15, and 20 random lattices where the frequencies of individual dipoles vary by $\sigma = 1\%$, 2%, 3%, and 4% with respect to $\omega_0 = 2\,\mathrm{eV}$. Finally, we show the effect of an additional non-radiative decay channel or homoge-

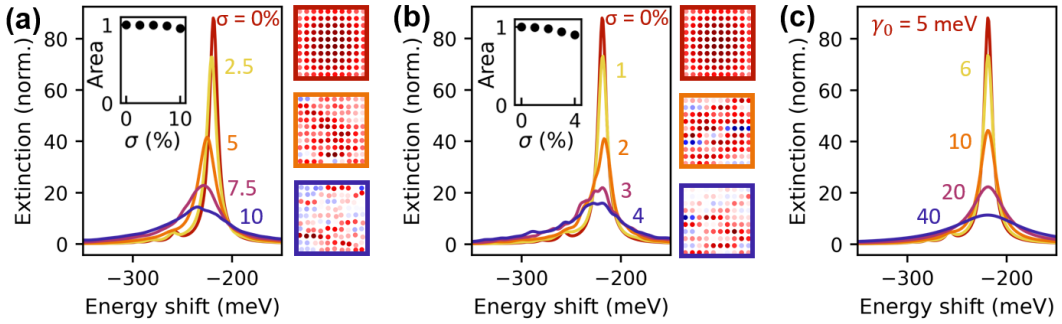

Figure 5.3 **Disorder in 2D Dipole Lattices. (a)** Effect of position disorder on collective extinction. Average spectra are calculated from 1000 random lattices with standard deviation σ (units of lattice constant) of each dipole position in the xy plane. The panels to the right show dominant collective modes of selected random lattices with $\sigma = 0\%$, 5%, and 10% from top to bottom. **(b)** Effect of frequency disorder on collective extinction of 10×10 square lattice. The panels to the right show dominant collective modes for selected random lattices with $\sigma = 0\%$, 2%, and 4% from top to bottom. Insets in (a) and (b) give integrated peak areas. **(c)** Collective extinction for perfect lattice with increasing homogeneous broadening γ_0. All spectra are referenced to the extinction of a single dipole with $d_0 = 10\,\mathrm{D}$ and $\gamma_0 = 5\,\mathrm{meV}$. Further parameters: lattice constant $a = 1\,\mathrm{nm}$, $\epsilon_m = 1$, and dipoles along x.

neous broadening by varying γ_0 in Fig. 5.3c. This additional contribution affects all individual dipoles in exactly the same way and leads to an increase in the FWHM of the collective eigenmodes. The cooperative frequency shift $\Delta_p = d_{\mathrm{ge}}^2 \mathrm{Re}(g_p)$, on the other hand, depends only on the transition dipole d_{ge} and the geometry of the lattice *via* $\mathrm{Re}(g_p)$. It is independent of γ_0 as confirmed by the constant peak position in Fig. 5.3c.

To summarize, we simulated a molecular monolayer by a square lattice of interacting transition dipoles in real space. The interaction between the molecules leads to collective eigenstates that give rise to a strong red shift of the predicted excitation frequencies. This process is robust against spatial and energetic disorder, because of the strong dipole-dipole coupling in the tightly packed molecular layers. We also find that an increase in non-radiative decay will not affect the collective frequency. For a perfect lattice the collective frequency depends only on the individual transition frequency, the strength of the transition dipole, the 2D lattice type, its lattice constant, and the screening by the environment. We now realize such 2D molecular lattices experimentally to study the collective states by optical spectroscopy.

5.2 Growth and Structure of MePTCDI Monolayers

Monolayers of MePTCDI were grown on multi-layers of hBN as an insulating and few-layer graphene as a conductive substrate. MePTCDI is a planar dye molecule that belongs to the perylene family with a conjugated π-system, see molecule structure in Sec. 2.2.7. It was previously shown to form micron-sized monolayers on atomically flat hBN. [3] We initially characterize the MePTCDI structure on hBN with fluorescence microscopy and high-eigenmode tapping mode atomic force microscopy (AFM). [183] Figure 5.4a shows a multi-layer hBN flake with MePTCDI molecules on top that were deposited by physical vapor deposition, see Method Sec. 4.1.1. The green luminescence is emitted from an MePTCDI monolayer that arranged non-covalently on the hBN substrate. [3] It has an emission maximum at 2.25 eV (551 nm) as we will discuss in detail in the next section. The monolayer areas dominate the sample in Fig. 5.4a and account for 84% of the hBN area. The red areas (16%) are molecular aggregates where the molecules stacked in three-dimensional structures and interact *via* $\pi - \pi$ coupling in addition to the Coulomb interaction. [3] The agglomerate fluorescence spectrum peaks at 1.75 eV (709 nm), Fig. 5.4b, resulting in the red appearance in the fluorescence microscope image, Fig. 5.4a.

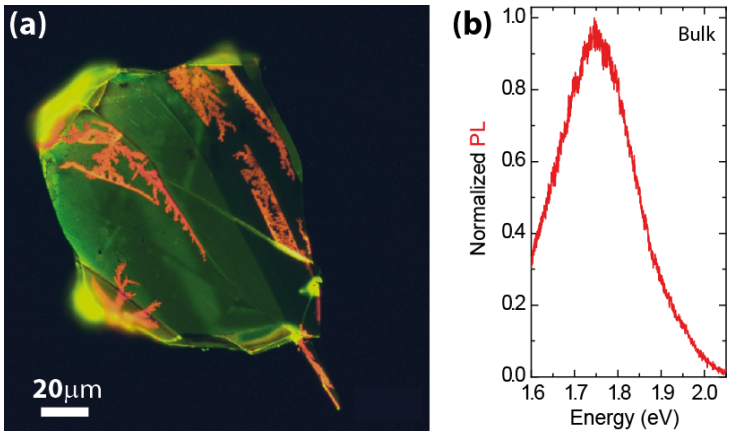

Figure 5.4 **Fluorescence Image and Spectrum of an hBN Flake with Ordered Molecules. (a)** Fluorescence microscopy image of an hBN flake with ordered MePTCDI molecules on top. The area with green luminescence belongs to highly ordered monolayers of MePTCDI, whereas red luminescence are molecular aggregates (bulk). **(b)** Micro-fluorescence spectrum of a MePTCDI bulk agglomerate in (a). The spectrum was measured by exciting the structure with a 532 nm laser.

In collaboration with N. Severin we measured the structure of the MePTCDI monolayers using high-resolution AFM, see Fig. 5.5a. The image shows an almost square lattice with lattice constants $a = b = (11.8 \pm 0.3)$ Å and an angle $\angle \mathbf{a}, \mathbf{b} = (84 \pm 2)°$ as determined from a fast Fourier transform (FFT) of the AFM image, see inset. Figure 5.5b sketches the obtained monolayer structure that corresponds to the so-called brick stone lattice. [184] It results from the orientation of the transient molecular dipole moments plus the repulsion of the positively charged oxygen atoms. Dipole-dipole coupling aligns the molecules in a line along their long axis. The next row of molecules is placed in parallel but shifted for maximum distance between the oxygen atoms on neighboring MePTCDI molecules. Multi-layers of MePTCDI form a herringbone structure, [3] but the brick stone lattice in Fig. 5.5 has denser packing and is, therefore, favored in the monolayer.

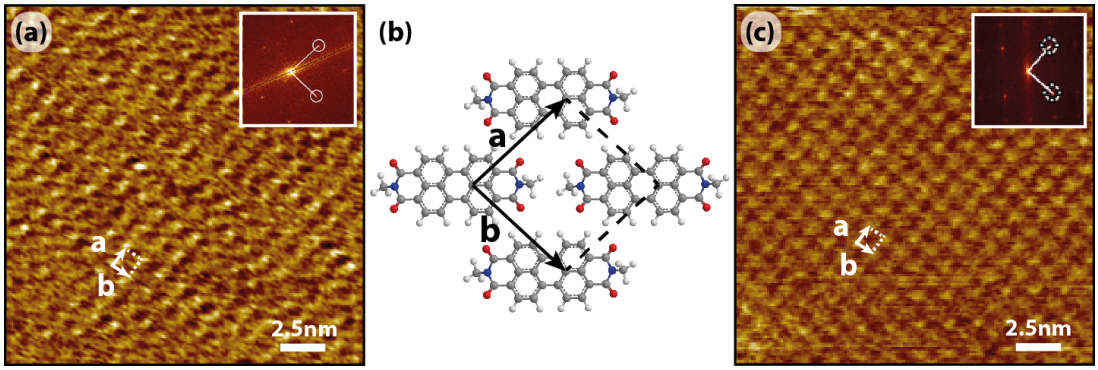

Figure 5.5 **Structure of the MePTCDI Monolayer on Multi-Layers of hBN and Few-Layer Graphene.** High resolution AFM phase images of the grown molecular layer on multi-layer **(a)** hBN and **(c)** graphene. Both images show a periodic nearly square pattern. The insets are FFT patterns of the phase images in (a) and (c), confirming the periodicity of the monolayers. **(b)** Brick stone lattice structure of the organic MePTCDI layer with the unit cell shown by black lines ($a = b = 11.8$ Å, $\angle \mathbf{a}, \mathbf{b} = (84 \pm 2)°$) agreeing within the experimental uncertainty of the unit cell from AFM imaging. The gray spheres of the molecule structure are carbon, red oxygen, blue nitrogen, and white hydrogen atoms.

The MePTCDI monolayer structure on multi-layer graphene, Fig. 5.5c, is identical within the experimental error to the one on hBN, Fig. 5.5a. The substrate had no direct effect on the in-plane structure of the molecular monolayer, which is reasonable because of the similar interaction and coupling strength of aromatic molecules to graphene and hBN. [185] The structure of the MePTCDI monolayer is determined by intermolecular interactions *via* Coulomb coupling and oxygen

repulsion; the two-dimensional crystals only ensure the flat arrangement. Due to their structural similarity, the two MePTCDI monolayers are excellent candidates to study how the interaction with the substrates affects the molecular transitions and the formation of collective states.

5.3 Collective MePTCDI Exciton

Light absorption and emission from the MePTCDI monolayer at room temperature, Fig. 5.6, has a strong peak at 2.25 eV, which originates from collective molecular states. It is shifted by 60 meV to smaller energies compared to the monomer (2.31 eV), Fig. 5.6a. This is in good agreement with Zhao *et al.*. [3] The emission is polarized, inset in Fig. 5.6a, which confirms optically that the molecules form a highly orientated lattice. In addition to the red shift of the emission, we find a vanishing Stokes shift in the monolayer absorption and emission, Fig. 5.6b. The Stokes shift of MePTCDI is already quite small in solution (60 meV), but the lower flanks of the absorption and emission peak are identical in the monolayer. [186] Other signatures of the collective state are the increase in the dominant zero-phonon-line compared to the phonon sideband and the much narrower line width of the monolayer emission compared to the molecules in solution, Table 5.1. [50, 70]

We calculated the expected frequency shift for a 2D lattice of MePTCDI monomers with $\hbar\omega_0 = 2.31\,\mathrm{eV}$, $\hbar\gamma_0 = 5\,\mathrm{meV}$, $d_{ge} = 8.8\,\mathrm{D}$, and $\epsilon_m = 2.7$, Fig. 5.6c,d. The used transition dipole moment d_{ge} was calculated by using Eq. (2.2) and (2.8). Therefor, the frequency depended absorption coefficient $\epsilon(\nu)$ in Fig. 5.7a was determined by the absorption of the MePTCDI molecules dissolved in chloroform. The dielectric background constant ϵ_m was calculated by averaging the dielectric contribution by air on top ($\epsilon_m = 1$) and by a half space filled with the van der Waals material underneath the MePTCDI layer, Fig. 5.7b, to account for the dielectric screening by the hBN substrate. With a direction-averaged dielectric constant of $\epsilon_{\mathrm{hBN}} = 4.3$ we obtain a background dielectric constant $\epsilon_m = 2.7$ for hBN. [187] This approach is an upper bound for the screening by the environment. A smaller screening would increase the predicted frequency shift due to the formation of the collective state. The dipoles were oriented at 45° in a square lattice as dictated by the brick stone structure (lattice constant $a = b = 1.2\,\mathrm{nm}$) in our experiments, Fig. 5.5b.
In this modeled lattice the eigenmode with the largest frequency shift (eigenvector I)

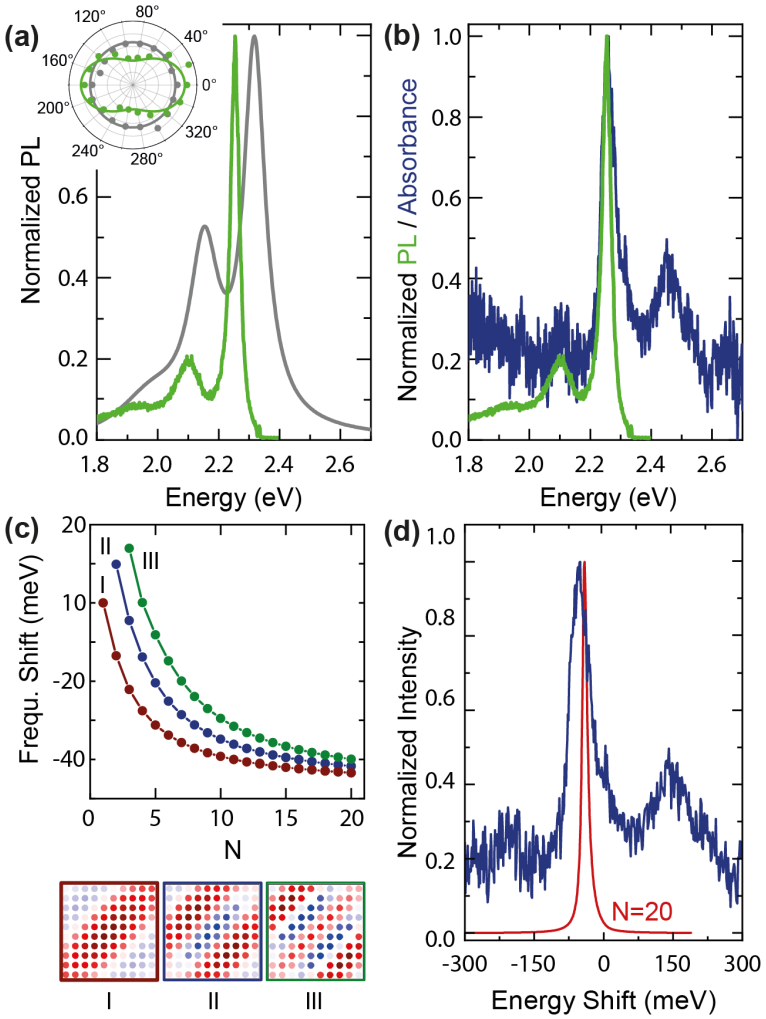

Figure 5.6 **Fluorescence and Absorption of the MePTCDI Monolayer.** **(a)** Fluorescence spectra of an MePTCDI monolayer (green) and MePTCDI in dimethyl sulfoxide (gray). For better comparison the emission and absorption spectra were normalized to one. The inset shows the polarization dependence of the light emission using the same color coding. **(b)** Comparison of the micro-fluorescence (green) and micro-absorption (blue) spectrum of the MePTCDI monolayer. Showing only a very small Stokes shift. **(c)** Frequency shift of collective eigenstates of an $N \times N$ brick stone lattice on hBN. Eigenstate I (red) has the largest net dipole, eigenstate II (blue) the second largest, and eigenstate III (green) the third largest. The panels below show the collective modes of the eigenstates in (c) for $N = 10$. Red (blue) dots indicate positive (negative) dipole moment along the diagonal. **(d)** Comparison of the micro-absorption (blue) spectrum and the simulated spectrum (red) of a 20×20 brick stone lattice.

has also the largest dipole moment, Fig. 5.6c. The luminescence by the MePTCDI lattice is therefore not thermally activated and remains present at low temperature which is in good agreement with prior experiments. [3] As the calculated frequency shift we obtain a red shift of 40 meV for the collective MePTCDI state, which is smaller than the experimental shift (60 meV), Fig. 5.6c,d. However, the simulation has a number of uncertainties: First, the molecules are large compared to their distance, which means that the point-dipole approximation is not strictly valid for this configuration. Second, $\hbar\omega_0$ was measured in solution and might actually differ on a solid substrate. Also, we assumed the screening by the hBN substrate to yield an effective background dielectric constant of $n = 1.64$, which corresponds to half space filling by the substrate and may overestimate the screening within the layer, see Fig. 5.7b.

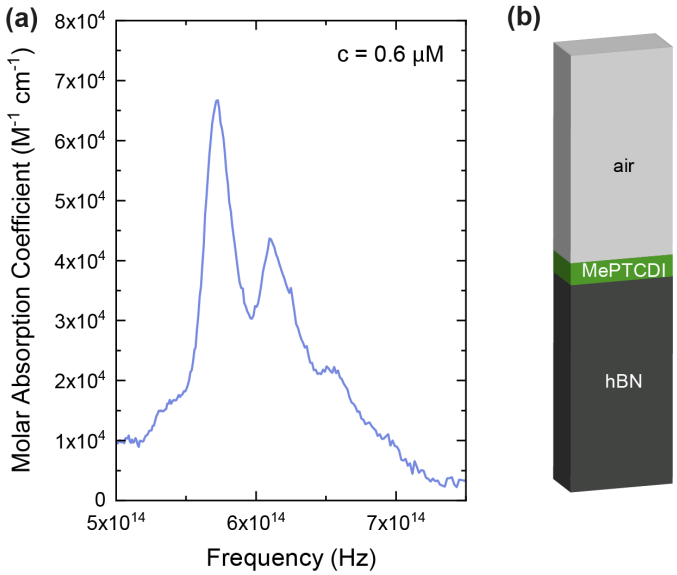

Figure 5.7 **Calculation of the Transition Dipole Moment and Estimation of the Dielectric Screening. a)** Molar Absorption Coefficient of MePTCDI Dissolved in Chloroform. The molar absorption coefficient was calculated from the absorption spectrum. The concentration of the solution was 0.6 μM and the path length 1 cm. **b)** Estimation of the Dielectric Screening. Sketch of the used averaging approach. The layers of hBN and air are weighted equally. Giving an effective background dielectric constant of $n = \sqrt{\epsilon_m} = 1.64$.

The emission spectrum of the MePTCDI monolayer has a narrow line width (FWHM = 36 meV) with a slightly larger width (45 meV) in absorption. The absorption is broader because all states with finite dipole moment contribute to

excitation, but light emission occurs predominantly from the lowest-lying optically active states. Despite its narrow appearance, the line width of the collective MePTCDI state remains dominated by inhomogeneous broadening with little contribution from spatial disorder. The FWHM of the monolayer amounts to 40% of the molecular transition in solution, Table 5.1, in reasonable agreement with the predicted narrowing (30%, Fig. 5.3b). The dominance of inhomogeneous broadening is also confirmed by time-resolved measurements that reported a lifetime of 30 ps and nearly 100% quantum yield for the monolayer, [3] which yields a lifetime limited FWHM $\approx 30\,\mu$eV, *i.e.*, three orders of magnitude below the observed width.

Table 5.1 **Transition Energies and Line Width of the Individual and Collective MePTCDI Excitons.**

Sample	ω (eV)	FWHM (meV)
MePTCDI monomer	2.31	90
MePTCDI/hBN absorption	2.25	45
MePTCDI/hBN emission	2.25	36
MePTCDI/graphene absorption	2.26	96
MePTCDI/graphene Raman resonance	2.26	140

On graphene the characteristic MePTCDI monolayer emission vanishes. Instead we observe the Raman spectrum of the monolayer, Fig. 5.8a. The peaks at 1309 cm^{-1} and 1392 cm^{-1} correspond to ring stretching modes of the perylene core while the mode at 1588 cm^{-1} belongs to C=C stretching of the carbon rings. [188] We attribute the quenching of the luminescence to a Förster resonant energy transfer that is very efficient, because of the small distance (0.3 nm) between a planar dye and graphene, the parallel alignment of the transition dipoles, and the broadband absorption of multi-layer graphene in the visible and near infrared. Experimentally, the intensity loss is at least five orders of magnitude or $\gamma_0/\gamma_{m\to G} \approx 10^{-5}$, where $\gamma_{m\to G}$ is the rate of excitation transfer from the molecule into graphene and γ_0 the intrinsic molecular decay rate.

To verify that the collective state of MePTCDI exists in the presence of graphene as a strong quenching agent, we measure the excitonic transition by absorption and resonant Raman scattering, Fig. 5.8b,c. The MePTCDI absorption on graphene has a main peak at the same energy as on hBN but twice its line width, see Table 5.1 and Fig. 5.8b. The small shift in the collective frequency between hBN and graphene is explained by the difference in the screening strength. The increase in FWHM

implies an additional broadening by a non-radiative channel with $\gamma_{nr} \approx 42\,\text{meV}$. Assuming $\gamma_{nr} = \gamma_{m\to G}$ and a lifetime of the MePTCDI transition on the order of 1 ns (Refs. [3, 189]) we estimate a relative transfer $\gamma_0/\gamma_{m\to G} \approx 10^{-5}$, which agrees with the intensity loss of the MePTCDI monolayer on graphene.

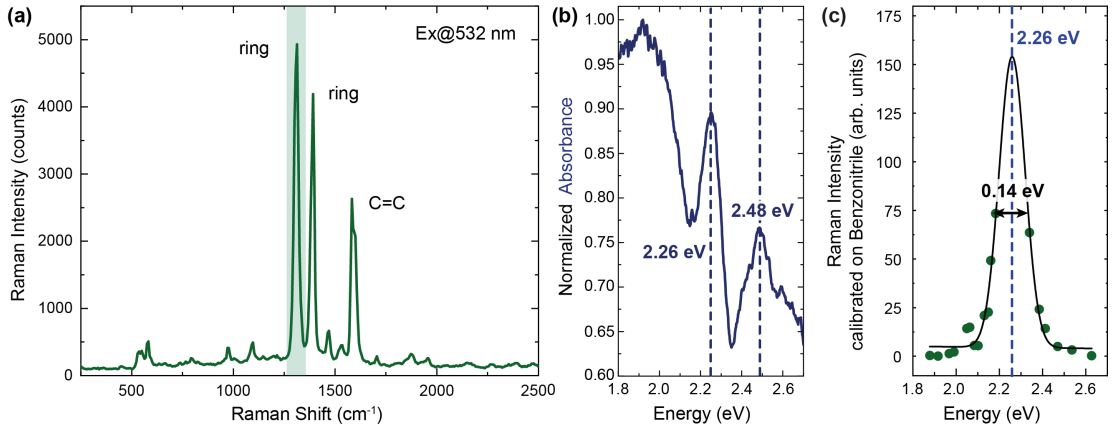

Figure 5.8 **MePTCDI Monolayer on Graphene.** (a) Raman spectrum of the MePTCDI monolayer on graphene at 532 nm excitation wavelength. The Raman modes of the dye molecule are indicated. (b) Normalized micro-absorbance spectrum of the MePTCDI monolayer on graphene. The spectrum has two absorption peaks that are located at 2.26 eV and 2.48 eV. (c) Resonant Raman profile of the ring stretching mode at $1309\,\text{cm}^{-1}$. The molecular resonance is located at 2.26 eV (549 nm) and has a FWHM of 0.14 eV.

In resonant Raman scattering we determined the integrated intensity of the ring stretch mode at $1309\,\text{cm}^{-1}$ as a function of excitation energy, Fig. 5.8c. The profile has a maximum at 2.26 eV with a FWHM of 140 meV that corresponds to the incoming resonance with the collective MePTCDI state. We did not observe an outgoing resonance in the profile that is expected at the incoming resonance plus the phonon frequency. [190, 191] Nevertheless, the Raman resonance clearly demonstrates that the collective dipole state exists for MePTCDI on graphene, although its emission is suppressed. Independent of the dielectric environment and excitation transfer, the molecular monolayer forms a collective state on flat surfaces. This remains true although in our system the broadening exceeds the coupling-induced red shift of the molecular excitonic transition of the MePTCDI monolayer.

5.4 Summary

In conclusion, we studied the transition of a localized excitation in a molecular monomer to a delocalized collective state in a molecular monolayer considering homogeneous and inhomogeneous broadening and spatial disorder. We presented a model based on the point-dipole approximation to calculate the eigenstates of 2D lattices and their extinction spectra. The interaction between the transition dipoles leads to collective states in the lattice and a red-shifted extinction spectrum. The shift depends on the radiative lifetime of the monomer (or the transition dipole) and the packing density of the molecular lattice. We found that spatial and energetic disorder as well as homogeneous non-radiative broadening lead to an increase in the line width of the collective state but hardly affect its transition frequency. Due to the strong dipole interaction and the small distance of molecules in a typical 2D lattice, the collective state is very robust. To study the predicted behavior experimentally, we grew monolayers of MePTCDI on multi-layer hBN and few-layer graphene substrates. We observed a brick stone lattice in the monolayer on 2D materials with a single molecule in the 2D unit cell. The collective monolayer state was shifted by 60 meV compared to the monomer transition which occurred on both hBN and graphene. On hBN we observed strong luminescence with characteristic signatures of superradiance like a narrowing of the transition and a vanishing Stokes shift. On graphene, the energy transfer from the MePTCDI molecules to the substrate led to an additional homogeneous broadening of 85 meV, but the collective state remained at the same energy. Our study shows that collective states in 2D molecular lattices are robust against disorder that result in additional homogeneous and inhomogeneous broadening. This could be applied for superradiant devices using soft materials with scalable fabrication techniques and solution-based processing.

6 | Collective States of α-Sexithiophene Chains inside Boron Nitride Nanotubes[1]

In this chapter of my thesis, I study collective states of α-sexithiophene (6T) chains inside boron nitride nanotubes (BNNTs). The nanotubes serve as a container to align the molecules into chains, forming J-aggregates. Depending on the inner diameter of the tubes several molecule chains can fit into a single tube resulting in an additional H-aggregate compound. [91] First, I will pre-characterize the tube bundle with encapsulated 6T molecules by different optical microscopic and spectroscopic methods. I will show that the investigated tube bundle shows a superposition of single- and multi-file chains. On the basis of the Stokes shift I show that also multi-file chains show a stronger J- than H-type of Coulomb coupling. At the end, I will compare my results on 6T molecules in BNNTs with 6T filled carbon nanotubes.

6.1 Sample Characterization

The BNNTs with encapsulated dye (6T@BNNT) were deposited onto a Si/SiO_2 wafer by spin coating. Encapsulation and deposition are described in the Method Sec. 4.1.2. The obtained sample was characterized by combined AFM and spatial

[1]Parts of this chapter were submitted as *Collective States of α-Sexithiophene Chains Inside Boron Nitride Nanotubes* in Nano Lett. (July, 2024) The project was conceived and planned by S. Reich and me. Sample preparation was done by J.-B. Marceau and E. Gaufrès. AFM, spatial modulation spectroscopy and micro fluorescence measurements were performed by me. s-SNOM was performed by P. Kusch and me. Photoluminescence excitation spectroscopy was measured by A. Setaro and C. Mueller. The theory was discussed with E. Barros. I interpreted the data and wrote the manuscript. All authors commented on the manuscript.

fluorescence spectroscopy, as well as polarization-dependent spatial modulation spectroscopy. Fluorescence microscopy was combined with AFM to distinguish between filled and empty BNNTs as well as between filled tubes and molecular agglomerates. A spatial fluorescence map of a $16 \times 16\,\mu m$ sample area was recorded, Fig. 6.1a, using 2.33 eV (532 nm) laser excitation, which is close to the molecular resonance. [47] It maps the intensity of the strongest fluorescence peak of 6T over the coordinates of the scanned sample area, showing areas of strong fluorescence (red areas) that may originate from filled tubes or free molecular agglomerates on the substrate. To distinguish between agglomerates and filled BNNTs we combine the fluorescence map with an AFM image of the same sample area, see Fig. 6.1b. Laying the fluorescence map on top of the AFM image, Fig. 6.1c, shows that the majority of the fluorescent spots indeed come from filled BNNTs. We identified a strongly emitting 6T@BNNT - likely a bundle of filled tubes - which is marked by a rectangle in Fig. 6.1c. The following measurements were performed on this 6T@BNNT unless noted otherwise. There are also empty tubes without molecules that do not show up in the fluorescence map, but are present in the AFM image.

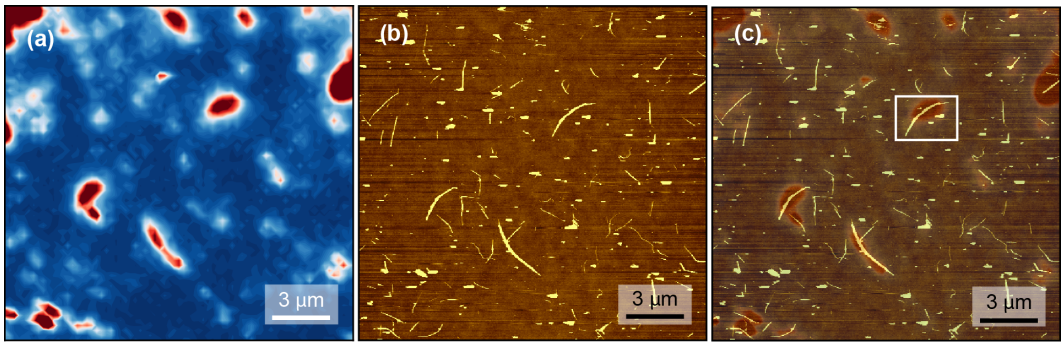

Figure 6.1 **Fluorescence Spectroscopy and Atomic Force Microscopy of 6T@BNNT. (a)** Spatial fluorescence map of 6T@BNNT on Si/SiO_2. Showing the fluorescence of the main transition (2.10-2.14 eV) of the 6T molecules. Red areas show the highest intensity. **(b)** AFM topography image of the sample area in panel (a). **(c)** Fluorescence map on top of the AFM image to identify tubes are filled with 6T. The white rectangle marks the tube bundle that was studied in the following.

To analyze molecular alignment in the filled BNNTs we measured the extinction of 6T@BNNT, *i.e.*, the sum of absorption and scattering, using polarized spatial modulation spectroscopy (SMS). A sketch of the SMS setup is depicted in the experimental Method Sec. 4.2.4. The sample holder contains a piezo element that

is mounted to modulate the sample position with frequency f while the sample is scanned through the focus of a laser beam. The demodulation of the scattered signal with a lock-in amplifier at frequency f leads to a contour plot with the shape of the first derivative of a Gaussian profile, from which we determine the extinction cross section of the tube bundle. [192–194]

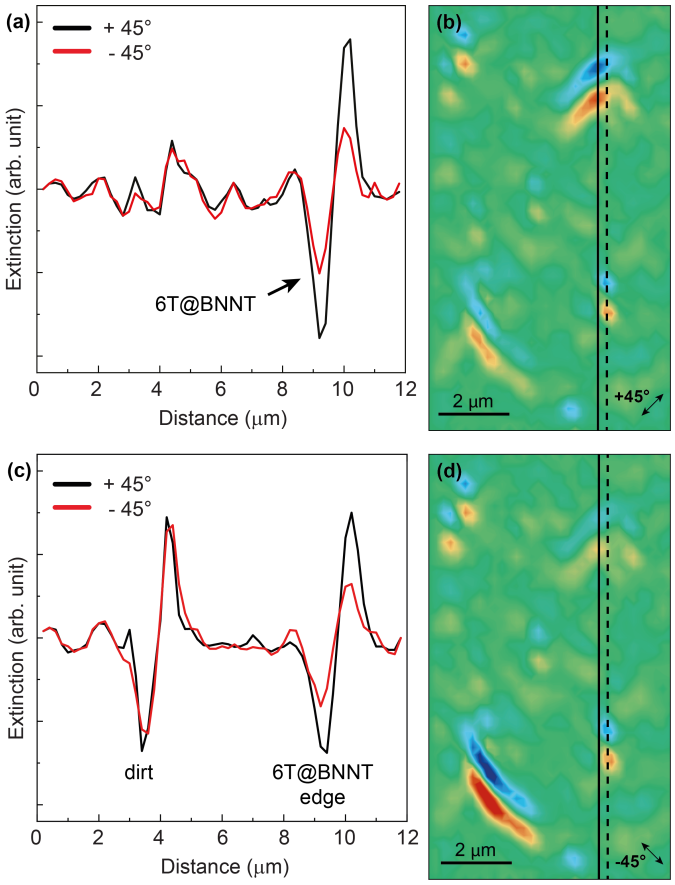

Figure 6.2 **Polarization Dependent Spatial Modulation Spectroscopy.** **(a,c)** Polarization-dependent extinction line profiles of the in (b) and (d) marked tube/dirt taken at 530 nm excitation wavelength. Black profile +45° and red profile -45° polarized light. Extinction contour plots of the studied area for **(b)** +45° and **(d)** -45° polarized light. Showing the polarization dependence of the filled tube bundles in the upper right and lower left corner. The solid black lines indicate the line profiles shown in (a). The dashed lines indicate the position of the line profile in (c).

We first recorded polarization-dependent SMS using 2.34 eV (530 nm) laser excitation, Fig. 6.2. It highlights the polarization dependence of the tube bundle. When the light is polarized along the BNNT axis the extinction is maximized

(black line profile in Fig. 6.2a and map in b) and when the polarization is (almost) orthogonal to the tube it is minimal (red line profile in Fig. 6.2a and map in d). Other objects like dirt and non ordered molecular agglomerates do not show any polarization dependence, Fig. 6.2c. This agrees with the prior observations of the polarization dependence of 6T molecules inside BNNTs [159] and shows that the 6T molecules are aligned along the tube axis. Further, the polarization-dependent SMS measurements allowed us to identify molecular agglomerates outside BNNTS, Fig. 6.1a. From the 6T@BNNT characterization we therefore identified 6T@BNNTs, unfilled BNNTs, and 6T agglomerates as well as dirt outside of BNNTs.

6.2 Results

A 6T@BNNT fluorescence spectrum is plotted in Fig. 6.3a together with the monomer spectrum of 6T measured in solution. In the monomer, the two main peaks were assigned to the 0-0 (2.44 eV) zero-phonon line and its 0-1 (2.29 eV) phonon replica with an energy separation of 0.15 eV [195–197]. The emission of the 6T@BNNT is strongly shifted to smaller energies as it is typical for the formation of molecular aggregates. [62, 72] In addition, the energetic separation of the two main peaks increased for the encapsulated molecules compared to the monomer, Fig. 6.3a and Table 6.1, and the intensity ratio changed.
To study the absorption of the 6T@BNNTs we performed wavelength-dependent SMS on the same sample area, giving us the extinction profile of the 6T@BNNT bundle in Fig. 6.3b. It is noticeable that the extinction is not the mirror image of the emission spectra in Fig. 6.3a, as is typical for molecules due to the similar emission/absorption probabilities in the ground (S_0) and first excited electronic state (S_1). [25, 27] The energetic separation of the two main peaks in the extinction spectrum ($\Delta\omega = 0.13$ eV) differs from the 6T@BNNT and monomer fluorescence spectra in Fig. 6.3a, see also Table 6.1.
The apparent discrepancies in emission and extinction spectrum of the 6T@BNNT arise from tubes filled with different numbers of parallel molecular chains resulting in a superposition of their optical responses. [159] The fluorescence spectrum in Fig. 6.3c is fitted well by four Lorentzians that we interpret as two pairs of peaks (red and blue lines). We assign them to the zero-phonon line and the phonon replica of the collective molecular states in single- and multi-file chains. Up to three chains may lie next to each other in ordered aggregates in a tube leading

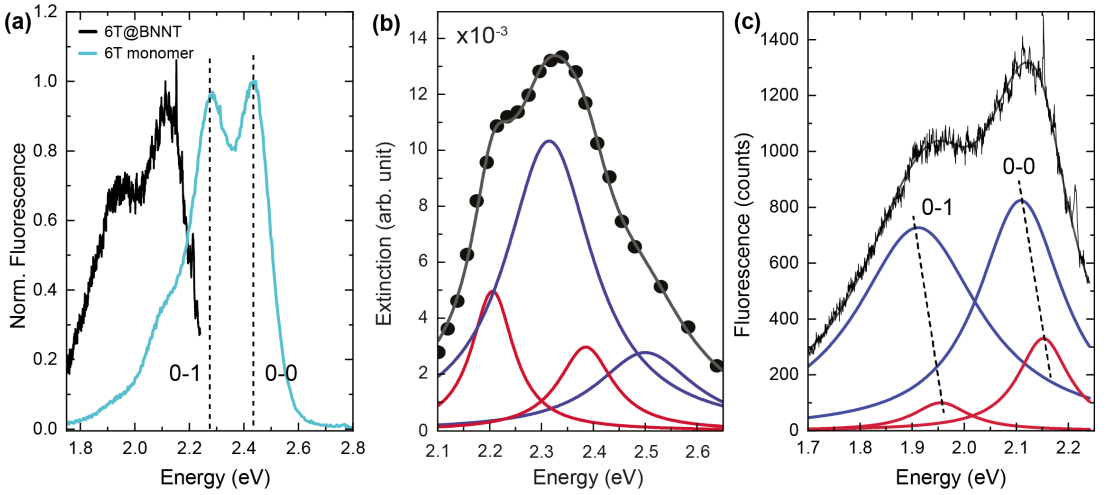

Figure 6.3 **Fluorescence Spectra and Wavelength-Dependent Spatial Modulation Spectroscopy. (a)** The fluorescence spectrum of 6T@BNNT (black) and 6T monomer (light blue) show a frequency shift, indicating the formation of ordered molecular aggregates inside the tube. **(b)** Wavelength-dependent extinction profile of the 6T@BNNT bundle and **(c)** fluorescence spectrum of 6T@BNNT (black) both fitted by four Lorentzian fits (red and blue solid lines). Dots are measurements and solid lines are Lorentzian fits.

to a head-to-tail configuration of the transition dipoles along the tube axis and a side-by-side configuration perpendicular to the axis. [159] For tubes with an inner diameter of more than 2.5 nm the molecules start to form undefined aggregates in the tube leading to an optical response that was not observed in the spectra presented here. [198] The fitting of the extinction curve with four Lorentzians, see Fig. 6.3b, results in two extinction spectra (red and blue) that are the expected mirror images of their respective 6T@BNNT emission, Fig. 6.3c. The energy difference of the two transitions fits to the C=C stretching vibration ($\sim$0.18 eV), see Table 6.1. [195, 199, 200] Despite the similar appearance, the double peak structure of the emission and extinction spectra have different origin: The two peaks in the extinction spectrum originate from the 0-0 transitions of the single- and multi-file chains, while the fluorescence is dominated by the 0-0 and 0-1 multi-file emission.

We used scattering scanning near-field optical microscopy (s-SNOM) to study the 6T@BNNT absorbance and its distribution along the nanotube axis with a resolution of $\sim$20 nm. s-SNOM determines the local absorbance of nanomaterials from its phase images, see Method Sec. 4.2.5, [201–203] and allows to study various

Table 6.1 **Transition Energies and Line Width of the Individual and Collective 6T Excitons.**

	S_{0-0}		S_{0-1}	
	ω (eV)	FWHM (eV)	ω (eV)	FWHM (eV)
monomer				
emission	2.44	0.14	2.29	0.15
single-file				
emission	2.15	0.12	1.96	0.13
extinction	2.21	0.10	2.39	0.13
absorption	2.16	0.14	2.25 - 2.40	-
multi-file				
emission	2.11	0.20	1.91	0.29
extinction	2.31	0.21	2.50	0.23

parts and hotspots along the 6T@BNNT bundle. Using a wavelength tuneable laser we measure phase images of the same 6T@BNNT bundle as a function of energy. An exemplary phase image recorded at 2.25 eV (550 nm) excitation is shown in Fig. 6.4a. The red areas indicate higher absorption than the white and blue areas. Figure 6.4b,c show the calibrated phase signal (absorbance) over 1.9 - 2.7 eV excitation energy at four different positions along the tube, arrows in Fig. 6.4a.

All four positions (I-IV) have an absorption peak at 2.16 eV. Positions I and II may show a second absorption maximum between 2.25 - 2.40 eV, but an energy gap in the tunable laser prevents measurements in this range. We identify the absorption peak at 2.16 eV in Fig. 6.4b,c with the single-file transition at 2.21 eV in the extinction spectrum. The lowest transition of the extinction profile is therefore by 50 meV higher than the peak in the absorption spectrum measured with the s-SNOM, see Table 6.1. This shift may be due to a strong scattering contribution to the extinction data and/or the characteristic shift between optical near- and far-field measurements. [191, 204, 205] We also note that the near-field absorption energy is identical to the far-field emission, which would point towards a vanishing Stokes shift for the single-file. The variation of the absorbance along the tube bundle indicated the tubes may be only partially filled or that the tube bundle gets thinner towards its end, since the s-SNOM signal is proportional the the amount of material. This also agrees with the observation that spots III and IV appear to have no absorption associated with the multi-file chains.

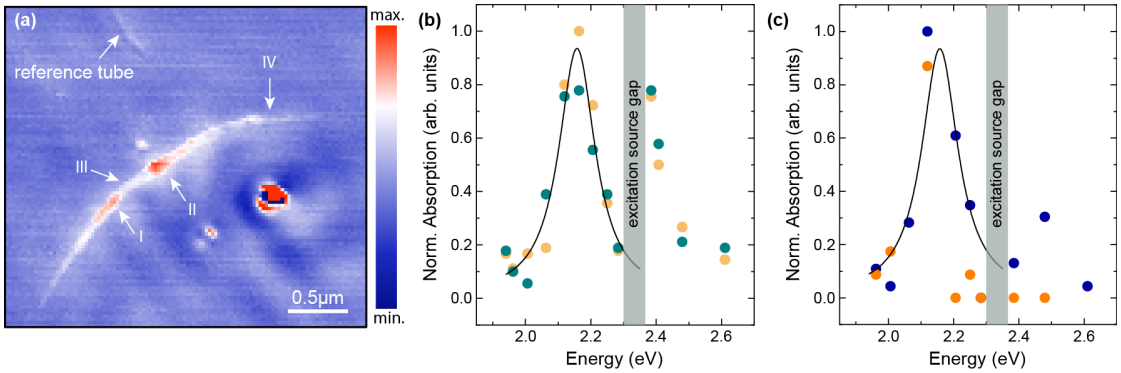

Figure 6.4 **s-SNOM Measurements of the 6T@BNNT Bundle. (a)** s-SNOM phase image of a 6T@BNNT hybrid. The red areas indicate a higher absorption than the white and blue areas. **(b)** s-SNOM measurements that belong to two parts of the BNNT bundle in (a) with higher absorption. The yellow data set belongs to the tube position (I) and petrol blue data set to position (II). The solid line is the Lorentzian fit of the absorbance. **(c)** The dark blue (III) and orange (IV) data set belong to two parts of the BNNT bundle in (a) that absorb less. For better comparison the absorption spectra are normalized to unity in panels (b) and (c).

6.3 Discussion

The fluorescence and absorption spectrum of the 6T@BNNTs reveal a rich combination of excited collective states as pictured in the Jablonski diagram in Fig. 6.5a, see also Table 6.1. The diagram compares the energy of the first excited state of the 6T monomer, Fig. 6.5b, with the collective states in 6T@BNNT single- and multi-file chains. The red shift of the collective state in the single 6T chain comes from the pure head-to-tail character along the chain, leading to a collective lowest excited states with an allowed dipole transition. The fluorescence of the single chain is also red shifted as is typical for J-aggregates. [50, 206] The remaining Stokes shift of 60 meV is vanishingly small compared to the $\sim$440 meV shift of the monomer, which indicates a pure head-to-tail configuration as well.

The collective energies of the 6T in a BNNT excellently agrees with previous measurements of 6T transitions in carbon nanotubes performed by resonant Raman scattering. [47] The close similarity of the in carbon and boron nitride encapsulated 6T chains implies that the packing of the 6T is similar in the two types of nanotubes and governed by the geometry of the available space. The difference in dielectric environment of carbon versus boron nitrite nanotube plays a negligible role for the energetic position of the molecular aggregates, which is rather surprising but

agrees well with the identical transition energies of ordered dye monolayers on two-dimensional hBN and graphene. [11] It is also confirmed by the weak dielectric screening by semiconducting nanotubes measured in double-walled nanotubes. [207]

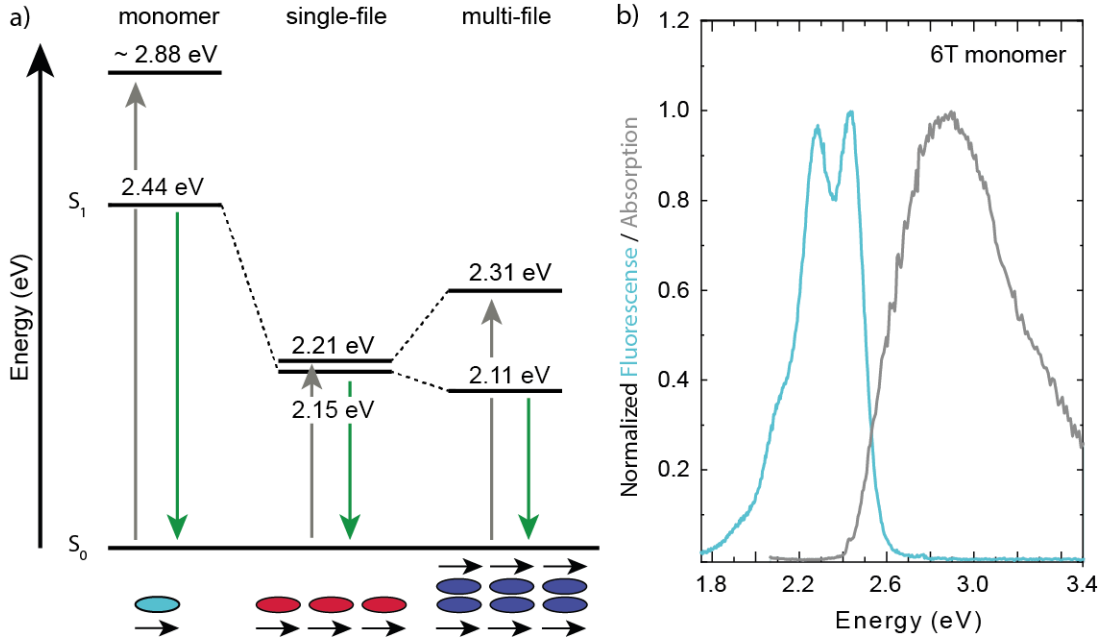

Figure 6.5 **Energy Shift Comparison of the Tube Bundle and Monomer. a)** Jablonski Diagram of the absorption (gray arrows) and fluorescence (green arrows) measurements on the tube bundle and monomer. The encapsulated molecules show a red shift of the absorption and emission compared to the monomer. Indicating the formation of agglomerates with strong J-character. **b)** Emission and Absorption of a 6T Monomer. The light blue (gray) curve shows the fluorescence (absorption) spectrum of the 6T monomer measured in solution and excited at 425 nm (detected at 510 nm), showing a large Stokes shift.

The collective shift of the 6T chains (290 meV) is very large compared to the observed red shifts in 2D molecular lattices (60 meV). [3, 11] Indeed, simulations of the 6T chains as a string of point dipoles separated by the molecular distance (2.51 nm) predict only a shift of 5 meV, black and dashed gray spectra in Fig. 6.6, although this model worked excellently for 2D lattices. [11] The applied model can be extended to take the finite size of the molecules into consideration, [208] yielding a much better fit to the experimental data, red line in Fig. 6.6. However, the necessary correction amounts to an effective dipole displacement on the same order of magnitude (96.5 %) as the physical length of 6T, which appears illusive. The physical origin of the extremely strong molecule-molecule interaction inside the

nanotube remains unreasonable, and should be the subject of further investigations. One possibility is a waveguiding effect of the encapsulating tube that enhances the Coulomb interaction between the molecular transition dipoles.

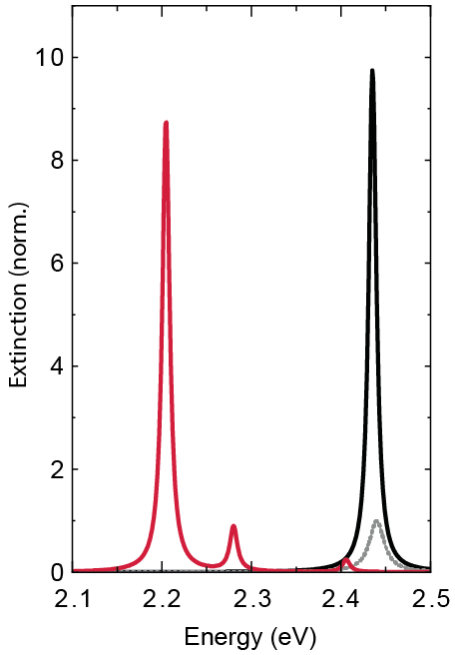

Figure 6.6 **Calculations of the Extinction of a 6T Single-File Chain.** Calculation without (black) and with (red) correction factor $g = 2.422\,\mathrm{nm}$. Both spectra are normalized to the extinction of a single dipole (gray dashed) with $\omega_0 = 2.44\,\mathrm{eV}$, $d_0 = 8.45\,\mathrm{D}$, [209] and $\gamma_0 = 5\,\mathrm{meV}$. Further parameters: lattice constant $a = 2.51\,\mathrm{nm}$, $\epsilon_m = 2.55$, and number of molecules $N = 10$. The dipole polarization was chosen along the x-direction.

The multi-file chain shows a smaller red shift of the absorption and a slightly larger red shift of the fluorescence, *i.e.*, effectively a splitting of the collective single-file state, Fig. 6.5a. The side-by-side configuration of the chains adds an anti-bonding configuration to the coupling of transition moments resulting in the splitting. The closer packing of the molecular chains compared to the in-chain separation leads to a stronger splitting of the excited state and thus an emission that is shifted further to the red compared to the single chain and in a larger Stokes shift (200 meV). [57, 206, 210] The shift of the absorption peak to smaller energies compared to the 6T monomer verifies that the J-character dominates the optical properties as expected for a multi-file molecular chain. Chains with a side-by-side configuration, *i.e.*, the molecules are oriented perpendicular to the nanotube axis, would result in a collective absorption at higher energies than the monomer and

a further increase in Stokes shift, [50, 206] in contrast to the dual red shift and smaller Stokes shift observed experimentally.
The FWHM of the 6T@BNNT spectrum further confirms our assignment of single- and multi-file chains. The single chain emission is narrower than the monomer and the multi-file emission, see Fig. 6.3a,c and Table 6.1. The collective state of J-aggregates has a reduced inhomogeneous broadening explaining the narrowing compared to the monomer. [11, 37] In addition, the absorption of the single chain is narrower than for several 6T files, because J-aggregates absorb predominantly into the lowest vibronic state whereas H-aggregates absorb in different vibronic levels of the excited state leading to a broadening of the absorption features. [11, 28]
Finally, we comment on the relative intensities of the single- and multi-file chains in fluorescence. J-aggregates are expected to show brighter emission from their collective state than H-aggregates, [11, 72, 73, 211] but we observed stronger emission from the multi-file chains. The observed intensities are most likely dominated by the smaller amount of tubes with single- than with multi-file chains. [159, 211] This is consistent with our observations of the extinction. The 0-0 emission is, in fact, dipole-forbidden for H-aggregates. Therefore, the peak intensity of the 0-0 emission decreases with increasing number of 6T chains inside the tube and vanishes for pure H-aggregates. [61, 196, 210, 212]

6.4 Conclusion

In conclusion, we studied absorption and emission from collective optical states of encapsulated 6T chains in BNNTs. By comparing the energetic position of the fluorescence and absorption the Stokes shift allowed us to identify the formation of single- and multi-file chains inside the nanotubes. The dominant configuration for the energy of the collective state is the J-type (head-to-tail) arrangement, we did not observe chains where the molecules are aligned in pure H-configuration or randomly orientated inside the tubes. The use of s-SNOM with its high spatial resolution made it possible to resolve which part of the tube bundle has a stronger absorption than other parts which is not possible with standard microscopic methods due to the large laser spot size covering the whole nanostructure. The very large shift of the single-file chain could not be modeled by the microscopic dipole model without the correction of the finite molecule size, requiring a further theoretical investigation. Additionally, it would be interesting to compare the one-dimensional

case with a two-dimensional lattice of 6T molecules.

7 | Plasmonic Bimetallic Two-Dimensional Supercrystals for H_2 Generation[1]

In this Chapter, I will change from a dipole coupled molecule systems to a plasmonic system. I will introduce a new system, a bimetallic supercrystal, that is able to increase the H_2 production in catalytic experiments due to the strong localized electric fields in the interparticle gaps of the crystal. First, I will show that small platinum particles integrated in the hotspots of the gold particle supercrystal will not significantly change the crystal structure and the optical properties of the crystal. FDTD simulations (see Method Sec. 4.3) show that the electric fields in the topmost layers of the crystal are responsible for the enhanced catalytic reaction. Together with an extensive characterization of the layer area sizes I calculate the wavelength dependent enhancement of the bimetallic crystal. Correlated with photocatalytic experiments done by M. Herran I show that the enhanced H_2 production is due to the strong electric fields and that charge transfer and heat generation play only a minor role.

[1]Parts of this chapter were published as *Plasmonic Bimetallic Two-Dimensional Supercrystals for H_2 Generation* in Herran and Juergensen et al. Nature Catalysis **6**, 1205–1214, DOI: 10.1038/s41929-023-01053-9 (2023). The project was conceived and planned by F. Schulz and Emiliano Cortés. The colloidal synthesis was done by M. Herran, A. Sousa-Castillo, and F. Schulz. The colloidal assembly was done by F. Schulz. The electron microscopy analysis was done by F. Schulz and A. Köppen. The photo catalytic experiments were performed by M. Herran. The optical spectroscopy and optical microscopy characterization was done by me, M. Kessens, and S. Reich. The FDTD simulations were done by me. The transient absorption spectroscopy was performed by D. Hoeing and H. Lange. M. Herran and me interpreted the data and wrote the manuscript. All authors commented on the manuscript.

7.1 Synthesis and Characterization of Two-Dimensional Supercrystals

The microscopical characterization of the synthesized mono- and bimetallic plasmonic supercrystals is presented in Fig. 7.1. The monometallic two-dimensional supercrystal (Au supercrystal) that serves as reference/control sample was fabricated according to a previously reported method in which individual gold nanoparticles (AuNPs) are used as building blocks, see Method Sec. 4.1.3. [12] The precise control of the synthesis of AuNPs, their surface chemistry, and the self-assembly step resulted in a well-packed hexagonal array of 22 nm AuNPs with an edge-to-edge distance of ∼2 nm, Fig. 7.1a. No crystalline arrangement other than hexagonal close packing of the large AuNPs was found in the sample when investigating different areas by transmission electron microscopy (TEM). The homogeneity of the structure over a large area is shown in the TEM image in Fig. 7.1b. These layers can extend up to a few square millimeters, Fig. 7.1c. In addition to monolayers, areas with multilayers also emerge during the crystallization process, Fig. 7.1c. The multilayers maintain the same crystalline phase [12], but they lead to different optical properties. With optical microscopy in transmission mode, we were able to identify the different layer numbers due to contrast difference, indicating different sample thicknesses. [10, 126] One example of the Au supercrystal in transmittance is depicted in Fig. 7.1c. The lighter the blue, the thinner the supercrystal. The unambiguous color contrast was utilized to measure the area size of the different layer numbers.

The colloidal approach to supercrystal fabrication was extended to bimetallic structures comprised of AuNPs and platinum nanoparticles (PtNPs). Through the same preparation methodology as used for Au supercrystals, we managed to assemble both 22 nm AuNPs and ∼3 nm PtNPs simultaneously, yielding a bimetallic supercrystal (AuPt supercrystal). The integration of platinum, a catalytically highly active metal, realized a supercrystal with combined optical and catalytic properties. In this composition the AuNPs dominate the optical behavior, whereas the PtNPs act as the active site for chemical reactions. The homogeneity and periodicity of the supercrystal was not affected by the presence of PtNPs, Fig. 7.1e. A higher-magnification TEM image revealed that during the assembly step the PtNPs were placed at the interparticle gaps between the AuNPs, which increased the gap size to

3.5 nm, Fig. 7.1d. At this point, it is important to emphasize that the small PtNPs were located in the interstices (gaps) of the two-dimensional hexagonal array of AuNPs and no direct contact exists between the two components of the bimetallic AuPt supercrystal. This structure is acknowledged to be an antenna–reactor configuration.

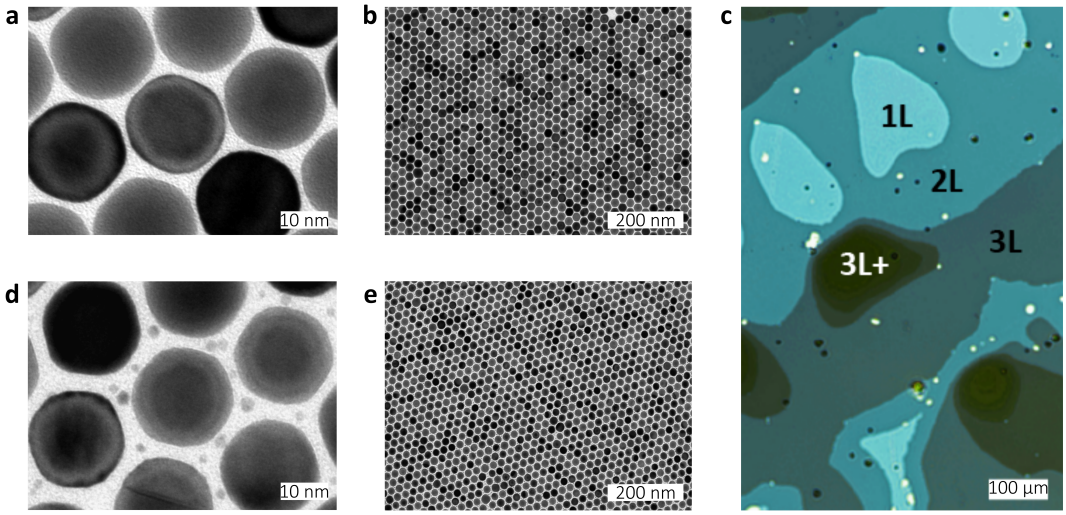

Figure 7.1 **Microscopic Characterization of the Supercrystals. (a,b)** TEM image of Au supercrystal made of 22 nm AuNP at two different magnifications. Interparticle gap of nanoparticles is ∼2 nm. **(c)** Representative transmission microscope image of the supercrystal. The different blue hues indicate different number of particle layers (1L, 2L, 3L and 3L+ stand for mono-, bi-, tri and multi-layers). **(d,e)** TEM of a bimetallic two-dimensional AuPt supercrystal at two different magnifications. ∼3 nm PtNPs are hosted at the interparticle gap (∼3.5 nm) between the 22 nm AuNP. No interface is created between the different metals.

The tunability of physical parameters, such as AuNP size, PtNP loading, interparticle gap size and number of layers, was confirmed by assembling larger particles with longer thiolated polystyrene (PSSH) ligands, which yielded similar results (*cf.* Fig. 7.8a). The assembly methodology was proven to work for different catalytic metals, as shown by replacing PtNPs with palladium NPs (PdNPs), Fig. 7.2, as well. Hence, the developed approach enables the creation of bimetallic supercrystals with a desired antenna–reactor combination, spanning several square millimeters consistently, while providing a broad range of tunable physical parameters. For a detailed explanation of the manufacturing process, see Method Sec. 4.1.3.

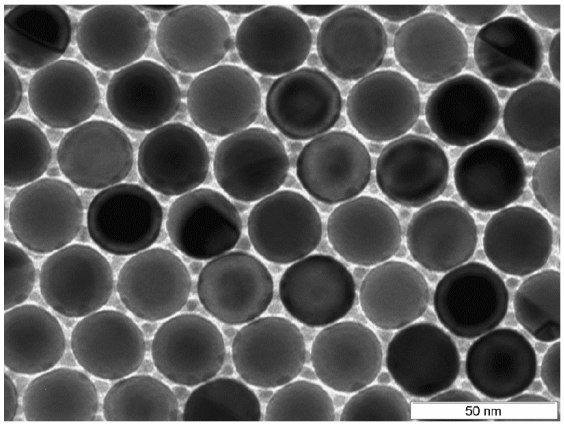

Figure 7.2 **Bimetallic Gold Palladium Supercrystal**. TEM images of AuPd supercrystals. The Au and Pd nanoparticles are in antenna-reactor configuration, similar to the AuPt supercrystal. The AuNPs form an hexagonal array with ∼5 nm Pd nanoparticles located in the interparticle gaps.

To investigate the optical properties of the indium tin oxide (ITO)-supported Au and AuPt supercrystals, micro-transmission and reflection measurements were performed on both supercrystals within the spectral range of 450-850 nm. The spectra were taken in both cases on monolayers, bilayers and trilayers (1L, 2L, 3L). The absorbance (A) was calculated afterwards as difference between the transmitted (T) and reflected (R) light, see Method Sec. 4.2.3. The resulting spectra for the pure gold supercrystals are shown in Fig. 7.3a and the spectra for the bimetallic sample in Fig. 7.3b. The obtained experimental spectra are in good agreement with the finite-difference time-domain (FDTD) simulations of both supercrystal structures, Fig. 7.3c,d. For the Au and AuPt supercrystals, the monolayer spectrum is dominated by interband transitions of the gold. [175] For bilayers and trilayers, the characteristic polaritonic modes that occur due to deep strong light–matter coupling start to appear between 650 and 750 nm. [10] The energetic position of these polaritonic resonances depends on the film thickness, the diameter of the particles, the gap size, and the dielectric environment. [10, 23] Thus, the small red shift of the bimetallic spectra with respect to the resonances presented by the monometallic supercrystal can be explained by the larger gap size, and by the changes in the refractive index of the background due to the presence of PtNPs. These interesting optical properties presented by supercrystals are related to the photocatalytic activity of the bimetallic structures.

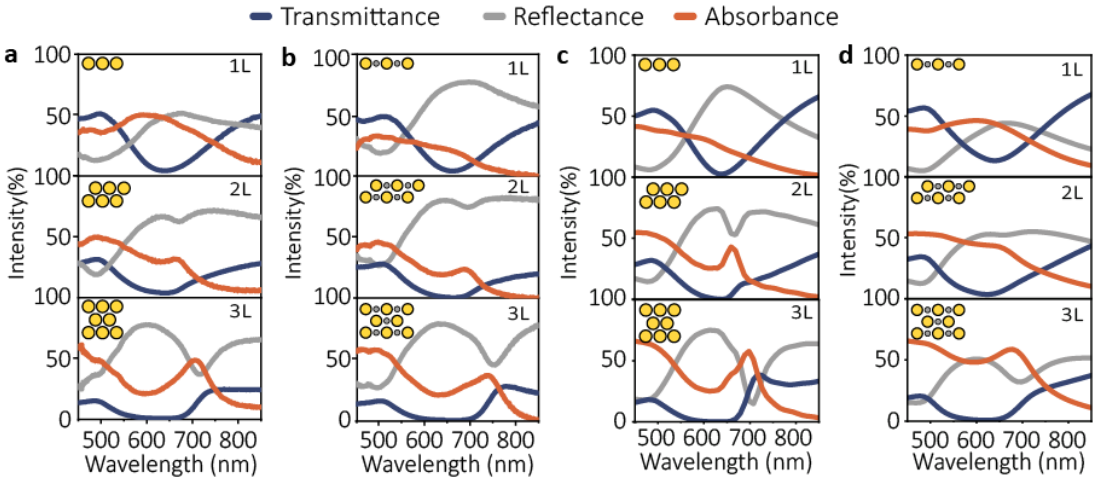

Figure 7.3 **Optical Characterization of the Supercrystals**. Experimental layer dependent reflectance (gray), transmittance (blue), and absorbance (orange) spectra of the **(a)** pure Au supercrystal and of the **(b)** bimetallic AuPt supercrystal. FDTD-Simulations of **(c)** the pure Au supercrystal (gap 2 nm) and of **(d)** the bimetallic AuPt supercrystal (gap 3.5 nm).

As mentioned above, the color contrast of the supercrystal layers imaged with an optical microscope in transmission mode made it possible to estimate the size of the domains. Thus, it was possible to calculate the overall optical response of the samples by weighting the experimental response of the individual layers by the different areas. It is important to know the ratios of the various layers because during the catalysis experiments a large area of the sample will be illuminated containing different numbers of layers. The details of the sample composition are given in Table 7.1. The study revealed that monolayers with ∼80% coverage for the control sample and ∼60% for the AuPt supercrystal make up the main part of the samples. The bimetallic sample also has a notable amount of trilayers and multilayers (∼30%), whereas the monometallic sample only consists of ∼3% multilayers.

Table 7.1 **Compositional Analysis by Optical Microscopy for both Au and AuPt Supercrystals**

Sample	Monolayer (1L)	Bilayer (2L)	Multilayer (3L+)
Au supercrystal	81%	16%	3%
AuPt supercrystal	61%	9%	30%

The optical behavior weighted by the area size (%) of the control and AuPt sample are depicted in Fig. 7.4a and b. As expected, due to the large contribution of monolayers, the overall response of the ITO-supported supercrystals was dominated by the interband transitions of the gold. In contrast to the pure Au supercrystal, the optical response of the AuPt sample shows an influence of the multilayers. Two shoulders are clearly visible in the absorbance spectrum at 671 and 732 nm due to the presence of the polaritonic modes in the bilayers and trilayers. Once the optical response of the samples was determined, they were tested as catalysts for formic acid dehydrogenation, see next section.

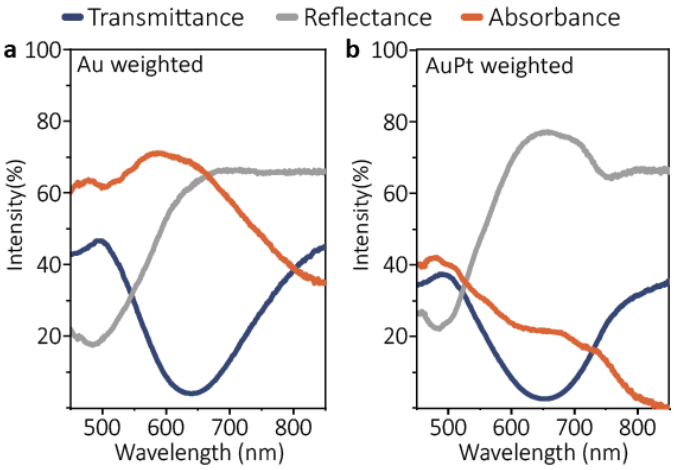

Figure 7.4 **Weighted Optical Characterization of the Supercrystals**. Weighted reflectance (gray), transmittance (blue) and absorbance (orange) spectra of **(a)** the pure Au and **(b)** the bimetallic supercrystal upon the composition study of the different layer numbers, Table 7.1.

7.2 Photocatalysis

The photocatalytic power of the resulting supercrystals was investigated by testing their performance on the formic acid decomposition without any further additives. The probe reaction was chosen based on the lower activity of gold versus platinum in this context, and also because it is a carbon-neutral H_2 carrier. [213–215] The experiments were carried out by M. Herran in the absence (dark) and presence of light and repeated at least three times each to ensure reproducibility. It has been shown that the probe redox reaction can follow two different pathways, namely dehydrogenation or dehydration. The former produces H_2 and CO_2 and is

favored thermodynamically ($\Delta G = -48.4\,\mathrm{kJ\,mol^{-1}}$), whereas the latter produces H_2O and CO ($\Delta G = -28.5\,\mathrm{kJ\,mol^{-1}}$). [213] CO was not detected throughout our experiments, excluding dehydration. For these studies a broadband lamp, equipped with an ultraviolet long-pass filter ($\lambda > 400\,\mathrm{nm}$) and an infrared filter, was used as illumination source, to work exclusively in the visible range of the spectrum and rule out heat generated from solvent absorption. An external cryostat set at 25°C was used to control the temperature during the reaction. The experiment was set up for the reactor to be illuminated with $\sim$110 mW cm^{-2}, which corresponds to sunlight irradiance. The stirring conditions helped to reduce any temperature gradient. [216]

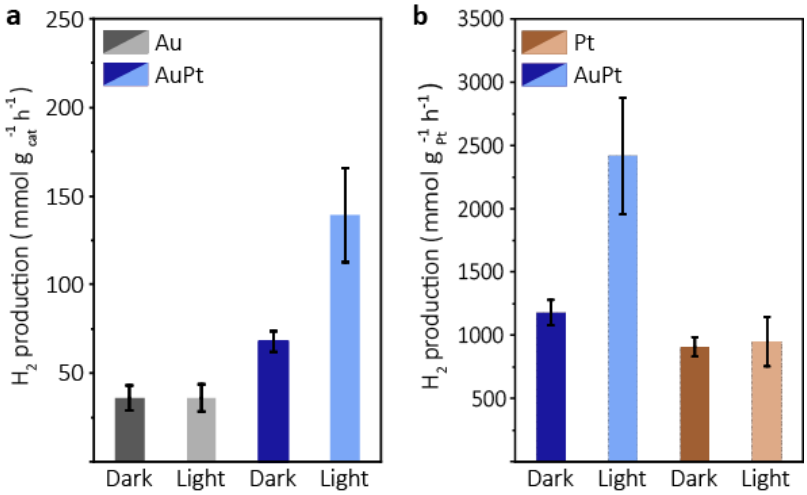

Figure 7.5 **Photocatalysis Performance on Formic Acid Dehydrogenation**. **(a)** H_2 generation rate normalized by the total mass of catalyst (Au or Au+Pt) in both conditions, dark and light for mono and bimetallic supercrystals. **(b)** H_2 generation rate normalized by the total mass of Pt. The Au and Pt control did not show enhancement upon illumination, while the AuPt presented a two-fold enhancement. Data are presented as the mean values of at least three independent measurements. Error bars represent the standard deviation.

Figure 7.5a shows the performances of ITO-supported Au and AuPt supercrystals when tested for the formic acid decomposition. The mass of the catalysts was obtained by inductively coupled plasma mass spectrometry (ICP-MS), while the preservation of the optical properties was monitored by optical spectroscopy. Figure 7.6 exemplary shows for the AuPt crystal that the optical properties do not change upon small changes in the crystal structure during the photocatalytic exper-

iments. The Au supercrystal presented an activity of 36 mmol g_{cat}^{-1} h^{-1} (Fig. 7.5a, dark gray) and a negligible enhancement upon illumination. Conversely, the inclusion of small amounts of PtNPs in the supercrystal increased the performance of the binary AuPt supercrystal up to 67 mmol g_{cat}^{-1} h^{-1} (Fig. 7.5a, dark blue). When illuminated with white light, the performance was increased by approximately a factor of two, reaching 139 mmol g_{cat}^{-1} h^{-1} (Fig. 7.5a, light blue). The improved performance of platinum under illumination in the experiments suggests that the interaction of the incoming light with the gold array results in energized platinum, useful for catalytic purposes. Indeed, the AuPt supercrystal appears to be the best plasmonic performer when formic acid is used as H_2 carrier. [217] Additionally, to assess the boost in PtNPs performance, the activity of the AuPt supercrystal was only normalized by the Pt mass and compared with a platinum control, evidencing its better performance when incorporated into the two-dimensional supercrystal, Fig. 7.5c.

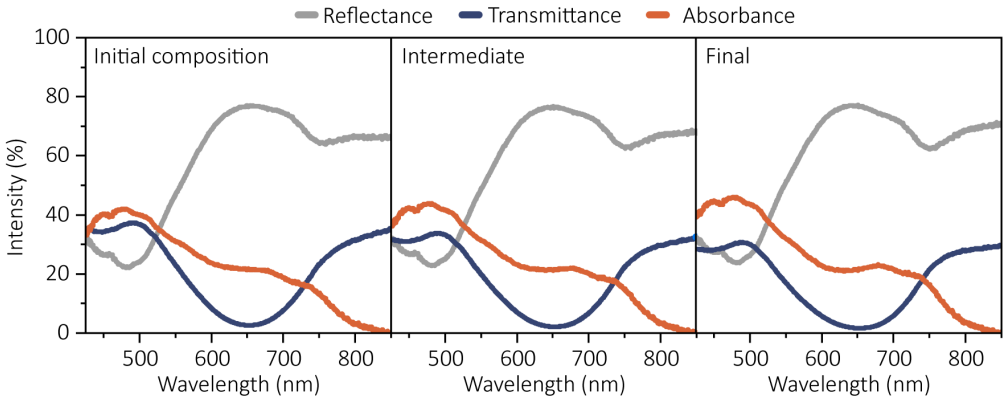

Figure 7.6 **Material Losses in AuPt Supercrystal.** Comparison of the optical response of the AuPt supercrystal between the catalytic experiments, showing the calculated optical response of the initial composition, an intermediate one and the final. It shows that the material loss did not change the total optical behavior of the sample (shape of the spectra). Note, the supercrystal size was always set to 100%.

Temperature-dependent experiments were conducted to evaluate the activation barrier (E_a). [218] We first investigated the temperature-dependent activity of the Au supercrystal versus the AuPt supercrystal over the 10-40°C temperature range, without illumination. As expected, the bimetallic sample always presented a larger activity Fig. 7.7a. While the activation barrier for the Au supercrystal was 40.7 kJ mol^{-1}, Fig. 7.7b, the one for the AuPt supercrystal was

33.4 kJ mol^{-1}, Fig. 7.7d, evidencing the superior activity due to the platinum. The same temperature-dependent study was carried out again, but now comparing the activity of AuPt supercrystal in dark and light over the same temperature range. Interestingly, we found the H_2 production was always enhanced across the range upon light assistance, although the enhancement factor was not constant. Despite this, the use of white light for photocatalysis resulted in a 10% decrease in the activation barrier for the Pt-formic-acid interface (Fig. 7.7c,d). All these experimental results highlight the synergy between the optical properties of the hexagonal array of 22 nm AuNPs and the interstitial PtNPs for sunlight-driven H_2 production.

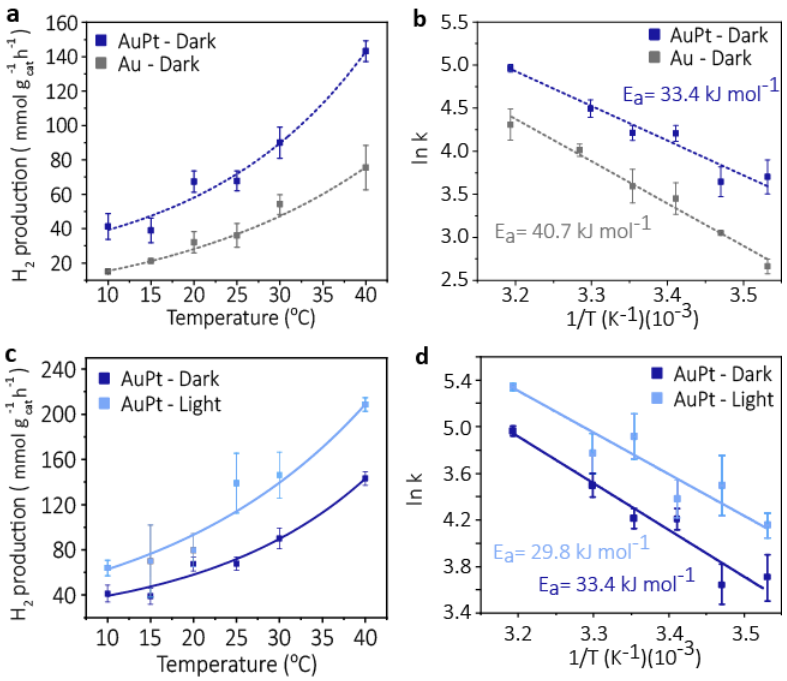

Figure 7.7 **Temperature Dependent Reaction Rates.** **(a)** Temperature-dependent catalytic experiments for both Au and AuPt supercrystals in the absence of light. Larger rates are observed for AuPt across the investigated temperature range. **(b)** Arrhenius plots for Au and AuPt for dark experiments giving the activation energy E_a. **(c)** Temperature-dependent catalytic experiments for the AuPt supercrystals in the in presence and absence of light. Coupling light to the crystal led to an increase of the rates at all temperatures. **(d)** Arrhenius plot for the AuPt supercrystal in presence and absence of light. E_a was reduced upon white light illumination. Data are presented as the mean value of at least three independent measurements. Error bars represent the standard deviation.

A similar trend was observed for the same system with larger gold NPs (39 nm), Fig. 7.8. In (a) the figure shows a TEM image of the crystal revealing a low platinum load. Nevertheless, a strong difference in the H_2 production between the absence and presents of light illumination was observed, confirming the higher production rate for bimetallic crystals compared to pure AuNP crystals. In the next section, we intend to disentangle the plasmonic contributions to the improved performance of AuPt with respect to H_2 generation.

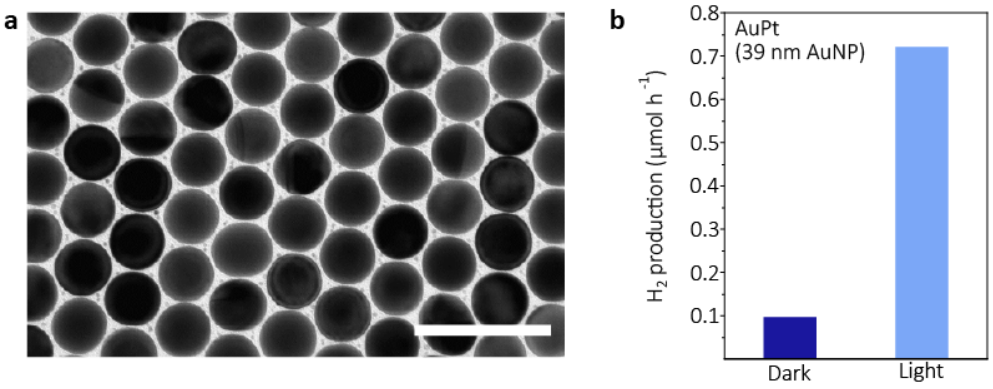

Figure 7.8 **AuPt Supercrystal with 39 nm AuNPs and low PtNP Loading (a)** TEM image of the AuPt supercrystal comprised of 39 nm AuNP and a low PtNP loading. Scale bar 100 nm. **(b)** Catalytic performance of the crystal in (a) on formic acid dehydrogenation in the presence and absence of light. An strong enhancement was observed for this system when light was coupled to the supercrystal. Data in photocatalytic experiments are presented as a single and independent measurement.

7.2.1 Mechanistic Insight

The superior photocatalytic activity of the AuPt clearly suggests that PtNPs benefit from the optical properties of the supercrystal. Several possible contributions are discussed for plasmonic photocatalysis with mono- or bimetallic systems: enhanced near fields, thermalized hot carriers, non-thermalized hot carriers and local heating. [152, 219–221] Hence, unraveling the dominant energy pathway improving PtNP performance at the interparticle gap of the gold array is crucial to fully exploit the advantages of such structures. A set of experiments were conducted to gain insight into the PtNP activation due to the interaction between the incoming light and the supercrystal.

First, wavelength-dependent catalytic experiments were performed on the bimetallic

supercrystal, which made it possible to discriminate the photocatalyst response in different spectral regions. [222] For these tests, the broadband lamp was equipped with bandpass filters centered at 450, 550, 650, 750, and 800 nm, with a bandwidth of 20 nm. The power (5 mW) was corrected for each wavelength to conduct the experiments with a constant irradiance and to match the power used previously with unfiltered light. The resulting wavelength-dependent H_2 generation rates are shown in Fig. 7.9, plotted together with the simulation of the enhanced electric field intensity at the hotspots for the topmost gold layer within the same spectral range, and the weighted absorbance. The relevance of hotspots in bimetallic plasmonic structures for photocatalysis has been proven for different systems. [223, 224] Only the top layer of each domain was considered in the simulations, as this is where the catalysis mainly occurs, as we will discuss in the following paragraph. The average electric field enhancement at the hotspots was calculated by FDTD-simulations, see Method Sec. 4.3. The simulations were evaluated in the center of an interparticle gap between two gold particles because this is the location where we expect the

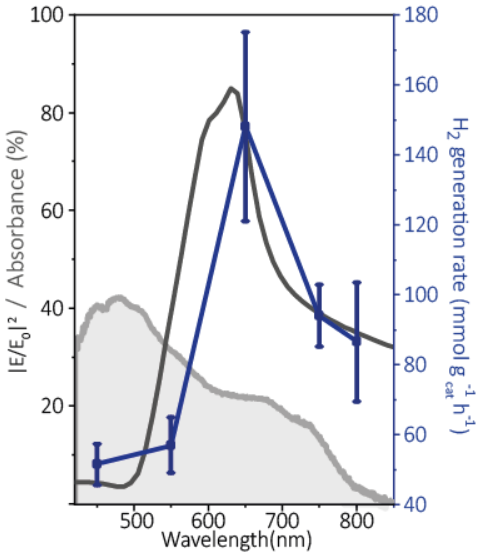

Figure 7.9 **Mechanistic Insight of AuPt Supercrystal Performance on Formic Acid Decomposition.** Wavelength dependent H_2 production (blue) plotted simultaneously with the calculated electric field strength (dark gray) in the hotspots within the visible range and the weighted measured absorbance (light gray). The photoactivity of the films peaks at 650 nm. Data are presented as the mean values of at least three independent measurements. Error bars represent the standard deviation.

PtNPs with the highest photocatalytic activity due to the strongest hotspots existing there.

We observed, that the photoactivity of the AuPt supercrystal correlates with the electric field enhancement: the reaction rate peaks at the enhancement maximum. Based on this result, it can be inferred that around 650 nm, the plasmonic components are funnelling more energy to the PtNPs, enhancing their absorption, and thus increasing the generation of excited carriers at the active metal which contribute to the redox reactions. [108, 223, 224]. This manifests as an improved performance in catalysis at that wavelength. Concomitantly, the maximized reaction rate does not coincide with the maximum of the absorbance, Fig. 7.3. This is an indication that the experimentally observed enhancement upon illumination is not primarily influenced by heat generated upon absorption by the supercrystals, but rather that the electric field enhancement facilitates the reaction. If heat had caused the rate increase, a larger enhancement would have been expected at shorter wavelengths, where the absorbance is higher, Fig. 7.9. [225]

The sample fabrication process yields two-dimensional supercrystals with monolayer, bilayer and multilayer domains, Table 7.1. Thus, it is worth investigating how the electric field enhancement depends on the number of layers. We simulated the spatial distribution of the electric field enhancement in the third dimension for different number of layers at 600 nm excitation wavelength, Fig. 7.10, the spectral range where we saw the highest catalytic activity. Consistent with Mueller *et al.* [23] it is almost exclusively the topmost layer that is plasmonically activated, giving a strong electric field that boosts the catalytic process. This is due to the plasmonic stop band, which unlike the polaritonic modes, does not allow the light to enter the supercrystal [10, 23], maximizing the field enhancement at the topmost layer.

Additional optical simulations were performed to screen the electric field enhancement across the gap (in the xy plane) when exciting the AuPt supercrystal in and out of the field enhancement maximum at 550, 650, and 800 nm, Fig. 7.11, covering the wavelength range used in photocatalytic experiments. The panels (a)-(c) in Fig. 7.11 depict the lattice unit cell of the FDTD simulations, showing the PtNPs in the strong hotspots of the AuNPs that are responsible for the enhancement and therefore for the high photocatalytic activity. While the presence of PtNPs leads to an electric field intensity enhancement of 10^3 times, Fig. 7.11d-f, a superior confinement is achieved at 650 nm, Fig. 7.11b,e. The intensity of the weighted

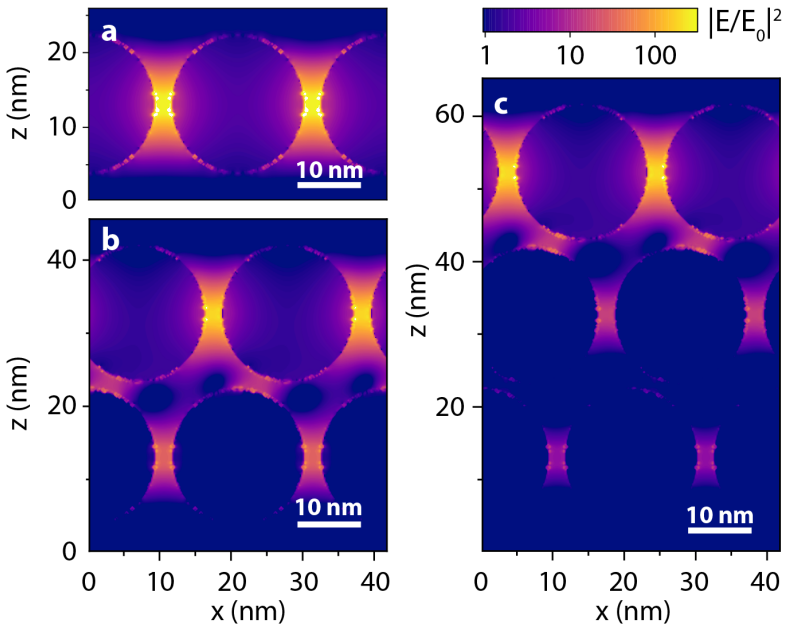

Figure 7.10 **FDTD-Simulations of the Spatial Electric Field Enhancement at 600 nm Excitation Wavelength.** Side view of supercrystals with 22 nm AuNPs and different layer number (a) one layer, (b) two layers, and (c) three layers. In all three cases the field enhancement is confined to the topmost layer. In the simulation the crystal was excited with x-polarized light.

electric field at 650 nm was almost three times larger than the intensity at the other wavelengths, Fig. 7.11. It is important to emphasize, that Fig. 7.9 was simulated without PtNPs in the gap, while Fig. 7.11a-f was calculated with PtNPs in the gaps between the AuNPs, leading to different electric field enhancement. However, both kinds of simulation show the strong enhancement at 650 nm and the same enhancement ratio between different wavelengths. The electric field enhancement simulations are in line with the experimental data. Interestingly, the H_2 generation rate at 800 nm was 1.6 times larger than at 550 nm, even though the absorbance at lower energy was negligible compared to the one at 550 nm, Fig. 7.3. This further supports our interpretation that heat is not the main plasmonic contribution to the enhanced performance of PtNPs.

Studying the plasmon relaxation of the excited sample makes it possible to gain an insight into the interaction between the constituents of the samples, and to precisely evaluate tunnelling from the plasmonic to the catalytic component driven by the

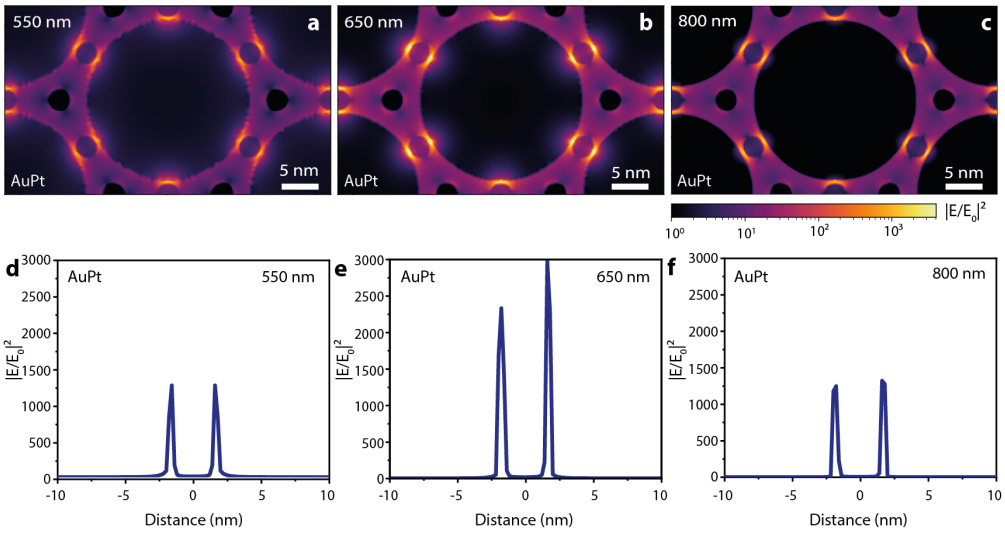

Figure 7.11 **FDTD-Simulations of the Electric Field Enhancement**. **(a, b, c)** Eclectic field enhancement maps of the AuPt supercrystal for different excitation wavelengths (550, 650 and 800 nm), showing the different hotspot intensities. **(d, e, f)** Line scan of the electric field enhancement over the gap of two AuNPs containing a PtNP. The PtNP is not placed in the center of the AuNPs leading to an asymmetric enhancement profile. All graphics show the sum of the topmost layer for 1L, 2L and 3L weighted by the percentages in Table 7.1. The asymmetry of the electric field is due to numerical inaccuracies.

enhanced electric field. [226, 227] To this end, the electronic dynamics of AuPt and Au supercrystals, and the platinum control, were investigated by transient absorption spectroscopy performed by D. Hoeing. [24] The results do not show essential changes in the hot electron dynamics, suggesting the absence of meaningful gold-to-platinum charge transfer when exciting the optically active layers in the wavelength regime under investigation. [228] This confirms once again the hypothesis that the electric fields in the hotspots drive the reaction. These measurements complemented the bulk wavelength-dependent experiments and optical simulations.

The evidence presented in this section sheds light on the mechanisms for harnessing light to boost the performance of plasmonic-catalytic nanoreactors. Our findings indicate that by incorporating PtNPs into the interparticle gaps of hexagonally arrayed 22 nm AuNPs, it is possible to turn a catalyst with weak visible light absorption into an active sunlight-type photocatalyst *via* enhanced excitation. From our experiments, we have effectively determined that the improved photoactivity is a

consequence of the interaction of strongly confined electromagnetic fields (hotspots) with interstitial PtNPs, whereas plasmonically generated heat, and charge injection from gold to platinum, appear in comparison to have minimal effect on the reaction rate enhancement. As such, and according to our pump–probe results, the main contribution of the plasmon in this hybrid structure is the activation of the catalytic sites (platinum) *via* the plasmonic (gold) enhanced near-fields. The increased performance of PtNPs upon illumination can be attributed to the generation of excited carriers (holes and electrons) participating in the redox cycle of formic acid dehydrogenation. The light-enhanced reaction rate is primarily due to the cleavage of the C–H bond, which represents the rate-limiting step of the reaction. [220, 224, 229, 230] These results highlight that accurately positioning catalytic metals in optical hotspots is a crucial parameter to modulate in these types of bimetallic photocalatysts. Various parameters, ranging from interparticle distance, constituent size or even the number of layers, can be modified to achieve greater electric fields at the hotspots, which in turn will impact the performance of these optocatalytic structures.

With these established design rules, efforts will be directed towards inexpensive and sustainable devices, which can be achieved with both earth-abundant plasmonic (copper, aluminum, magnesium) and catalytic (iron) metals, [231, 232] and the development of supports preserving the achieved supercrystal structure (mesoporous silica). In addition to formic acid dehydrogenation, we anticipate that the underlying physical principles described in our work will be exploited towards other important chemical transformations, such as CO_2 reduction or carbon–carbon coupling. [233, 234]

7.3 Conclusions

In this study, we introduce a plasmonic bimetallic supercrystal in which we achieved the desired antenna–reactor configuration from colloidal suspension. The size of the supercrystal can be extended up to several square millimeters while maintaining the configuration, and monolayer, bilayer, and multilayer domains can be achieved. We prove the synergistic effect of plasmonic-catalytic components in supercrystals by observing a two-fold increase in the rate of generation of H_2 in the formic acid dehydrogenation reaction at solar irradiance. By using well-defined supercrystals,

we were able to distinguish the plasmonic contributions to the catalytic enhancement. Our findings reveal that the performance of the PtNPs is primarily dictated by the intensity of the electromagnetic fields at the hotspots, whereas thermal contributions and charge injection from AuNP into the catalytic center have a lower impact on the reaction enhancement. In the future it would be interesting to perform catalytic experiments on samples with higher multi-layer amount to study the influence of the polaritonic modes on the H_2 generation.

8 | Summary and Outlook

The main aim of this thesis was the study of collective states in different low dimensional systems and to understand the mechanism behind it in more detail. Two-dimensional molecular lattices and one-dimensional molecule chains are ideal to study the transition from localized molecular transitions to collective states that are delocalized in space due to long range Coulomb coupling. It opens up a new promising path towards applications in optoelectronic devices. My motivation was to find out how robust collective states are against any kind of disorder. Further, I wanted to understand if the collective states also exist on materials that provide a strong radiative decay channel that quenches the intense fluorescence of the coupled state or if such a substrate can prevent the formation of coupled states. From first reports of the strong optical response and light emission from a MePTCDI monolayer on hBN by Zhao *et al.* [3] and giant Raman scattering of 6T molecules in carbon nanotubes by Gaufrès *et al.* [90] it was indicated that collective states were formed independently from the surrounding.

The second aim of my thesis was to investigate the usage of nanoparticle supercrystals as enhancer for catalytic reactions. It is well known that plasmonic structures can enhance the yield of H_2 during photocatalytic experiments. [149] The motivation was to find a structure that shows a higher H_2 generation rate in the formic acid decomposition than any plasmonic structure investigated so far. Bimetallic supercrystals, more precisely gold supercrystals with incorporated platinum nanoparticles, were promising candidates. The placement of the platinum particle in the hotspots of the gold crystal leads to an enhanced catalytic activity of the platinum. I showed that the optical properties of the bimetallic crystal changed only slightly compared to the pure gold crystal and showed with FDTD simulation at which wavelength the highest catalytic activity should be expected.

After the introduction of the fundamentals of molecular aggregates and plasmonics that are necessary to understand my experiments, I introduced the experimental methods.

Molecular Systems: To study two-dimensional molecular systems my first task was to built up an evaporation system that allows the growth of two-dimensional molecule layers. In a variety of adsorption runs I optimized the parameters to realize large scale molecular monolayers. Therefor, all free parameter, like the temperature, sample-to-source distance, the evaporation time, and inert gas flow were systematically changed until I observed layers that show the characteristic narrow and strong emission of molecular monolayers.

Monolayer growth on hBN and graphene have shown the same lattice constants, containing only one molecule per unit cell, indicating a close packing and strong coupling. I have shown that the fluorescence of the molecules is completely quenched on graphene, and therefor all the information about the kind of aggregation. Nevertheless, I was able to verify by micro-absorption measurements and wavelength dependent Raman scattering that the absorption of the molecule layer adsorbed on graphene is at the same energetic position as on hBN. Thus, I have shown that collective states also exist on materials with strong radiative loss channels, like (semi-)metals. With a real space model that is based on dipole-dipole coupling and allows the implementation of spatial and energetic disorder, as well as homogeneous broadening, it was shown that the collective state is quite robust against any type of disorder. The simulations have further shown that in a perfect dipole lattice, the mode where all dipoles point into the same direction, is not the mode with the largest frequency shift. The mode with the largest shift is a dark mode and can only be thermally activated.

To learn more about the molecule-molecule coupling and the interaction with the substrate further experiments are planed with different kinds of molecules that form different unit cells leading to lattices where the ratio of the J- to H-character in the lattice changes.
Collective states of one-dimensional molecule aggregates were studied in the second part of my experimental research. With different types of optical measurements I have shown that it is possible to assign the signal of a nanotube bundle filled

with 6T molecules to its particular origins (single- or multi-filed chains). Using the Stokes shift I was able to verify that for tubes filled with multi-file chains the J-character along the chains outweighs the H-character perpendicular to the chains. The observed Stokes shifts for both types of encapsulation (60 meV and 200 meV) were too strong that they could not be explained by a point dipole description of molecular transition moments, like used previously for the two-dimensional molecule lattice, and even appears to exceed a reasonable description with extended transition dipoles. A possible explanation is that the nanotube serves as waveguide, giving rise for the need to develop a new theoretical model.
Near-field absorption measurements with the s-SNOM enabled me to measure the absorption along the tube with high resolution. I showed that the absorption along the tube bundle varied which indicated an inhomogeneous spatial distribution of the molecules in the tubes, since the s-SNOM signal is proportional to the amount of material. The comparison of the far-field absorption measurements with near-field measurements showed an offset of 50 meV. This might be due to scattering effects of the far-field detection or the characteristic shift between optical near- and far-field measurements. [191, 204, 205]

Plasmonic System: In the last part of my thesis, I changed the coupled dipole system. Instead of organic systems I investigated a inorganic plasmonic system. I introduced a bimetallic supercrystal that consisted out of gold nanoparticles with small platinum particles in the gaps as an ideal candidate to enhance the H_2 generation in photocatalytic experiments. After extensive characterization of the different layer sizes by the different blue tones in the transmission microscope. I measured the layer dependent absorption of the crystal. The results showed that the optical response of the crystal with the platinum particles only slightly red shifted compared to the pure gold crystal. With FDTD simulations I have shown that the topmost layer of the crystals showed the strongest hotspots and therefore give the strongest contribution to the H_2 generation so that the other layers could be neglected. The expected field enhancement in the plasmonic hotspots was correlated with the area size of the different layers numbers to calculate an average electric field strength that can be compared to the wavelength dependent H_2 generation rate. The photocatalytic experiments performed by M. Herran complied with the predicted enhancement and thereby revealed that the catalytic performance of the platinum particles is mainly driven by the hotspots. Of particular note is that

the H_2 generation rate is higher compared to other top performers for formic acid dehydrogenation. The H_2 production was doubled under solar light illumination. Even without light illumination an increased H_2 generation was measured compared to the pure gold crystal due to the presents of the highly active Pt. Further, we have shown that also Pd particles can be incorporated into the crystal and the gold particle size can be changed giving similar results. Future experiments are planed to understand the role of thermal contributions and charge injection in the enhancement of the generation rate. Likewise we would like to stabilize the gold layers against degeneration due to the liquid environment during the catalysis and extend the measurements of the crystal with incorporated palladium particles that indicate an even higher enhancement of the H_2 generation.

Publications

1. **S. Juergensen**, J.-B. Marceau, C. Mueller, E.B. Barros, P. Kusch, A. Setaro, E. Gaufrès, and S. Reich, *Collective states of α-sexithiophene chains inside boron nitride nanotubes*, Nano Lett. (2024) - **submitted**

2. S. Kesarwani, **S. Juergensen**, Y. Staechelin, S. Reich, F. Schulz, and H. Lange, *Incorporation strategy for organic dyes into gold nanoparticle superlattices*, J. Chem. Phys. **161**, DOI: 10.1063/5.0209021, (2024) - **accepted**

3. M. Herran*, **S. Juergensen***, M. Kessens, D. Hoeing, A. Köppen, A. Sousa-Castillo, W.J. Parak, H. Lange, S. Reich, F. Schulz, and E. Cortés, *Plasmonic bimetallic two-dimensional supercrystals for H_2 generation*, Nature Catalysis **6**, 1205–1214, DOI: 10.1038/s41929-023-01053-9 (2023)

4. **S. Juergensen**, M. Kessens, C. Berrezueta-Palacios, N. Severin, S. Ifland, J.P. Rabe, N.S. Mueller, and S. Reich, *Collective states in molecular monolayers on 2D materials*, ACS Nano **17**, 17350–17358, DOI: 10.1103/PhysRevB.107.235122 (2023)

5. S. Wasserroth, G. Gordeev, **S. Juergensen**, P. Kusch, *Exploiting plasmonic enhancement with light-emitting diode excitation in surface-enhanced Raman scattering*, J. Raman Spectrosc. **53**, 1380, DOI: 10.1002/jrs.6369 (2022)

6. R. Schürmann, A. Nagel, **S. Juergensen**, A. Pathak, S. Reich, C. Pacholskia, and I. Bald, *Microscopic understanding of reaction rates observed in plasmon chemistry of nanoparticle-ligand systems*, J. Phys. Chem. C **126**, 5333, DOI: 10.1021/acs.jpcc.2c00278 (2022).

7. V. Deinhart, L.M. Kern, J.N. Kirchhof, **S. Juergensen**, J. Sturm, E. Krauss, T. Feichtner, S. Kovalchuk, M. Schneider, D. Engel, B. Pfau, B. Hecht, K.

Bolotin, S. Reich, and K. Höflich, *The patterning toolbox FIB-o-mat: Exploiting the full potential of focused helium ions for nanofabrication*, Beilstein J. Nanotechnol. **12**, 304, DOI: 10.3762/bjnano.12.25 (2021).

8. **S. Juergensen**, P. Kusch, and S. Reich, *Resonant Raman scattering of 4-nitrothiophenol*, Phys. Status Solidi B **257**, 2000295, DOI: 10.1002/pssb.202000295 (2020).

9. N.S. Mueller, Y. Okamura, B.G.M. Vieira, **S. Juergensen**, H. Lange, E.B. Barros, F. Schulz, and S. Reich, *Deep strong light–matter coupling in plasmonic nanoparticle crystals*, Nature **583**, 780, DOI: 10.1038/s41586-020-2508-1 (2020).

10. N.S. Mueller, **S. Juergensen**, K. Höflich, S. Reich, and P. Kusch, *Excitation-tunable tip-enhanced Raman spectroscopy*, J. Phys. Chem. C **122**, 28273, DOI: 10.1021/acs.jpcc.8b10272 (2018).

11. M. Glaeske, **S. Juergensen**, L. Gabrielli, E. Menna, F. Mancin, T. Gatti, and A. Setaro, *Plasmon-assisted energy transfer in hybrid nanosystems*, Phys. Status Solidi – Rapid Res. Lett. **12**, 1800508, DOI: 10.1002/pssr.201800508 (2018).

12. M. Glaeske, P. Bluemmel, **S. Juergensen**, A. Setaro, and S. Reich, *Dipole-switch induced modification of the emissive response of carbon nanotubes*, J. Condens. Matter. Phys. **29**, 454003, DOI: 10.1088/1361-648X/aa8dcf (2017).

13. L. Gabrielli, G. Altoè, M. Glaeske, **S. Juergensen**, S. Reich, A. Setaro, E. Menna, F. Mancin, and T. Gatti, *Controlling the decoration of the reduced graphene oxide surface with pyrene-functionalized gold nanoparticles*, Phys. Status Solidi B **254**, 11, DOI: 10.1002/pssb.201700281 (2017).

14. G. Gordeev, A. Setaro, M. Glaeske, **S. Jürgensen**, and S. Reich, *Doping in covalently functionalized carbon nanotubes: A Raman scattering study*, Pysic. Status Solidi B **253**, 2461, DOI: 10.1002/pssb.201600636 (2016).

*shared first authorship

Acknowledgments

At this point of my thesis I want to take the opportunity to thank all the people who have accompanied me over the last few years. Without all of you this thesis would not have been possible.

Special thanks goes to my supervisor, Stephanie Reich, for giving me the opportunity to write my PhD-Thesis in her group. You supported me from my bachelor's thesis onwards and gave me the opportunity to delve into many interesting topics in the world of nanomaterials. With your guidance, I have learned a lot over the years and always had the opportunity to pursue my own scientific interests. I am happy to stay for some more time in your group.

Further I would like to thank...

... Helénè Seiler for being my second supervisor on such short notice and for the discussions that we had on the two-dimensional molecule lattices.

... Niclas S. Müller with any question I could come to you or write to you and you were always so kind to help, no matter how busy or where in the world you were.

... Florian Schulz for the great collaboration and the countless gold particle samples that you synthesized for me since my master thesis as well as Holger Lange, Matias Herran and Emiliano Cortés for the great collaboration on the catalytic work.

... Nicolai Severin and Jürgen Raabe for taking the AFM measurements whenever we asked for them.

... Etienne Gaufrès and Jean-Baptiste Marceau for the encapsulated molecule chains and the great collaboration.

... Channi and Moritz for the trust in me as their master thesis supervisor.

... and of course my current and former group members Kati, Antonio, Patryk, Eduardo, Charly, Oisín, Arseniy, Gaby, José, Georgy, Niclas, Sören, Martin, and Mareen. You became my second family over the years. Together we had a lot of funny and great moments. I always could count on you if help was needed even without saying anything.

... last but not least Angelin and Gudrun you always support us and keep administrative matters as far away from us as possible.

Outside from the university, I would like to thank my family and friends for always supporting me through all my ups and downs, and for giving me so many wonderful moments without thinking about university. A very big thank you also goes to my boyfriend, Sören, who has been very understanding and patient with me over the last few weeks while I was writing my thesis.

Bibliography

[1] S.-W. Hsu, A. L. Rodarte, M. Som, G. Arya, and A. R. Tao. Colloidal plasmonic nanocomposites: From fabrication to optical function. *Chemical Reviews*, **118**, 3100–3120 (2018).

[2] S. B. Pyun, J. E. Song, J. Y. Kim, and E. C. Cho. Hydrochromic smart windows to remove harmful substances by mimicking medieval european stained glasses. *ACS Applied Materials Interfaces*, **12**, 16937–16945 (2020).

[3] H. Zhao, Y. Zhao, Y. Song, M. Zhou, W. Lv, L. Tao, Y. Feng, B. Song, Y. Ma, J. Zhang, J. Xiao, Y. Wang, D.-H. Lien, M. Amani, H. Kim, X. Chen, Z. Wu, Z. Ni, P. Wang, Y. Shi, H. Ma, X. Zhang, J.-B. Xu, A. Troisi, A. Javey, and X. Wang. Strong optical response and light emission from a monolayer molecular crystal. *Nature Communications*, **10** (2019).

[4] A. Sharma, L. Zhang, J. O. Tollerud, M. Dong, Y. Zhu, R. Halbich, T. Vogl, K. Liang, H. T. Nguyen, F. Wang, S. Sanwlani, S. K. Earl, D. Macdonald, P. K. Lam, J. A. Davis, and Y. Lu. Supertransport of excitons in atomically thin organic semiconductors at the 2d quantum limit. *Light: Science & Applications*, **9** (2020).

[5] H. Gao, W. Peng, Y. Liang, S. Chu, L. Yu, Z. Liu, and Y. Zhang. Plasmonic broadband perfect absorber for visible light solar cells application. *Plasmonics*, **15**, 573–580 (2019).

[6] N. P. Hylton, X. F. Li, V. Giannini, K. H. Lee, N. J. Ekins-Daukes, J. Loo, D. Vercruysse, P. Van Dorpe, H. Sodabanlu, M. Sugiyama, and S. A. Maier. Loss mitigation in plasmonic solar cells: aluminium nanoparticles for broadband photocurrent enhancements in gaas photodiodes. *Scientific Reports*, **3** (2013).

[7] Z. Geng, Y. Yu, and J. Liu. Broadband plasmonic photocatalysis enhanced by photothermal light absorbers. *The Journal of Physical Chemistry C*, **127**, 17723–17731 (2023).

[8] K. Yang, Y. Chen, S. Yan, and W. Yang. Nanostructured surface plasmon resonance sensors: Toward narrow linewidths. *Heliyon*, **9**, e16598 (2023).

[9] B. D. Thackray, V. G. Kravets, F. Schedin, G. Auton, P. A. Thomas, and A. N. Grigorenko. Narrow collective plasmon resonances in nanostructure arrays observed at normal light incidence for simplified sensing in asymmetric air and water environments. *ACS Photonics*, **1**, 1116–1126 (2014).

[10] N. S. Mueller, Y. Okamura, B. G. M. Vieira, S. Juergensen, H. Lange, E. B. Barros, F. Schulz, and S. Reich. Deep strong light–matter coupling in plasmonic nanoparticle crystals. *Nature*, **583**, 780–784 (2020).

[11] S. Juergensen, M. Kessens, C. Berrezueta-Palacios, N. Severin, S. Ifland, J. P. Rabe, N. S. Mueller, and S. Reich. Collective states in molecular monolayers on 2d materials. *ACS Nano*, **17**, 17350–17358 (2023).

[12] F. Schulz, O. Pavelka, F. Lehmkühler, F. Westermeier, Y. Okamura, N. S. Mueller, S. Reich, and H. Lange. Structural order in plasmonic superlattices. *Nature Communications*, **11** (2020).

[13] D. Barredo, S. de Léséleuc, V. Lienhard, T. Lahaye, and A. Browaeys. An atom-by-atom assembler of defect-free arbitrary two-dimensional atomic arrays. *Science*, **354**, 1021–1023 (2016).

[14] S. Juergensen, P. Kusch, and S. Reich. Resonant raman scattering of 4-nitrothiophenol. *physica status solidi (b)*, **257** (2020).

[15] M. Müller, A. Paulheim, A. Eisfeld, and M. Sokolowski. Finite size line broadening and superradiance of optical transitions in two dimensional long-range ordered molecular aggregates. *The Journal of Chemical Physics*, **139**, 044302 (2013).

[16] T. Dienel, C. Loppacher, S. Mannsfeld, R. Forker, and T. Fritz. Growth-mode-induced narrowing of optical spectra of an organic adlayer. *Advanced Materials*, **20**, 959–963 (2008).

[17] J. Kim, L. J. Cote, F. Kim, and J. Huang. Visualizing graphene based sheets by fluorescence quenching microscopy. *Journal of the American Chemical Society*, **132**, 260–267 (2009).

[18] H. R. Matte, K. Subrahmanyam, K. V. Rao, S. J. George, and C. Rao. Quenching of fluorescence of aromatic molecules by graphene due to electron transfer. *Chemical Physics Letters*, **506**, 260–264 (2011).

[19] J. J. Mock, M. Barbic, D. R. Smith, D. A. Schultz, and S. Schultz. Shape effects in plasmon resonance of individual colloidal silver nanoparticles. *The Journal of Chemical Physics*, **116**, 6755–6759 (2002).

[20] W. L. Barnes. Particle plasmons: Why shape matters. *American Journal of Physics*, **84**, 593–601 (2016).

[21] V. Voliani. *Gold Nanoparticles: An Introduction to Synthesis, Properties and Applications*. De Gruyter (2020).

[22] K. A. Dahan, Y. Li, J. Xu, and C. Kan. Recent progress of gold nanostructures and their applications. *Physical Chemistry Chemical Physics*, **25**, 18545–18576 (2023).

[23] N. S. Mueller, E. Pfitzner, Y. Okamura, G. Gordeev, P. Kusch, H. Lange, J. Heberle, F. Schulz, and S. Reich. Surface-enhanced raman scattering and surface-enhanced infrared absorption by plasmon polaritons in three-dimensional nanoparticle supercrystals. *ACS Nano*, **15**, 5523–5533 (2021).

[24] M. Herran, S. Juergensen, M. Kessens, D. Hoeing, A. Köppen, A. Sousa-Castillo, W. J. Parak, H. Lange, S. Reich, F. Schulz, and E. Cortés. Plasmonic bimetallic two-dimensional supercrystals for h2 generation. *Nature Catalysis*, **6**, 1205–1214 (2023).

[25] B. Valeur and M. N. Berberan-Santos. *Molecular Fluorescence: Principles and Applications*. Wiley (2012).

[26] E. C. L. Ru and P. G. Etchegoin. *Principles of Surface-Enhanced Raman Spectroscopy*. Elsevier (2009).

[27] J. R. Lakowicz, ed. *Principles of Fluorescence Spectroscopy*. Springer US (2006).

[28] M. Sauer, J. Hofkens, and J. Enderlein. *Handbook of Fluorescence Spectroscopy and Imaging: From Single Molecules to Ensembles*. Wiley (2011).

[29] M. A. Omary and H. H. Patterson. *Luminescence, Theory*, 636–653. Elsevier (2017).

[30] H. Haken and H. C. Wolf. *Molekülphysik und Quantenchemie: Einführung in die experimentellen und theoretischen Grundlagen*. Springer (2006).

[31] P. G. Baranov, H. J. von Bardeleben, F. Jelezko, and J. Wrachtrup. *Fundamentals of EPR Related Methods*, 113–178. Springer Vienna (2017).

[32] D. H. Arias, K. W. Stone, S. M. Vlaming, B. J. Walker, M. G. Bawendi, R. J. Silbey, V. Bulović, and K. A. Nelson. Thermally-limited exciton delocalization in superradiant molecular aggregates. *The Journal of Physical Chemistry B*, **117**, 4553–4559 (2012).

[33] M. Müller, A. Langner, O. Krylova, E. Le Moal, and M. Sokolowski. Fluorescence spectroscopy of ultrathin molecular organic films on surfaces. *Applied Physics B*, **105**, 67–79 (2011).

[34] C. Didraga and J. Knoester. Exchange narrowing in circular and cylindrical molecular aggregates: degenerate versus nondegenerate states. *Chemical Physics*, **275**, 307–318 (2002).

[35] J. Han, H. Zhang, and D. Abramavicius. Exchange narrowing and exciton delocalization in disordered j aggregates: Simulated peak shapes in the two dimensional spectra. *The Journal of Chemical Physics*, **139** (2013).

[36] M. Wubs and J. Knoester. Exchange narrowing in dynamically disordered molecular aggregates. *Chemical Physics Letters*, **284**, 63–70 (1998).

[37] E. Knapp. Lineshapes of molecular aggregates, exchange narrowing and intersite correlation. *Chemical Physics*, **85**, 73–82 (1984).

[38] R. Schäfer, L. Böhner, M. Schiek, D. Hertel, K. Meerholz, and K. Lindfors. Strong light–matter interaction of molecular aggregates with two excitonic transitions. *ACS Photonics*, **11**, 111–120 (2023).

[39] J. Tsutsumi, S. Matsuoka, I. Osaka, R. Kumai, and T. Hasegawa. Reduced exchange narrowing caused by gate-induced charge carriers in high-mobility donor–acceptor copolymers. *Physical Review B*, **95**, 115306 (2017).

[40] Y. Chen and J. Zhao. The mean-size dependence of the exchange narrowing in molecular j-aggregates. *Physica B: Condensed Matter*, **406**, 579–583 (2011).

[41] R. C. Hilborn. Einstein coefficients, cross sections, f values, dipole moments, and all that. *American Journal of Physics*, **50**, 982–986 (1982).

[42] J. R. Ferraro, K. Nakamoto, and C. W. Brown. *Introductory Raman Spectroscopy*. Elsevier (2003).

[43] D. A. Long. *The Raman Effect: A Unified Treatment of the Theory of Raman Scattering by Molecules*. John Wiley & Sons Ltd (2002).

[44] N. S. Mueller. Tailoring plasmon-enhanced light-matter interaction. Ph.D. thesis, Freie Universität Berlin (2020).

[45] S. Agnello, ed. *Spectroscopy for Materials Characterization*. Wiley (2021).

[46] J. Behringer and J. Brandmüller. Der resonanz-raman-effekt unter besonderer berücksichtigung neuerer russischer arbeiten. *Zeitschrift für Elektrochemie, Berichte der Bunsengesellschaft für physikalische Chemie*, **60**, 643–679 (1956).

[47] S. Wasserroth, S. Heeg, N. S. Mueller, P. Kusch, U. Hübner, E. Gaufrès, N. Y.-W. Tang, R. Martel, A. Vijayaraghavan, and S. Reich. Resonant, plasmonic raman enhancement of α-6t molecules encapsulated in carbon nanotubes. *The Journal of Physical Chemistry C*, **123**, 10578–10585 (2019).

[48] S. Heeg, L. Shi, T. Pichler, and L. Novotny. Raman resonance profile of an individual confined long linear carbon chain. *Carbon*, **139**, 581–585 (2018).

[49] N. J. Hestand and F. C. Spano. Expanded theory of h- and j-molecular aggregates: The effects of vibronic coupling and intermolecular charge transfer. *Chemical Reviews*, **118**, 7069–7163 (2018).

[50] J. L. Bricks, Y. L. Slominskii, I. D. Panas, and A. P. Demchenko. Fluorescent j-aggregates of cyanine dyes: basic research and applications review. *Methods and Applications in Fluorescence*, **6**, 012001 (2017).

[51] Y. Zhao, V. Wang, and A. Javey. Molecular materials with short radiative lifetime for high-speed light-emitting devices. *Matter*, **3**, 1832–1844 (2020).

[52] R. Gross and A. Marx. *Festkörperphysik*. De Gruyter (2018).

[53] D. Kim, S. Lee, J. Park, J. Lee, H. C. Choi, K. Kim, and S. Ryu. In-plane and out-of-plane excitonic coupling in 2d molecular crystals. *Nature Communications*, **14** (2023).

[54] A. Sharma, M. M. Hasan, and Y. Lu. Exciton dynamics in 2d organic semiconductors. *Materials Futures*, **1**, 042001 (2022).

[55] M. Kasha, H. R. Rawls, and M. Ashraf El-Bayoumi. The exciton model in molecular spectroscopy. *Pure and Applied Chemistry*, **11**, 371–392 (1965).

[56] R. Bernhardt, M. Manrho, J. Zablocki, L. Rieland, A. Lützen, M. Schiek, K. Meerholz, J. Zhu, T. L. C. Jansen, J. Knoester, and P. H. M. van Loosdrecht. Structural disorder as the origin of optical properties and spectral dynamics in squaraine nano-aggregates. *Journal of the American Chemical Society*, **144**, 19372–19381 (2022).

[57] J. Gierschner and S. Y. Park. Luminescent distyrylbenzenes: tailoring molecular structure and crystalline morphology. *Journal of Materials Chemistry C*, **1**, 5818 (2013).

[58] M. Bayda, F. Dumoulin, G. L. Hug, J. Koput, R. Gorniak, and A. Wojcik. Fluorescent h-aggregates of an asymmetrically substituted mono-amino zn(ii) phthalocyanine. *Dalton Transactions*, **46**, 1914–1926 (2017).

[59] C. J. Bardeen. Excitonic processes in molecular crystalline materials. *MRS Bulletin*, **38**, 65–71 (2013).

[60] A. P. Demchenko. *Fluorescent Organic Dyes and Conjugated Polymers in Nanoscale Ensembles*, 307–355. Springer International Publishing (2020).

[61] H. Yamagata and F. C. Spano. Interplay between intrachain and interchain interactions in semiconducting polymer assemblies: The HJ-aggregate model. *The Journal of Chemical Physics*, **136** (2012).

[62] A. P. Deshmukh, N. Geue, N. C. Bradbury, T. L. Atallah, C. Chuang, M. Pengshung, J. Cao, E. M. Sletten, D. Neuhauser, and J. R. Caram. Bridging the gap between h- and j-aggregates: Classification and supramolecular tunability for excitonic band structures in two-dimensional molecular aggregates. *Chemical Physics Reviews*, **3**, 021401 (2022).

[63] A. P. Deshmukh, D. Koppel, C. Chuang, D. M. Cadena, J. Cao, and J. R. Caram. Design principles for two-dimensional molecular aggregates using kasha's model: Tunable photophysics in near and short-wave infrared. *The Journal of Physical Chemistry C*, **123**, 18702–18710 (2019).

[64] S. Kirstein and H. Möhwald. Exciton band structures in 2d aggregates of cyanine dyes. *Advanced Materials*, **7**, 460–463 (1995).

[65] R. Bettles. *Cooperative Interactions in Lattices of Atomic Dipoles*. Springer Theses. Springer: Cham (2017).

[66] H. Qi and X. Fu. An in situ spectral monitoring scheme for advanced manufacturing of novel nanodevices. *Journal of Sensors*, **2022**, 1–10 (2022).

[67] K. Cong, Q. Zhang, Y. Wang, G. T. Noe, A. Belyanin, and J. Kono. Dicke superradiance in solids [invited]. *Journal of the Optical Society of America B*, **33**, C80 (2016).

[68] M. O. Scully and A. A. Svidzinsky. The super of superradiance. *Science*, **325**, 1510–1511 (2009).

[69] C. Zhu, S. C. Boehme, L. G. Feld, A. Moskalenko, D. N. Dirin, R. F. Mahrt, T. Stöferle, M. I. Bodnarchuk, A. L. Efros, P. C. Sercel, M. V. Kovalenko, and G. Rainò. Single-photon superradiance in individual caesium lead halide quantum dots. *Nature*, **626**, 535–541 (2024).

[70] F. C. Spano and H. Yamagata. Vibronic coupling in j-aggregates and beyond: A direct means of determining the exciton coherence length from the photoluminescence spectrum. *The Journal of Physical Chemistry B*, **115**, 5133–5143 (2010).

[71] J. Kerfoot, S. A. Svatek, V. V. Korolkov, T. Taniguchi, K. Watanabe, E. Antolin, and P. H. Beton. Fluorescence and electroluminescence of j-

aggregated polythiophene monolayers on hexagonal boron nitride. *ACS Nano*, **14**, 13886–13893 (2020).

[72] B. Sun, X. Xu, G. Zhou, L. Tao, W. Xinran, Z. Chen, and J.-B. Xu. Observation of strong j-aggregate light emission in monolayer molecular crystal on hexagonal boron nitride. *The Journal of Physical Chemistry A*, **124**, 7340–7345 (2020).

[73] A. Eisfeld, C. Marquardt, A. Paulheim, and M. Sokolowski. Superradiance from two dimensional brick-wall aggregates of dye molecules: The role of size and shape for the temperature dependence. *Physical Review Letters*, **119**, 097402 (2017).

[74] G. Rainò, H. Utzat, M. Bawendi, and M. Kovalenko. Superradiant emission from self-assembled light emitters: From molecules to quantum dots. *MRS Bulletin*, **45**, 841–848 (2020).

[75] D. J. Heijs, V. A. Malyshev, and J. Knoester. Decoherence of excitons in multichromophore systems: Thermal line broadening and destruction of superradiant emission. *Physical Review Letters*, **95**, 177402 (2005).

[76] C. Marquardt. Optical investigations on ptcda on kcl(100): Superradiant aggregates and single molecules. Ph.D. thesis, Rheinische Friedrich-Wilhelms-Universität Bonn (2019).

[77] R. J. Stöhr, R. Kolesov, K. Xia, R. Reuter, J. Meijer, G. Logvenov, and J. Wrachtrup. Super-resolution fluorescence quenching microscopy of graphene. *ACS Nano*, **6**, 9175–9181 (2012).

[78] A. Kasry, A. A. Ardakani, G. S. Tulevski, B. Menges, M. Copel, and L. Vyklicky. Highly efficient fluorescence quenching with graphene. *The Journal of Physical Chemistry C*, **116**, 2858–2862 (2012).

[79] Z. Chen, S. Berciaud, C. Nuckolls, T. F. Heinz, and L. E. Brus. Energy transfer from individual semiconductor nanocrystals to graphene. *ACS Nano*, **4**, 2964–2968 (2010).

[80] R. S. Swathi and K. L. Sebastian. Resonance energy transfer from a dye molecule to graphene. *The Journal of Chemical Physics*, **129** (2008).

[81] C. Brülke, O. Bauer, and M. M. Sokolowski. The influence of an interfacial hbn layer on the fluorescence of an organic molecule. *Beilstein Journal of Nanotechnology*, **11**, 1663–1684 (2020).

[82] M. Kratzer, A. Matkovic, and C. Teichert. Adsorption and epitaxial growth of small organic semiconductors on hexagonal boron nitride. *Journal of Physics D: Applied Physics*, **52**, 383001 (2019).

[83] A. Paulheim, C. Marquardt, M. Sokolowski, M. Hochheim, T. Bredow, H. Aldahhak, E. Rauls, and W. G. Schmidt. Surface induced vibrational modes in the fluorescence spectra of ptcda adsorbed on the kcl(100) and nacl(100) surfaces. *Physical Chemistry Chemical Physics*, **18**, 32891–32902 (2016).

[84] H. Guo, A. J. Martínez-Galera, and J. M. Gómez-Rodríguez. Molecular properties of ptcda on graphene grown on a rectangular symmetry substrate. *Applied Surface Science*, **620**, 156777 (2023).

[85] J. Kerfoot, V. V. Korolkov, A. S. Nizovtsev, R. Jones, T. Taniguchi, K. Watanabe, I. Lesanovsky, B. Olmos, N. A. Besley, E. Besley, and P. H. Beton. Substrate-induced shifts and screening in the fluorescence spectra of supramolecular adsorbed organic monolayers. *The Journal of Chemical Physics*, **149** (2018).

[86] M. Müller, E. L. Moal, R. Scholz, and M. Sokolowski. Exciton and polarization contributions to optical transition energies in an epitaxial organic monolayer on a dielectric substrate. *Physical Review B*, **83**, 241203 (2011).

[87] W. D. Xiao, Y. Y. Zhang, L. Tao, K. Aït-Mansour, K. Y. Chernichenko, V. G. Nenajdenko, P. Ruffieux, S. X. Du, H.-J. Gao, and R. Fasel. Impact of heterocirculene molecular symmetry upon two-dimensional crystallization. *Scientific Reports*, **4** (2014).

[88] H. Zhao, S. Zhang, S. Li, X. Song, W. Liu, B. Liu, and M. Dong. Investigation of the non-covalent interactions of molecular self-assembly by scanning tunneling microscopy using the association of aromatic structures in pyrene-4,5,9,10-tetraone and phenanthrene-9,10-dione molecules. *RSC Advances*, **5**, 103316–103320 (2015).

[89] S. S. Lampoura, C. Spitz, S. Dähne, J. Knoester, and K. Duppen. The optical dynamics of excitons in cylindrical j-aggregates. *The Journal of Physical Chemistry B*, **106**, 3103–3111 (2002).

[90] E. Gaufrès, N. Y.-W. Tang, F. Lapointe, J. Cabana, M.-A. Nadon, N. Cottenye, F. Raymond, T. Szkopek, and R. Martel. Giant raman scattering from j-aggregated dyes inside carbon nanotubes for multispectral imaging. *Nature Photonics*, **8**, 72–78 (2013).

[91] C. Allard, L. Schué, F. Fossard, G. Recher, R. Nascimento, E. Flahaut, A. Loiseau, P. Desjardins, R. Martel, and E. Gaufrès. Confinement of dyes inside boron nitride nanotubes: Photostable and shifted fluorescence down to the near infrared. *Advanced Materials*, **32** (2020).

[92] O. Bauer, G. Mercurio, M. Willenbockel, W. Reckien, C. Heinrich Schmitz, B. Fiedler, S. Soubatch, T. Bredow, F. S. Tautz, and M. Sokolowski. Role of functional groups in surface bonding of planar π-conjugated molecules. *Physical Review B*, **86**, 235431 (2012).

[93] C. Ludwig, B. Gompf, J. Petersen, R. Strohmaier, and W. Eisenmenger. Stm investigations of ptcda and ptcdi on graphite and mos2. a systematic study of epitaxy and stm image contrast. *Zeitschrift für Physik B Condensed Matter*, **93**, 365–373 (1994).

[94] D. K. Gramotnev and S. I. Bozhevolnyi. Plasmonics beyond the diffraction limit. *Nature Photonics*, **4**, 83–91 (2010).

[95] N. Zhou, V. López-Puente, Q. Wang, L. Polavarapu, I. Pastoriza-Santos, and Q.-H. Xu. Plasmon-enhanced light harvesting: applications in enhanced photocatalysis, photodynamic therapy and photovoltaics. *RSC Advances*, **5**, 29076–29097 (2015).

[96] S. A. Maier. *Plasmonics: Fundamentals and Applications*. Springer US (2007).

[97] C. F. Bohren and D. R. Huffman. *Absorption and Scattering of Light by Small Particles*. Wiley (1998).

[98] H. U. Yang, J. D'Archangel, M. L. Sundheimer, E. Tucker, G. D. Boreman, and M. B. Raschke. Optical dielectric function of silver. *Physical Review B*, **91**, 235137 (2015).

[99] P. B. Johnson and R. W. Christy. Optical constants of the noble metals. *Physical Review B*, **6**, 4370–4379 (1972).

[100] S.-Y. Ding, J. Yi, J.-F. Li, B. Ren, D.-Y. Wu, R. Panneerselvam, and Z.-Q. Tian. Nanostructure-based plasmon-enhanced raman spectroscopy for surface analysis of materials. *Nature Reviews Materials*, **1** (2016).

[101] C. Zhan, X.-J. Chen, J. Yi, J.-F. Li, D.-Y. Wu, and Z.-Q. Tian. From plasmon-enhanced molecular spectroscopy to plasmon-mediated chemical reactions. *Nature Reviews Chemistry*, **2**, 216–230 (2018).

[102] NanoComposix. https://nanocomposix.com/pages/mie-theory-calculator. Accessed: 2024-05-03.

[103] S. J. Oldenburg. Light scattering from gold nanoshells. Ph.D. thesis, Rice University (2000).

[104] A. Shafiqa, A. Abdul Aziz, and B. Mehrdel. Nanoparticle optical properties: Size dependence of a single gold spherical nanoparticle. *Journal of Physics: Conference Series*, **1083**, 012040 (2018).

[105] S. Schlücker, ed. *Surface Enhanced Raman Spectroscopy: Analytical, Biophysical and Life Science Applications*. Wiley (2010).

[106] Phornano. https://www.phornano.com/4ngold. Accessed: 2024-04-25.

[107] A. Minopoli, A. Acunzo, B. Della Ventura, and R. Velotta. Nanostructured surfaces as plasmonic biosensors: A review. *Advanced Materials Interfaces*, **9** (2021).

[108] S. Linic, S. Chavez, and R. Elias. Flow and extraction of energy and charge carriers in hybrid plasmonic nanostructures. *Nature Materials*, **20**, 916–924 (2021).

[109] C. W. Moon, M.-J. Choi, J. K. Hyun, and H. W. Jang. Enhancing photoelectrochemical water splitting with plasmonic au nanoparticles. *Nanoscale Advances*, **3**, 5981–6006 (2021).

[110] S. A. Lee and S. Link. Chemical interface damping of surface plasmon resonances. *Accounts of Chemical Research*, **54**, 1950–1960 (2021).

[111] N. S. Mueller, B. G. M. Vieira, D. Höing, F. Schulz, E. B. Barros, H. Lange, and S. Reich. Direct optical excitation of dark plasmons for hot electron generation. *Faraday Discussions*, **214**, 159–173 (2019).

[112] J. D. Jackson. *Electrodynamics, Classical.* John Wiley & Sons, Inc. (1962).

[113] F. Wang and Y. R. Shen. General properties of local plasmons in metal nanostructures. *Physical Review Letters*, **97**, 206806 (2006).

[114] L. Ye, W. Zhang, A. Hu, H. Lin, J. Tang, Y. Wang, C. Pan, P. Wang, X. Guo, L. Tong, Y. Gao, Q. Gong, and G. Lu. Plasmon–exciton coupling effect on plasmon damping. *Advanced Photonics Research*, **3** (2021).

[115] M. Ahlawat, D. Mittal, and V. Govind Rao. Plasmon-induced hot-hole generation and extraction at nano-heterointerfaces for photocatalysis. *Communications Materials*, **2** (2021).

[116] D. Mittal, M. Ahlawat, and V. Govind Rao. Recent progress and challenges in plasmon-mediated reduction of co2 to chemicals and fuels. *Advanced Materials Interfaces*, **9** (2022).

[117] G. V. Hartland, L. V. Besteiro, P. Johns, and A. O. Govorov. What's so hot about electrons in metal nanoparticles? *ACS Energy Letters*, **2**, 1641–1653 (2017).

[118] S. V. Boriskina, T. A. Cooper, L. Zeng, G. Ni, J. K. Tong, Y. Tsurimaki, Y. Huang, L. Meroueh, G. Mahan, and G. Chen. Losses in plasmonics: from mitigating energy dissipation to embracing loss-enabled functionalities. *Advances in Optics and Photonics*, **9**, 775 (2017).

[119] J. H. Hodak, I. Martini, and G. V. Hartland. Spectroscopy and dynamics of nanometer-sized noble metal particles. *The Journal of Physical Chemistry B*, **102**, 6958–6967 (1998).

[120] M. L. Brongersma, N. J. Halas, and P. Nordlander. Plasmon-induced hot carrier science and technology. *Nature Nanotechnology*, **10**, 25–34 (2015).

[121] M. Liu, M. Pelton, and P. Guyot-Sionnest. Reduced damping of surface plasmons at low temperatures. *Physical Review B*, **79**, 035418 (2009).

[122] H. Zhang, M. Ijaz, and R. J. Blaikie. Recent review of surface plasmons and plasmonic hot electron effects in metallic nanostructures. *Frontiers of Physics*, **18** (2023).

[123] E. Prodan, C. Radloff, N. J. Halas, and P. Nordlander. A hybridization model for the plasmon response of complex nanostructures. *Science*, **302**, 419–422 (2003).

[124] P. Nordlander, C. Oubre, E. Prodan, K. Li, and M. I. Stockman. Plasmon hybridization in nanoparticle dimers. *Nano Letters*, **4**, 899–903 (2004).

[125] P. K. Jain and M. A. El-Sayed. Plasmonic coupling in noble metal nanostructures. *Chemical Physics Letters*, **487**, 153–164 (2010).

[126] N. S. Mueller, B. G. M. Vieira, F. Schulz, P. Kusch, V. Oddone, E. B. Barros, H. Lange, and S. Reich. Dark interlayer plasmons in colloidal gold nanoparticle bi- and few-layers. *ACS Photonics*, **5**, 3962–3969 (2018).

[127] A. M. Michaels, Jiang, and L. Brus. Ag nanocrystal junctions as the site for surface-enhanced raman scattering of single rhodamine 6g molecules. *The Journal of Physical Chemistry B*, **104**, 11965–11971 (2000).

[128] B. Hou, M. Xie, R. He, M. Ji, S. Trummer, R. H. Fink, and L. Zhang. Microsphere assisted super-resolution optical imaging of plasmonic interaction between gold nanoparticles. *Scientific Reports*, **7** (2017).

[129] P. K. Jain, W. Huang, and M. A. El-Sayed. On the universal scaling behavior of the distance decay of plasmon coupling in metal nanoparticle pairs: A plasmon ruler equation. *Nano Letters*, **7**, 2080–2088 (2007).

[130] J. Sancho-Parramon and S. Bosch. Dark modes and fano resonances in plasmonic clusters excited by cylindrical vector beams. *ACS Nano*, **6**, 8415–8423 (2012).

[131] D. E. Gómez, Z. Q. Teo, M. Altissimo, T. J. Davis, S. Earl, and A. Roberts. The dark side of plasmonics. *Nano Letters*, **13**, 3722–3728 (2013).

[132] S. Reich, N. S. Mueller, and M. Bubula. Selection rules for structured light in nanooligomers and other nanosystems. *ACS Photonics*, **7**, 1537–1550 (2020).

[133] S. Hasegawa, H. Ichikawa, and K. Imura. Selective excitation of dark plasmon modes using cylindrical vector beams studied by microscopic imaging of nonlinear photoluminescence. *The Journal of Physical Chemistry C*, **128**, 2536–2542 (2024).

[134] L. Jiang, T. Yin, A. M. Dubrovkin, Z. Dong, Y. Chen, W. Chen, J. K. W. Yang, and Z. Shen. In-plane coherent control of plasmon resonances for plasmonic switching and encoding. *Light Sci Appl*, **8** (2019).

[135] F. Schulz, S. Tober, and H. Lange. Size-dependent phase transfer functionalization of gold nanoparticles to promote well-ordered self-assembly. *Langmuir*, **33**, 14437–14444 (2017).

[136] D. S. Dovzhenko, S. V. Ryabchuk, Y. P. Rakovich, and I. R. Nabiev. Light–matter interaction in the strong coupling regime: configurations, conditions, and applications. *Nanoscale*, **10**, 3589–3605 (2018).

[137] L. C. Andreani, G. Panzarini, and J.-M. Gérard. Strong-coupling regime for quantum boxes in pillar microcavities: Theory. *Physical Review B*, **60**, 13276–13279 (1999).

[138] J. P. Reithmaier, G. Sęk, A. Löffler, C. Hofmann, S. Kuhn, S. Reitzenstein, L. V. Keldysh, V. D. Kulakovskii, T. L. Reinecke, and A. Forchel. Strong coupling in a single quantum dot–semiconductor microcavity system. *Nature*, **432**, 197–200 (2004).

[139] S. De Liberato. Light-matter decoupling in the deep strong coupling regime: The breakdown of the purcell effect. *Physical Review Letters*, **112**, 016401 (2014).

[140] R. Chikkaraddy, B. de Nijs, F. Benz, S. J. Barrow, O. A. Scherman, E. Rosta, A. Demetriadou, P. Fox, O. Hess, and J. J. Baumberg. Single-molecule strong coupling at room temperature in plasmonic nanocavities. *Nature*, **535**, 127–130 (2016).

[141] T. Jaako, Z.-L. Xiang, J. J. Garcia-Ripoll, and P. Rabl. Ultrastrong-coupling phenomena beyond the dicke model. *Physical Review A*, **94**, 033850 (2016).

[142] G. A. Peterson, S. Kotler, F. Lecocq, K. Cicak, X. Y. Jin, R. W. Simmonds, J. Aumentado, and J. D. Teufel. Ultrastrong parametric coupling between a superconducting cavity and a mechanical resonator. *Physical Review Letters*, **123**, 247701 (2019).

[143] W. Qin, A. F. Kockum, C. S. Muñoz, A. Miranowicz, and F. Nori. Quantum amplification and simulation of strong and ultrastrong coupling of light and matter. *Physics Reports*, **1078**, 1–59 (2024).

[144] B. Luo, Z. Wang, T. Curk, G. Watson, C. Liu, A. Kim, Z. Ou, E. Luijten, and Q. Chen. Unravelling crystal growth of nanoparticles. *Nature Nanotechnology*, **18**, 589–595 (2023).

[145] D. Wang, M. Hermes, R. Kotni, Y. Wu, N. Tasios, Y. Liu, B. de Nijs, E. B. van der Wee, C. B. Murray, M. Dijkstra, and A. van Blaaderen. Interplay between spherical confinement and particle shape on the self-assembly of rounded cubes. *Nature Communications*, **9** (2018).

[146] W. Ding, Y. Xia, H. Song, T. Li, D. Yang, and A. Dong. Macroscopic superlattice membranes self-assembled from gold nanobipyramids with precisely tunable tip arrangements for sers. *Angewandte Chemie International Edition* (2024).

[147] E. B. Barros and S. Reich. Longitudinal polaritons in crystals. *arXiv:2311.03107* (2023).

[148] G. Job and R. Rüffler. *Katalyse*, 409–423. Springer Fachmedien Wiesbaden (2021).

[149] P. H. Camargo and E. Cortés. *Plasmonic Catalysis: From Fundamentals to Applications*. Wiley (2021).

[150] L. Zhou, D. F. Swearer, C. Zhang, H. Robatjazi, H. Zhao, L. Henderson, L. Dong, P. Christopher, E. A. Carter, P. Nordlander, and N. J. Halas. Quantifying hot carrier and thermal contributions in plasmonic photocatalysis. *Science*, **362**, 69–72 (2018).

[151] D. F. Swearer, H. Zhao, L. Zhou, C. Zhang, H. Robatjazi, J. M. P. Martirez, C. M. Krauter, S. Yazdi, M. J. McClain, E. Ringe, E. A. Carter, P. Nordlander, and N. J. Halas. Heterometallic antenna-reactor complexes for photocatalysis. *Proceedings of the National Academy of Sciences*, **113**, 8916–8920 (2016).

[152] B. Y. Zheng, H. Zhao, A. Manjavacas, M. McClain, P. Nordlander, and N. J. Halas. Distinguishing between plasmon-induced and photoexcited carriers in a device geometry. *Nature Communications*, **6** (2015).

[153] Z. Fang, Z. Liu, Y. Wang, P. M. Ajayan, P. Nordlander, and N. J. Halas. Graphene-antenna sandwich photodetector. *Nano Letters*, **12**, 3808–3813 (2012).

[154] U. Aslam, V. G. Rao, S. Chavez, and S. Linic. Catalytic conversion of solar to chemical energy on plasmonic metal nanostructures. *Nature Catalysis*, **1**, 656–665 (2018).

[155] C. Zhang, T. Kong, Z. Fu, Z. Zhang, and H. Zheng. Hot electron and thermal effects in plasmonic catalysis of nanocrystal transformation. *Nanoscale*, **12**, 8768–8774 (2020).

[156] A. Gellé and A. Moores. Plasmonic nanoparticles: Photocatalysts with a bright future. *Current Opinion in Green and Sustainable Chemistry*, **15**, 60–66 (2019).

[157] J. D. Fernandes, P. H. B. Aoki, R. F. Aroca, W. D. Macedo Junior, A. E. d. Souza, S. R. Teixeira, M. L. Braunger, C. d. A. Olivati, and C. J. L. Constantino. Supramolecular architecture and electrical properties of a perylene derivative in physical vapor deposited films. *Materials Research*, **18**, 127–137 (2015).

[158] M. Golshan, F. Amani, and M. Salami-Kalajahi. Photophysical and reflectance properties of perylene-3,4,9,10-tetracarboxylic diimide (ptcdi)/rhodamine 6g hybrid for application in cold paints. *Progress in Organic Coatings*, **157**, 106308 (2021).

[159] A. Badon, J.-B. Marceau, C. Allard, F. Fossard, A. Loiseau, L. Cognet, E. Flahaut, G. Recher, N. Izard, R. Martel, and E. Gaufrès. Fluorescence

anisotropy using highly polarized emitting dyes confined inside BNNTs. *Materials Horizons*, **10**, 983–992 (2023).

[160] Y. Zheng, X. Zhong, Z. Li, and Y. Xia. Successive, seed-mediated growth for the synthesis of single-crystal gold nanospheres with uniform diameters controlled in the range of 5–150 nm. *Particle & Particle Systems Characterization*, **31**, 266–273 (2014).

[161] M. Sanles-Sobrido, M. A. Correa-Duarte, S. Carregal-Romero, B. Rodriguez-Gonzalez, R. A. Alvarez-Puebla, P. Hervés, and L. M. Liz-Marzán. Highly catalytic single-crystal dendritic pt nanostructures supported on carbon nanotubes. *Chemistry of Materials*, **21**, 1531–1535 (2009).

[162] A. Dong, J. Chen, P. M. Vora, J. M. Kikkawa, and C. B. Murray. Binary nanocrystal superlattice membranes self-assembled at the liquid-air interface. *Nature*, **466**, 474–477 (2010).

[163] Y. Piao, J. R. Simpson, J. K. Streit, G. Ao, M. Zheng, J. A. Fagan, and A. R. H. Walker. Intensity ratio of resonant raman modes for (n,m) enriched semiconducting carbon nanotubes. *ACS Nano*, **10**, 5252–5259 (2016).

[164] J. G. Duque, H. Chen, A. K. Swan, A. P. Shreve, S. Kilina, S. Tretiak, X. Tu, M. Zheng, and S. K. Doorn. Violation of the condon approximation in semiconducting carbon nanotubes. *ACS Nano*, **5**, 5233–5241 (2011).

[165] N. Ocelic, A. Huber, and R. Hillenbrand. Pseudoheterodyne detection for background-free near-field spectroscopy. *Applied Physics Letters*, **89** (2006).

[166] attocube. https://www.attocube.com/en/products/microscopes/nanoscale-imaging-spectroscopy/technology/s-SNOM. Accessed: 2024-05-30.

[167] K. Yee. Numerical solution of initial boundary value problems involving maxwell's equations in isotropic media. *IEEE Transactions on Antennas and Propagation*, **14**, 302–307 (1966).

[168] U. S. Inan and R. A. Marshall. *Numerical Electromagnetics: The FDTD Method*. Cambridge University Press (2011).

[169] K. S. Kunz and R. J. Luebbers. *The Finite Difference Time Domain Method for Electromagnetics*. CRC Press (1993).

[170] B. Gallinet, J. Butet, and O. J. F. Martin. Numerical methods for nanophotonics: standard problems and future challenges. *Laser Photonics Reviews*, **9**, 577–603 (2015).

[171] R. Gunnarsson and M. Backstrom. Transmission cross section for apertures and arrays calculated using time-domain simulations. *2014 International Symposium on Electromagnetic Compatibility*. IEEE (2014).

[172] F. L. Teixeira, C. Sarris, Y. Zhang, D.-Y. Na, J.-P. Berenger, Y. Su, M. Okoniewski, W. C. Chew, V. Backman, and J. J. Simpson. Finite-difference time-domain methods. *Nature Reviews Methods Primers*, **3** (2023).

[173] Y. Cheng, G. Chen, X. Wang, and S. Yang. Investigation of numerical dispersion with time step of the fdtd methods: avoiding erroneous conclusions. *IET Microwaves, Antennas & Propagation*, **15**, 691–703 (2021).

[174] A. C. Lesina, A. Vaccari, P. Berini, and L. Ramunno. On the convergence and accuracy of the fdtd method for nanoplasmonics. *Optics Express*, **23**, 10481 (2015).

[175] B. G. M. Vieira, N. S. Mueller, E. B. Barros, and S. Reich. Plasmonic properties of close-packed metallic nanoparticle mono- and bilayers. *The Journal of Physical Chemistry C*, **123**, 17951–17960 (2019).

[176] R. L. Olmon, B. Slovick, T. W. Johnson, D. Shelton, S.-H. Oh, G. D. Boreman, and M. B. Raschke. Optical dielectric function of gold. *Physical Review B*, **86**, 235147 (2012).

[177] E. D. Palik, ed. *Handbook of Optical Constants of Solids*. Elsevier - Academic Press (1985).

[178] M. Orrit, D. Möbius, U. Lehmann, and H. Meyer. Reflection and transmission of light by dye monolayers. *The Journal of Chemical Physics*, **85**, 4966–4979 (1986).

[179] H. Fidder, J. Knoester, and D. A. Wiersma. Optical properties of disordered molecular aggregates: A numerical study. *The Journal of Chemical Physics*, **95**, 7880–7890 (1991).

[180] F. Würthner, T. E. Kaiser, and C. R. Saha-Möller. J-aggregates: From serendipitous discovery to supramolecular engineering of functional dye materials. *Angewandte Chemie International Edition*, **50**, 3376–3410 (2011).

[181] R. H. Dicke. Coherence in spontaneous radiation processes. *Physical Review*, **93**, 99–110 (1954).

[182] S. Ravets, H. Labuhn, D. Barredo, L. Béguin, T. Lahaye, and A. Browaeys. Coherent dipole–dipole coupling between two single rydberg atoms at an electrically-tuned förster resonance. *Nature Physics*, **10**, 914–917 (2014).

[183] N. Severin, A. R. Dzhanoev, H. Lin, A. Rauf, S. Kirstein, C.-A. Palma, I. M. Sokolov, and J. P. Rabe. Atomic resolution with high-eigenmode tapping mode atomic force microscopy. *Physical Review Research*, **4**, 023149 (2022).

[184] S. K. Saikin, A. Eisfeld, S. Valleau, and A. Aspuru-Guzik. Photonics meets excitonics: natural and artificial molecular aggregates. *Nanophotonics*, **2**, 21–38 (2013).

[185] K. Berland and P. Hyldgaard. Analysis of van der waals density functional components: Binding and corrugation of benzene and c60 on boron nitride and graphene. *Physical Review B*, **87**, 205421 (2013).

[186] E. Engel, K. Schmidt, D. Beljonne, J.-L. Brédas, J. Assa, H. Fröb, K. Leo, and M. Hoffmann. Transient absorption spectroscopy and quantum-chemical studies of matrix-isolated perylene derivatives. *Physical Review B*, **73**, 245216 (2006).

[187] A. Laturia, M. L. V. de Put, and W. G. Vandenberghe. Dielectric properties of hexagonal boron nitride and transition metal dichalcogenides: from monolayer to bulk. *npj 2D Materials and Applications*, **2** (2018).

[188] K. Akers, R. Aroca, A. Hort, and R. Loutfy. Molecular organization in perylene tetracarboxylic di-imide solid films. *Spectrochimica Acta Part A: Molecular Spectroscopy*, **44**, 1129–1135 (1988).

[189] E. Lunedei. Distance dependent excited-state relaxation of meptcdi on semiconductor substrates in the isolated molecule limit (2003). Accessed: 2023-05-22.

[190] P. Y. Yu and M. Cardona. *Fundamentals of Semiconductors*. Springer: Berlin - Heidelberg (2010).

[191] S. Wasserroth, T. Bisswanger, N. S. Mueller, P. Kusch, S. Heeg, N. Clark, F. Schedin, R. Gorbachev, and S. Reich. Graphene as a local probe to investigate near-field properties of plasmonic nanostructures. *Physical Review B*, **97**, 155417 (2018).

[192] A. Arbouet, D. Christofilos, N. Del Fatti, F. Vallée, J. R. Huntzinger, L. Arnaud, P. Billaud, and M. Broyer. Direct measurement of the single-metal-cluster optical absorption. *Physical Review Letters*, **93**, 127401 (2004).

[193] M. S. Devadas, Z. Li, and G. V. Hartland. Imaging and analysis of single optically trapped gold nanoparticles using spatial modulation spectroscopy. *The Journal of Physical Chemistry Letters*, **5**, 2910–2915 (2014).

[194] M. S. Devadas, T. Devkota, S. Guha, S. K. Shaw, B. D. Smith, and G. V. Hartland. Spatial modulation spectroscopy for imaging and quantitative analysis of single dye-doped organic nanoparticles inside cells. *Nanoscale*, **7**, 9779–9785 (2015).

[195] S. Zhao, M. Riedel, J. Patarroyo, N. Bastus, V. Puntes, Z. Yue, F. Lisdat, and W. J. Parak. Introducing visible-light sensitivity into photocatalytic ceo 2 nanoparticles by hybrid particle preparation exploiting plasmonic properties of gold: enhanced photoelectrocatalysis exemplified for hydrogen peroxide sensing. *Nanoscale*, **13**, 980–990 (2021).

[196] S. Bhagat, W. D. Leal, M. B. Majewski, J. Simbrunner, S. Hofer, R. Resel, and I. Salzmann. Aggregate formation in crystalline blends of α-sexithiophene and para-sexiphenyl. *Electronic Structure*, **3**, 034004 (2021).

[197] M. T. W. Milder, J. L. Herek, J. Areephong, B. L. Feringa, and W. R. Browne. Tunable aggregation and luminescence of bis(diarylethene)sexithiophenes. *The Journal of Physical Chemistry A*, **113**, 7717–7724 (2009).

[198] Y. Song, G. Pan, C. Zhang, C. Wang, B. Xu, and W. Tian. Organic luminescent crystals: role of packing structures and optical properties. *Materials Chemistry Frontiers*, **7**, 5104–5119 (2023).

[199] L. Blinov, S. Palto, G. Ruani, C. Taliani, A. Tevosov, S. Yudin, and R. Zamboni. Location of charge transfer states in α-sexithienyl determined by the electroabsorption technique. *Chemical Physics Letters*, **232**, 401–406 (1995).

[200] F. Kouki, P. Spearman, P. Valat, G. Horowitz, and F. Garnier. Experimental determination of excitonic levels in α-oligothiophenes. *The Journal of Chemical Physics*, **113**, 385–391 (2000).

[201] T. Taubner, R. Hillenbrand, and F. Keilmann. Nanoscale polymer recognition by spectral signature in scattering infrared near-field microscopy. *Applied Physics Letters*, **85**, 5064–5066 (2004).

[202] S. Mastel, A. A. Govyadinov, T. V. A. G. de Oliveira, I. Amenabar, and R. Hillenbrand. Nanoscale-resolved chemical identification of thin organic films using infrared near-field spectroscopy and standard fourier transform infrared references. *Applied Physics Letters*, **106** (2015).

[203] I. Niehues, L. Mester, E. Vicentini, D. Wigger, M. Schnell, and R. Hillenbrand. Identification of weak molecular absorption in single-wavelength s-SNOM images. *Optics Express*, **31**, 7012 (2023).

[204] J. Zuloaga and P. Nordlander. On the energy shift between near-field and far-field peak intensities in localized plasmon systems. *Nano Letters*, **11**, 1280–1283 (2011).

[205] A. Estrada-Real, I. Paradisanos, P. R. Wiecha, J.-M. Poumirol, A. Cuche, G. Agez, D. Lagarde, X. Marie, V. Larrey, J. Müller, G. Larrieu, V. Paillard, and B. Urbaszek. Probing the optical near-field interaction of mie nanoresonators with atomically thin semiconductors. *Communications Physics*, **6** (2023).

[206] F. C. Spano. The spectral signatures of frenkel polarons in h- and j-aggregates. *Accounts of Chemical Research*, **43**, 429–439 (2009).

[207] G. Gordeev, S. Wasserroth, H. Li, A. Jorio, B. S. Flavel, and S. Reich. Dielectric screening inside carbon nanotubes. *Nano Letters*, **24**, 8030–8037 (2024).

[208] L. Romaner, G. Heimel, C. Ambrosch-Draxl, and E. Zojer. The dielectric constant of self-assembled monolayers. *Advanced Functional Materials*, **18**, 3999–4006 (2008).

[209] M. Andrzejak and P. Petelenz. Mesoscopic disorder in thin film spectra: absorption spectroscopy of sexithiophene. *Chemical Physics Letters*, **332**, 435–441 (2000).

[210] T. Eder, D. Kraus, S. Höger, J. Vogelsang, and J. M. Lupton. Vibrations responsible for luminescence from hj-aggregates of conjugated polymers identified by cryogenic spectroscopy of single nanoparticles. *ACS Nano*, **16**, 6382–6393 (2022).

[211] J. B. Marceau, D. M. Ta, A. Aguilar, A. Loiseau, R. Martel, P. Bon, R. Voituriez, G. Recher, and E. Gaufrès. Forming 1d periodic j-aggregates by mechanical bending of bnnts: Evidence of activated molecular diffusion (2024).

[212] M. A. Loi, E. da Como, F. Dinelli, M. Murgia, R. Zamboni, F. Biscarini, and M. Muccini. Supramolecular organization in ultra-thin films of α-sexithiophene on silicon dioxide. *Nature Materials*, **4**, 81–85 (2004).

[213] J. Eppinger and K. W. Huang. Formic acid as a hydrogen energy carrier. *ACS Energy Letters*, **2**, 188–195 (2017).

[214] K. Tedsree, T. Li, S. Jones, C. W. A. Chan, K. M. K. Yu, P. A. Bagot, E. A. Marquis, G. D. Smith, and S. C. E. Tsang. Hydrogen production from formic acid decomposition at room temperature using a ag–pd core–shell nanocatalyst. *Nature nanotechnology*, **6**, 302–307 (2011).

[215] M. Czaun, J. Kothandaraman, A. Goeppert, B. Yang, S. Greenberg, R. B. May, G. A. Olah, and G. S. Prakash. Iridium-catalyzed continuous hydrogen generation from formic acid and its subsequent utilization in a fuel cell: toward a carbon neutral chemical energy storage. *ACS Catalysis*, **6**, 7475–7484 (2016).

[216] I.-W. Un and Y. Sivan. The role of heat generation and fluid flow in plasmon-enhanced reduction–oxidation reactions. *ACS Photonics*, **8**, 1183–1190 (2021).

[217] S. Ezendam, M. Herran, L. Nan, C. Gruber, Y. Kang, F. Gröbmeyer, R. Lin, J. Gargiulo, A. Sousa-Castillo, and E. Cortés. Hybrid plasmonic nanomaterials for hydrogen generation and carbon dioxide reduction. *ACS Energy Letters*, **7**, 778–815 (2022).

[218] J. Zhou, W. Zhang, X.-F. Jiang, C. Wang, X. Zhou, B. Xu, L. Liu, Z. Xie, and Y. Ma. Magic-angle stacking and strong intermolecular pi-pi interaction in a perylene bisimide crystal: An approach for efficient near-infrared (NIR) emission and high electron mobility. *The Journal of Physical Chemistry Letters*, **9**, 596–600 (2018).

[219] M. Rodio, M. Graf, F. Schulz, N. S. Mueller, M. Eich, and H. Lange. Experimental evidence for nonthermal contributions to plasmon-enhanced electrochemical oxidation reactions. *ACS catalysis*, **10**, 2345–2353 (2020).

[220] B. Wu, J. Lee, S. Mubeen, Y.-S. Jun, G. D. Stucky, and M. Moskovits. Plasmon-mediated photocatalytic decomposition of formic acid on palladium nanostructures. *Advanced Optical Materials*, **4**, 1041–1046 (2016).

[221] J. Gargiulo, M. Herran, I. L. Violi, A. Sousa-Castillo, L. P. Martinez, S. Ezendam, M. Barella, H. Giesler, R. Grzeschik, S. Schlücker, S. A. Maier, F. D. Stefani, and E. Cortés. Impact of bimetallic interface design on heat generation in plasmonic au/pd nanostructures studied by single-particle thermometry. *Nature communications*, **14**, 1–11 (2023).

[222] G. Baffou, I. Bordacchini, A. Baldi, and R. Quidant. Simple experimental procedures to distinguish photothermal from hot-carrier processes in plasmonics. *Light: Science & Applications*, **9**, 1–16 (2020).

[223] S. Lee, H. Hwang, W. Lee, D. Schebarchov, Y. Wy, J. Grand, B. Auguié, D. H. Wi, E. Cortés, and S. W. Han. Core–shell bimetallic nanoparticle trimers for efficient light-to-chemical energy conversion. *ACS Energy Letters*, **5**, 3881–3890 (2020).

[224] M. Herran, A. Sousa-Castillo, C. Fan, S. Lee, W. Xie, M. Döblinger, B. Auguié, and E. Cortés. Tailoring plasmonic bimetallic nanocatalysts toward sunlight-driven h2 production. *Advanced Functional Materials*, **32**, 2203418 (2022).

[225] K. Li, N. J. Hogan, M. J. Kale, N. J. Halas, P. Nordlander, and P. Christopher. Balancing near-field enhancement, absorption, and scattering for effective antenna–reactor plasmonic photocatalysis. *Nano letters*, **17**, 3710–3717 (2017).

[226] S. Link and M. A. El-Sayed. Shape and size dependence of radiative, non-radiative and photothermal properties of gold nanocrystals. *International reviews in physical chemistry*, **19**, 409–453 (2000).

[227] K. J. Savage, M. M. Hawkeye, R. Esteban, A. G. Borisov, J. Aizpurua, and J. J. Baumberg. Revealing the quantum regime in tunnelling plasmonics. *Nature*, **491**, 574–577 (2012).

[228] C. Engelbrekt, K. T. Crampton, D. A. Fishman, M. Law, and V. A. Apkarian. Efficient plasmon-mediated energy funneling to the surface of au@ pt core–shell nanocrystals. *ACS nano*, **14**, 5061–5074 (2020).

[229] S. Zhao, M. Riedel, J. Patarroyo, N. G. Bastús, V. Puntes, Z. Yue, F. Lisdat, and W. J. Parak. Tailoring of the photocatalytic activity of ceo 2 nanoparticles by the presence of plasmonic ag nanoparticles. *Nanoscale*, **14**, 12048–12059 (2022).

[230] L. Han, L. Zhang, H. Wu, H. Zu, P. Cui, J. Guo, R. Guo, J. Ye, J. Zhu, X. Zheng, et al. Anchoring pt single atoms on te nanowires for plasmon-enhanced dehydrogenation of formic acid at room temperature. *Advanced Science*, **6**, 1900006 (2019).

[231] L. Yuan, J. Zhou, M. Zhang, X. Wen, J. M. P. Martirez, H. Robatjazi, L. Zhou, E. A. Carter, P. Nordlander, and N. J. Halas. Plasmonic photocatalysis with chemically and spatially specific antenna–dual reactor complexes. *ACS nano* (2022).

[232] E. Ringe. Shapes, plasmonic properties, and reactivity of magnesium nanoparticles. *The Journal of Physical Chemistry C*, **124**, 15665–15679 (2020).

[233] S. Yu, A. J. Wilson, J. Heo, and P. K. Jain. Plasmonic control of multi-electron transfer and c–c coupling in visible-light-driven co2 reduction on au nanoparticles. *Nano letters*, **18**, 2189–2194 (2018).

[234] S. Li, H. Huang, L. Shao, and J. Wang. How to utilize excited plasmon energy efficiently. *ACS nano*, **15**, 10759–10768 (2021).